HU ISSN 2063-6792

MATERIALS SCIENCE AND ENGINEERING

A Publication of the University of Miskolc

Volume 43, Number 1

Miskolc University Press
2018

CONTENTS

Materials Science and Engineering, Volume 43, No. 1 (2018) pp. 5–10.

BALLOON BASED ATMOSPHERIC STABILITY MEASUREMENT NEAR THE SURFACE

CSONGOR BÁTHORY[1]–ÁRPÁD BENCE PALOTÁS[2]

Detailed vertical temperature and humidity distribution data were collected up to 300 m above sea level using a helium balloon technique. The measurement serves as a basis for research of the link between the mixing layer height and PM_{10} concentration. The balloon with the data recorder, like an aerostat, by its rigging was lifted and then descended. During the test measurements data were recorded and stored. After the experiment analysis demonstrated the instable, mixed and stable air layering as atmospheric stability types.

Keywords: PM_{10}, mixing layer height, atmospheric stability, temperature gradient

INTRODUCTION

In Switzerland meteorological and PM_{10} concentration data were collected for over 15 years to analyze the connection between them [1]. The investigations revealed that on a yearly basis, the wiping effect of the daily precipitation [2] and the turbulent and spreading effect of the gusts typically reduce the concentration of PM_{10} [3]. Case studies however show that this is not always the case: moderate or strong winds can create a resuspension mechanism which increases PM_{10} concentration [4], or can be associated with long-range transport of pollutants [5, 6].

Table 1

Effect of meteorological variables to PM_{10} concentration [1]

Spring		**Summer**		**Autumn**		**Winter**		**Year**	
wind gust	(–)	workday-weekday	(–)	wind gust	(–)	wind gust	(–)	daily precipitation	(–)
MLH	(–)	wind gust	(–)	MLH	(–)	MLH	(–)	wind gust	(–)
yesterday precipitation	(–)	afternoon temperature	(–)	yesterday precipitation	(–)	temperature	(–)	workday-weekday	(–)
relative humidity	(–)		(–)	daily precipitation	(–)	yesterday precipitation	(–)	yesterday precipitation	(–)
net irradiance	(–)					net irradiance	(+)	front effect	(+)
daily precipitation	(–)					daily precipitation	(–)	MLH	(–)
								temperature	(–)

The effects of meteorological conditions vary with the season. On the annual level the mixing layer height (MLH) presented after the effect of the fronts, but in spring, autumn and winter

---

[1] Department of Combustion Technology and Thermal Energy, University of Miskolc
H-3515 Miskolc-Egyetemváros, Hungary
csongor.bathory@uni-miskolc.hu

[2] Department of Combustion Technology and Thermal Energy, University of Miskolc
H-3515 Miskolc-Egyetemváros, Hungary
arpad.palotas@uni-miskolc.hu

as the second significant PM_{10} concentration influencing factor. According to *Table 1.* MLH is a measure for the vertical turbulent exchange within the boundary layer, which is one of the controlling factors for the dilution of pollutants emitted near the ground [7], [8]. It has a decreasing effect (see *Table 1*), meaning that with increasing MLH, PM_{10} concentrations decrease [9], [10].

The easiest approach of determining MLH is the vertical temperature distribution in a way of measurement technique. Various studies looking for a link between the MLH and PM concentrations with different variables (see *Table 2*). Largeron and Staquet reported that the daily-average temperature gradient values are well-correlated with the PM_{10} concentration, in the Alps, with a correlation coefficient of 0.68 [11], as *Table 2* shows. The correlation is stronger if it is restricted to the persistent inversion periods (when the temperature gradient is higher than the winter average over 72 hours), reaching 0.89 [11]. Whiteman and his group analyzed data for the Salt Lake Valley (Utah, USA) for the past 40 years and reported a correlation coefficient of 0.65 between $PM_{2.5}$ and the valley heat deficit (calculated from temperature gradient), for all the 40 winters [12]. Vecchi and his colleagues analyzed air pollution data in Milan, Italy and have determined a correlation coefficient of 0.62 between PM_{10} and the concentration of Radon as a measure of boundary layer stability during nighttime [13]. Guzman-Torres and his colleagues evaluated a correlation coefficient of 0.56 between PM_{10} and surface thermal inversions in Mexico [10].

Table 2

Correlation between characteristic of MLH and PM concentrations [10–13]

Author	Largeron and Staquet	Largeron and Staquet	Whiteman et al.	Vecci et al.	Guzman-Torres et al.
Place	Grenoble, France	Grenoble, France	Salt Lake Valley, USA	Milan, Italy	Mexico, Mexico City
Variable A	PM_{10} conc.	PM_{10} conc.	$PM_{2.5}$ conc.	PM_{10} conc.	PM_{10} conc.
Variable B	daily-average temperature gradient	persistent inversion period	valley heat deficit	concentration of Radon	surface thermal inversion
Correlation coefficient	0.68	0.89	0.65	0.62	0.56

The importance of the atmospheric conditions in the evolution of smog periods is undisputable, especially at valley type terrain. Miskolc is located both in the Szinva Valley and in the Sajó Valley next to the varying heating habits at the suburban areas. The atmospheric stability change can be one of the main reason of the high PM_{10} and $PM_{2.5}$ concentrations during the heating season. The effect of this factor is still not known. To explore the effect, the temperature distribution along the vertical axis at different times of the day were measured. The criteria for the experimental design and implementation were the following:

- must be cost-effective,
- reliable measurements, and automatic data collection,
- the results should be reproducible in identical situation.

1. MATERIALS AND METHODS

1.1. Measuring device

Sensors, power source, microcontroller, and a small display, which are part of the data recording system, have been fixed in a test box (see *Figure 1*).

Table 3
Major components of the measuring device

Device type	**Device Name**	**Key Features**
Microcontroller	Raspberry Pi 3B	Power Consumption: 1.5 W–6.7 W CPU: 1.2 GHz, Memory: 1 GB
Temperature and humidity sensor	DHT22	Humidity: 0–100%, ±2% Temperature: –40–80°C, ±0,5 °C
Temperature, pressure and altitude sensor	HP206C	Temperature: –40–85°C, ±0.5 °C Pressure: 300–1,200 mbar, ±0,01 mbar Altitude: 0–9,999 m, ±0,1 m
Power source	Zendure A3 Power Bank	10,000 mAh

The full weights of the test box, i.e. payload was 873 g. The data recorder program was written in Python 2.7 programming language. The properties of the elements of the measuring device is listed in *Table 3*.

1.2. Lifting method

The test box was lifted by a 2 m diameter latex balloon, filled with helium. A cradle was made for it of 20 m rope. Volume of the balloon was 1.18 m^3, lift capacity was 4 kg.

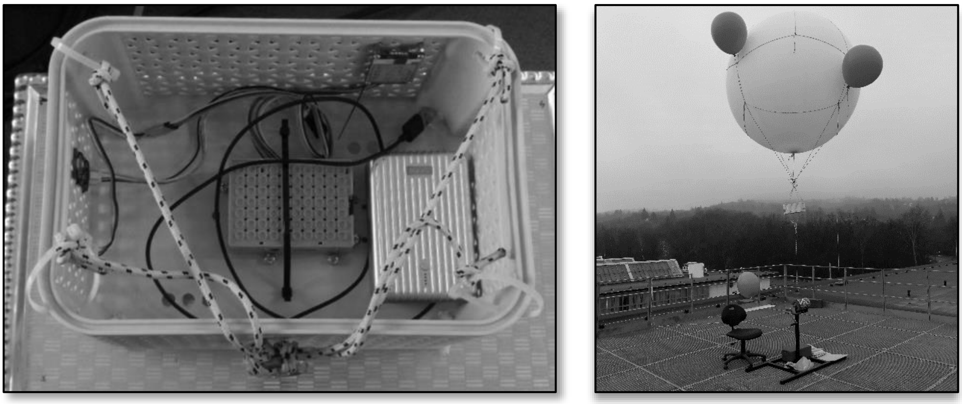

Figure 1
Test box and the compiled measuring system

In addition to the 2 m diameter balloon, four small (approx. 0.5 m diameter) helium balloons were taken as emergency reserve. The balloon loaded with a rope and a carabiner connection had complete lifting capacity of 3.5 kg. The test box (measurement device) was fixed to the base of the cradle, and the balloon + cradle was attached to a winch base (see *Figure 1*). The winch was fed with a 200 m long rope weighing 1.5 kg.

1.3. Measurement location and time

The measurements were implemented from the top roof of the building C/1 at the University of Miskolc, were the height is 125 metres above the sea level (MASL). Three measurements were conducted in January 2018 as shown in *Table 4*.

Table 4

Measurements time and maximum elevated height in MASL

No.	Date	Start	End	Max height
#1	04. 01. 2018.	p.m 03:47	p.m 06:29	185 MASL
#2	05. 01. 2018.	a.m 09:57	a.m 11:28	175 MASL
#3	09. 01. 2018.	a.m 07:52	a.m 09:54	105 MASL

During measurements the test box were elevated over 305 MASL. For the second and third measurements the data are incomplete due to a hardware error. Thus, the ascend part of the measurement #2 is incomplete from 160 to 235 MASL and for measurement #3 the descending period was recorded from 230 MASL height only. Because of the lack of the data and to eliminate the effect of the balloon on air mixing just the decreasing periods of the measurement were analysed in the next chapters.

2. RESULTS AND DISCUSSION

The air temperature data were plotted in 5 m resolution for the way of the measurement's descending balloon periods in *Figure 2*. The 125 MASL altitude represents the rooftop test site, from where the measurement was started, and the balloon has returned. The full, dashed and dotted grey lines show the average temperature gradient of the troposphere ($\Gamma_{avg} = -0.65$ °C/100 m), started from the temperature of the first 5 metres section above the rooftop.

Data for measurement #1 shows a monotone decrease in temperature with increasing altitude, a characteristic of an instable air layering. The total temperature gradient from 125 to 305 MASL is –1.4 °C/100 m. This suggest a presence of a convective boundary layer, which is usual before sunset.

The measurement #2 shows, that the temperature increases by 6 °C until the height of 215 MASL (+6.6 °C/100 m), decrease with 4 °C until 245 MASL (–13 °C/100 m) and after a short (25 m) isothermal section (~0 °C/100 m) the decreasing continues. Based on these, it can be stated that the balloon was passed through an instable and stable air layer during descent. The total temperature gradient from 125 to 300 MASL is –0.9 °C/100 m. This suggest a mixed boundary layer: a stable boundary layer started to spread to instable boundary layer thanks to the warming effect of the sun.

During measurement #3 the sensors didn't detect temperature change until 150 MASL and an isothermal section was recorded. Above 150 MASL the temperature increases with altitude, indicating a stable air layering. The temperature gradient from the starting point (at 125 MASL, with 1.6 °C) to 225 MASL (3.5 °C) is +1.8 °C/100 m. This suggest a stable boundary layer or even an inversion, which is usually seen before sunrise.

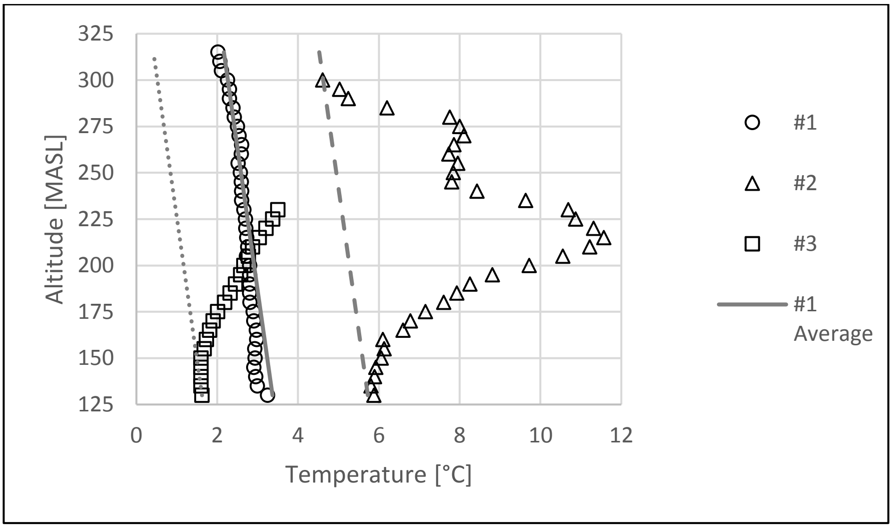

Figure 2

Air temperature data in 5 m resolution for the way of the descending balloons

CONCLUSION

Detailed vertical temperature and humidity distribution data were collected up to 305 MASL above the sea level using a helium balloon technique. The balloon with the data recorder, like an aerostat, was lifted and then pulled back down.

Table 5

Recorded temperature gradient results

#1 – afternoon			**#2 – before noon**			**#3 – morning**		
Height		Gradient	Height		Gradient	Height		Gradient
MASL		°C/100 m	MASL		°C/100 m	MASL		°C/100 m
125		–1.4	125	215	+6.6	125	150	0
			215	245	–13	150		+1.8
			245	270	0			
	305		270	300	–12.3		230	
Stability:		Instable	Stability:		Mixed	Stability:		Stable

During the test measurements data were recorded referring to instable (04. 01. 2018. – afternoon), mixed (05. 01. 2018. – before noon) and stable (09. 01. 2018. – morning) air layering as shown in *Table 5*. The tests were suitable for detecting faults in the data collection system. The data recorder device must be protected against the external conditions, like humidity, rain and UV, thermal radiation.

Our plans for future are reliability test of sensors, to extend sensors with low-budget, light weight PM_{10} counter and to uniform the evaluation of data while carrying out further measurements to have more information about the connection between the atmospheric stability and PM_{10} concentrations. Once we understand this factor, we will have a chance to reduce the pollution during the effected periods.

REFERENCES

[1] I. Barmpadimos, C. Hueglin, J. Keller, S. Henne, and A. S. H. Prévôt (2011). Influence of meteorology on PM_{10} trends and variability in Switzerland from 1991 to 2008. *Atmos. Chem. Phys.,* Vol. 11, No. 4, pp. 1813–1835.

[2] A. Flossmann, W. Hall, and H. Pruppacher (1985). A theoretical study of the wet removal of atmospheric pollutants. Part I: The redistribution of aerosol particles captured through nucleation and impaction scavenging by growing cloud drops. *Journal of the atmospheric sciences,* Vol. 42, No. 6, pp. 583–606.

[3] S. Vardoulakis and P. Kassomenos (2008). Sources and factors affecting PM10 levels in two European cities: Implications for local air quality management. *Atmospheric Environment,* Vol. 42, No. 17, pp. 3949–3963.

[4] A. Triantafyllou (2001). PM10 pollution episodes as a function of synoptic climatology in a mountainous industrial area. *Environmental Pollution,* Vol. 112, No. 3, pp. 491–500.

[5] D. Asimakopoulos, H. Flocas, T. Maggos, and C. Vasilakos (2011). The role of meteorology on different sized aerosol fractions (PM10, PM2. 5, PM2. 5–10). *Science of the Total Environment,* Vol. 419, pp. 124–135.

[6] L. Makra, I. Matyasovszky, Z. Guba, K. Karatzas, and P. Anttila (2011). Monitoring the long-range transport effects on urban PM10 levels using 3D clusters of backward trajectories. *Atmospheric environment,* Vol. 45, No. 16, pp. 2630–2641.

[7] G. Tang et al. (2016). Mixing layer height and its implications for air pollution over Beijing, China. *Atmospheric Chemistry and Physics,* Vol. 16, No. 4, pp. 2459–2475.

[8] A. Geiß et al. (2017). Mixing layer height as an indicator for urban air quality? *Atmospheric Measurement Techniques,* Vol. 10, No. 8, p. 2969.

[9] J. Holst, H. Mayer, and T. Holst (2008). Effect of meteorological exchange conditions on PM10 concentration. *Meteorologische Zeitschrift,* Vol. 17, No. 3, pp. 273–282.

[10] D. Guzmán-Torres et al. (2009). Effects of meteorology on diurnal and nocturnal levels of priority polycyclic aromatic hydrocarbons and elemental and organic carbon in PM10 at a source and a receptor area in Mexico City. *Atmospheric Environment,* Vol. 43, No. 17, pp. 2693–2699.

[11] Y. Largeron and C. Staquet (2016). Persistent inversion dynamics and wintertime PM10 air pollution in Alpine valleys. *Atmospheric Environment,* Vol. 135, pp. 92–108.

[12] C. D. Whiteman, S. W. Hoch, J. D. Horel, and A. Charland (2014). Relationship between particulate air pollution and meteorological variables in Utah' Salt Lake Valley. *Atmospheric Environment,* Vol. 94, pp. 742–753.

[13] R. Vecchi, G. Marcazzan, and G. Valli (2007). A study on nighttime–daytime PM10 concentration and elemental composition in relation to atmospheric dispersion in the urban area of Milan (Italy). *Atmospheric Environment,* Vol. 41, No. 10, pp. 2136–2144.

Materials Science and Engineering, Volume 43, No. 1 (2018) pp. 11–16.

AN APPROACH FOR ELIMINATING PHENYL ISOCYANATE FROM SOLVENT USED IN ISOCYANATE PRODUCTION

R. ZSANETT BOROS[1, 2]–ISTVÁN VARGA[1]–BARNABÁS BUZELLÁK[1]–
MÁRTA HARANGOZÓ[1]–MILÁN SZŐRI[2]–BÉLA VISKOLCZ[2]–
LÁSZLÓ FARKAS[1]

Methylene diphenyl diisocyanate (MDI) is one of the most important raw materials of polyurethane industry. During its synthesis unwanted by-products might be formed such as phenyl isocyanate (PI). In this laboratory work, a separation method has been developed and tested for the the elimination of phenyl isocyanate from the ortho-dichlorobenzene solvent purified after MDI production. This method is based on conversion of phenyl isocyanate by MDI precursor methylene diphenyl diamine (MDA). The formed carbamide compounds were separated from the solvent by either distillation or filtration. As a result, the initial phenyl isocyanate content of 9,000 ppm was successfully reduced to 30 ppm by distillation and less efficiently to 231 ppm by filtration.

Keywords: methylene diphenyl diisocyanate, ortho-dichlorobenzene, phenyl isocyanate, distillation, filtration

INTRODUCTION

Polyurethanes are the most versatile class of polymers, used in a surprising array of commercial applications such as flexible- and rigid foams, solid elastomers, thermoplastic polyurethanes, coatings, adhesives, sealants and elastomers used on floors and automotive interiors [1]. They are formed by the exothermic reaction between alcohols with two or more reactive hydroxyl and isocyanates that have more than one reactive isocyanate group. Methylene diphenyl diisocyanate (MDI) is one of the most significant raw material of polyurethane industry [2]. Production of MDI occurs via phosgenation of the appropriate diamine, namely methylene diphenyl diamine (MDA), in a solvent such as dichlorobenzene which is removed from the product by distillation and is reused [3]. MDA is synthetized from the reaction between aniline and formalin. In the case of MDA synthesis some aniline could be remained in the system which might be converted to phenyl isocyanate via phosgenation *(Figure 1)*. In MDI synthesis phenyl isocyanate might be a possible source of several by-product due to its reactivity [4]. The reactivity of aniline derivatives with phosgene have been studied by Ulrich et al. [5]. The aromatic diamines such as the MDA are much more reactive amines than others. The reactivity of different aromatic amines with diisocyanates have been measured [6]. Beside the phenyl isocyanate formation, numerous other side-reactions can occur via the MDI synthesis producing several unwanted by-products which might cause problems. For instance, the isocyanates can easily react with amines forming carbamides due to the high reactivity of isocyanate group. Callison et al. investigated the reactions between carbamides and phosgene producing precursor to chlorine radicals, which could form

---

[1] Wanhua-BorsodChem Ltd., Bolyai tér 1.
H-3700 Kazincbarcika, Hungary
renata.boros@borsodchem.eu

[2] Institute of Chemistry, Faculty of Materials Science and Engineering, University of Miskolc
H-3515 Miskolc-Egyetemváros, Hungary

conjugated systems with the MDI backbone promoting discoloration [7]. The formation of the by-products is substantial. The elimination of them encounters difficulties.

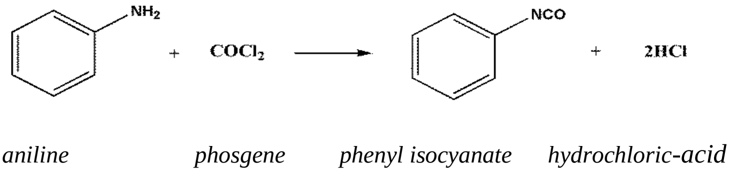

Figure 1
Phenyl-isocyanate formation via phosgenation of aniline

This study focusses only on one possible by-product, phenyl isocyanate. The aim of this research was to find out an appropriate method for phenyl isocyanate removal. Our exploration was based on the reaction of phenyl isocyanates with amines [8]. The phenyl isocyanate was converted to carbamide *(Figure 2)* and then eliminated from the solvent.

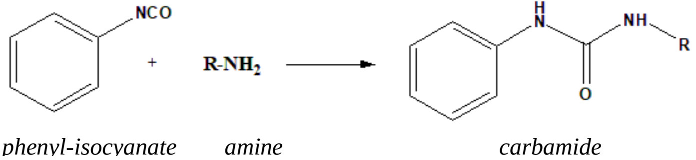

Figure 2
Reaction of phenyl-isocyanate with amine

1. APPLIED METHODS AND REAGENTS

Distillations were carried out using distillation apparatus set up in the laboratory. Three-necked, round-bottom 250 ml of glass flask was used as reaction vessel while a 100 ml of one-necked round-bottom glass flask was used as volumetric flask for the distillate. The flasks were connected by a distillation head and a Liebig-cooler. Heating was provided by melted metal bath heated by laboratory heater. The head- and bottom temperatures were controlled using thermometers. In the case of vacuum distillation, the reduced pressure was set up by oil-ring pump produced by Leybold. About 100 ml of ODCB sample – arisen from the plant – was used mixed with phenyl isocyanate purchased by Sigma Aldrich. For the filtration Whatman glass vacuum membrane filtration device was applied. The vacuum was adjusted using water suction pump. The grain size of the filter was 1.4 µm.

The phenyl isocyanate content of the samples was analyzed by Agilent 6890N gas chromatograph applying Zebron Inferno capillary column, using flame ionization detector (FID). Scanning electron microscopy (Joel T220 SEM) was used for mapping the structure of the formed carbamides.

2. RESULTS AND DISCUSSION

Distillation was the first type of phenyl isocyanate removal method which was tried. The first idea was that the ortho-dichlorobenzene will be purified this by-product via simple distillation. The phenyl isocyanate content was measured before and after the distillation. The results are summarized in *Table 1*.

Table 1

Phenyl isocyanate content before and after distillation

PI content (ppm)	
Before distillation	After distillation
1,800	2,979
1,800	2,870
1,800	2,596

The initial 1,800 ppm was not decreased but increased after the distillation without using any reagent. Due to the similar boiling points of the ortho-dichlorobenzene (180 °C) and phenyl-isocyanate (166 °C) the separation of the compounds is difficult. The accumulation of the isocyanate in the distillate can be explained by the lower boiling point, although the difference in boiling points are not large enough to ensure complete separation.

MDA was tested as a reagent for converting phenyl isocyanate into a non-volatile compound before the distillation. Samples with different phenyl isocyanate content was reacted with MDA and then distilled. The starting phenyl isocyanate content was greatly reduced (<100 ppm). The results are summarized in *Table 2*. The amino group of the MDA was reacted with the isocyanate group of the phenyl isocyanate producing carbamide bond. The product carbamide was remained in the bottom of the flask while the ortho-dichlorobenzene was distilled. The phenyl isocyanate content was reduced efficiently.

Table 2

Phenyl isocyanate content before and after distillation using MDA as reactant

PI content (ppm)	
Before distillation	After distillation (using MDA as reagent before)
1,800	89
700	20
500	10

The other main advantage of using MDA as reactant is that it is a familiar material in MDI synthesis. Any MDA residues in the solvent will never cause problems because it can be easily eliminated from the system. In addition, MDA is one of the raw materials produced so that using it will be obvious.

Vacuum distillation – performed under reduced pressure – was also tested for solvent purification after MDA was added to the solvent to react with the phenyl isocyanate. The efficiency of the simple and vacuum distillation is compared in *Table 3*. The initial phenyl isocyanate content was 9,000 ppm. The final phenyl isocyanate content was <40 ppm. The vacuum distillation seemed to be more effective than the simple distillation, although the difference in removal efficiency is minimal. This phenomenon could be explained by the fact that at higher temperature carbamides can be decomposed into amine and isocyanate. In the case of the simple distillation higher temperature was used which was favorable for the decomposition of the product facilitating phenyl isocyanate formation, while in the case of vacuum distillation lower temperature resulted in less isocyanate release.

Table 3

Phenyl isocyanate content before and after simple- and vacuum distillation

Type of distillation	**PI content (ppm)**	
	Before distillation	**After distillation**
simple	9,000	29
		30
		29
vacuum		18
		17
		19

Filtration of impurities is a frequently used method in the industry for purification. The applicability of it was tested for phenyl isocyanate elimination, too. Ortho-dichlorobenzene samples with high phenyl isocyanate content were mixed with the appropriate amount of MDA at room temperature and at higher temperatures as well. Beside the influence of the temperature the effect of the stirring was also studied.
The results are summarized in *Table 4*.

Table 4

Phenyl isocyanate content before and after filtration using MDA as reagent

Sample	**Temperature [°C]**	**Stirring**	**PI content (ppm)**	
			Before filtration	**After filtration**
1	25–30	No	9,000	58
2	25–30	Yes		57
3	70–90	Yes		110
4	110–120	Yes		128
5	120–130	Yes		231

The starting 9,000 ppm was significantly decreased <300 ppm. It was surprising that without stirring (for 1 hour) and at room temperature the phenyl isocyanate was reduced from 9,000 ppm to 58 ppm. As the temperature was higher the phenyl isocyanate reduction efficiency of the MDA was lower. The structures of the filtrated solid sediments were different. They were examined by scanning electron microscopy. According to the microscopic views *(Figure 3)* the particle sizes of the formed carbamides are different.

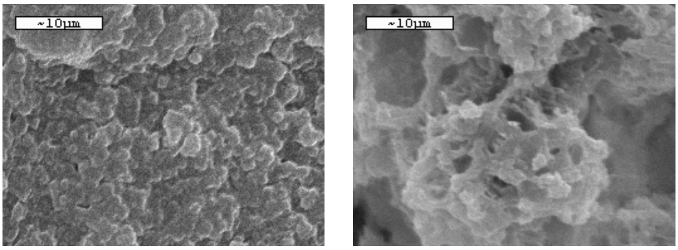

25–30 °C 70–90 °C

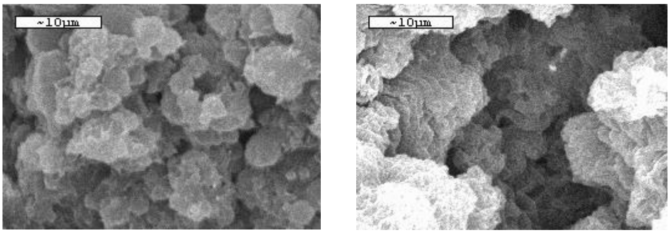

110–120 °C 120–130 °C

Figure 3
Microscopic views of the filtrated carbamide compounds

At lower temperature the reaction between the MDA and phenyl isocyanate resulted smaller particle sized (<10µm) carbamide sediment, while at higher temperature bigger sized (>10µm) particles were formed. At higher temperature the decomposition of the carbamide into phenyl isocyanate and amine could also occur such as in the case of the simple distillation. Therefore, more phenyl isocyanate was found in the solvent after the filtration at higher temperature. Considering the filtration method, the phenyl isocyanate content can be reduced significantly. The efficiency of the filtration is as adequate as the distillation's. This procedure can be feasible even in the technology. The filtrate was also examined and it was found that it has a little MDA content. If this method will be applied for phenyl isocyanate removing, it is necessary to take care about this MDA content of the ortho-dichlorobenzene as well.

CONCLUSION

This study was focused on removing of a possible by-product – *phenyl isocyanate* – of MDI synthesis from the solvent. Useful methods were found for phenyl isocyanate elimination: distillation or filtration.

Simple distillation of the ortho-dichlorobenzene was not effective because the phenyl isocyanate co-distilled with ortho-dichlorobenzene. It was essential to convert this isocyanate into another compound which is easier to separate from the solvent. The idea was to find a reactant which can easily react with the phenyl isocyanate. Using MDA as a reagent appeared to be obvious as it is the precursor of MDI synthesis. Applying it as a reagent will never cause any problems even if it remains in the system. The results confirmed that phenyl isocyanate can be reduced significantly from the ortho-dichlorobenzene using MDA.

Filtration seemed to be also a quite good method for a possible phenyl isocyanate reduction. MDA was used as a reagent in this way, too. The efficiency of this method is lower than the distillation, however it is effective enough.

Considering the experimental results, it could be said that both distillation and filtration could be suggested for a possible technological application after MDA was used as a reagent for converting phenyl isocyanate to carbamide. Some disadvantages need to be noted as well such as during the filtration the filter packages must be cleaned frequently causing some difficulties and in the case of distillation high energy is requires for evaporation of the solvent.

ACKNOWLEDGMENTS

This research was supported by the European Regional Development Fund in the framework of the GINOP-2.3.4-15-2016-00004 project. The authors would like to thank Tamás Purzsa, Vice President of BorsodChem, for his helpful contribution.

REFERENCES

[1] M. Sycher (2013). *Szycher's Handbook of Polyurethanes*. CRC Press.

[2] M. Ionescu (2007). *Chemistry and technology of polyols for polyurethanes*. Vol. 56.

[3] D. C. Allport, D. S. Gilbert, and S. M. Outterside (2003). *MDI and TDI: Safety, Health and the Environment: A Source Book and Practical Guide*.

[4] P. Tremblay, J. Lesage, C. Ostiguy, and H. Van Tra (2003). Investigation of the competitive rate of derivatization of several secondary amines with phenylisocyanate (PHI), hexamethylene-1,6-diisocyanate (HDI), 4,4'-methylenebis(phenyl isocyanate) (MDI) and toluene diisocyanate (TDI) in liquid medium. *Analyst*, Vol. 128, No. C, pp. 142–149.

[5] H. Ulrich (1974). Reaction of Phosgene with N-Methyleneaniline Derivatives. *J. Org. Chem*, Vol. 39, No. 7, pp. 11–13.

[6] G. R. Somayajulu, I. A. Gribova, and I. A. Gribova (1963). The Reaction of Aromatic Diamines with Di-isocyanates-II The Reactivity of Some Aromatic Diamines. *Polymer Science U.S.S.R*, Vol. 847, No. 2, pp. 227–232.

[7] J. Callison (2011). The investigation of a side reaction leading to colour formation in a polyurethane production chain (Ph.D Dissertation). University of Glasgow.

[8] F. L. Hegarty, Anthony F., Hegarty, Con N., Scott (1970). The Reactivity of Phenyl Isocyanate in Aqueous Solution. *J.C.S. Pekin II*, Vol. 1, No. 1366, pp. 0–4.

Materials Science and Engineering, Volume 43, No. 1 (2018) pp. 17–25.

THE EXAMINATION OF THE GRAIN REFINING EFFECTS OF TITANIUM IN HYPOEUTECTIC AL-SI FOUNDRY ALLOYS

MARIANNA BUBENKÓ[1]–MONIKA TOKÁR[2]–GYÖRGY FEGYVERNEKI[3]

Grain refining is an important technological step for the nucleus growth of the melt, in order to increase the number of nuclei, to improve mechanical properties (tensile strength, yield strength, hardness, elongation), feeding conditions and to decrease the tendency of hot tearing and the degree of sintering. [1], [2] The aim of the experiments was the determination of the grain refining effects of titanium (Ti) addition in the form of AlTi5B1 master alloy to the examined alloys (AlSi7MgCu0.5 – AC 42 000, AlSi9Cu3Fe0.5 – 46 500; AlSi9Cu1 – AC 46 400).

Keywords: Al-Si alloys, grain refinement, titanium, thermal analysis, nucleus formation

INTRODUCTION

Providing the uniaxial dendritic structure for cast alloys in fine – grained cast state is necessary. Thus, the regulation of the nucleus formation of the melt via grain refinement is an essential step to achieve the required quality and mechanical properties [1], [2], [3]. Grain refining is one of the strengthening mechanisms which provide higher mechanical properties to an alloy. Grain refinement would increase the number of grains and their boundaries, therefore, increase the yield strength of the material. [4] The addition of grain refiner increases the number of nucleation sites, thus, promoting equiaxed grain growth rather than columnar. Large grains of α-Al in the microstructure are responsible for a number of defects, like scattered porosity, microcracks, deterioration of mechanical properties, etc. For many years, grain refinement of α-Al has been obtained by the controlled addition of intermetallic compounds of the type: Al_3Ti, TiB_2, TiC, to the liquid metal. For this purpose, master alloys, like AlTi5B1, AlTi3B1 or AlTi3C015 can be used, or the newly developed alloys of AlTi1.7B1.4, AlTi1.2 B0.5 or AlSr5Ti0.8B0.7. [5] There are several theories describing the process of grain refinement which are available in numerous publications. The most frequently adopted one claim that in the case of Al–Ti–B refiner, the main compound responsible for the grain refining effect is TiB_2. [5] According to the duplex nucleation theory (Mohanty and Gruzleski [6]), in case of the use of Al–Ti–B master alloys, a Ti rich melt layer is formed surrounding the TiB_2 particles in the melt. If the local Ti content is higher than 0.15 wt%, a solid $TiAl_3$ layer is formed on the surface of TiB_2 particles *(Figure 1)*. Then, the aluminium particles are formed through peritectic reactions on the $TiAl_3$ layer.

---

[1] Institute of Foundry Engineering, University of Miskolc
H-3515 Miskolc-Egyetemváros, Hungary
b.marianna1228@gmail.com

[2] Institute of Foundry Engineering, University of Miskolc
H-3515 Miskolc-Egyetemváros, Hungary
monika.tokar@uni-miskolc.hu

[3] Institute of Foundry Engineering, University of Miskolc
H-3515 Miskolc-Egyetemváros, Hungary
gyorgy.fegyverneki@nemak.com

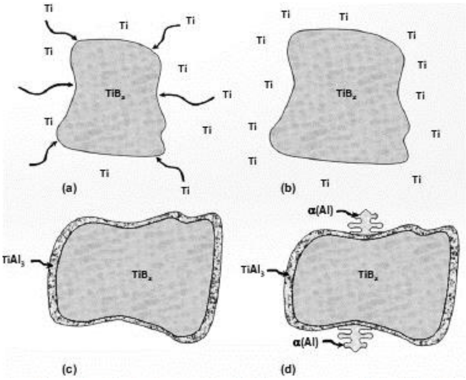

Figure 1
Duplex nucleation theory. (a) Excess Ti (Ti > 2.21) in solution, (b) Ti segregated to the TiB_2 *– melt interface, (c) formation of* $TiA1_3$ *layer on TiB2, (d) Nucleation of α-Al by peritectic reaction* [7]

1. EXPERIMENTAL CONDITIONS AND RESULTS

The three examined foundry alloy melts (***AlSi7MgCu0.5 – 1st alloy***; ***AlSi9Cu1 – 2nd alloy***; ***AlSi9Cu3Fe0.5 – 3rd alloy***) were alloyed with AlTi5B1 master alloy during the rotary degassing process [with nitrogen (N_2) inert gas]. The initial Ti contents were between 900–1,200 ppm. Based on the recommendation of the alloy manufacturer (Trimet GmbH), 750 g AlTi5B1 master alloy was added to 1,000 kg melt (37.5 ppm Ti content in function of total amount). The effect of additional Ti content (in the form of AlTi5B1 master alloy) on the nucleus formation properties of the aluminium melt was examined.

Optical Emission Analyzer technique was used to determine the chemical compositions of the alloys and the amount of the beneficial AlTi5B1 master alloy. Thermal analysis was carried out to examine the degree of grain refinement. The equipment used for the thermal analysis and the dimensions of the casted test bar can be seen in *Figure 2*. The test bar was casted in a steel crucible preheated to 200 °C.

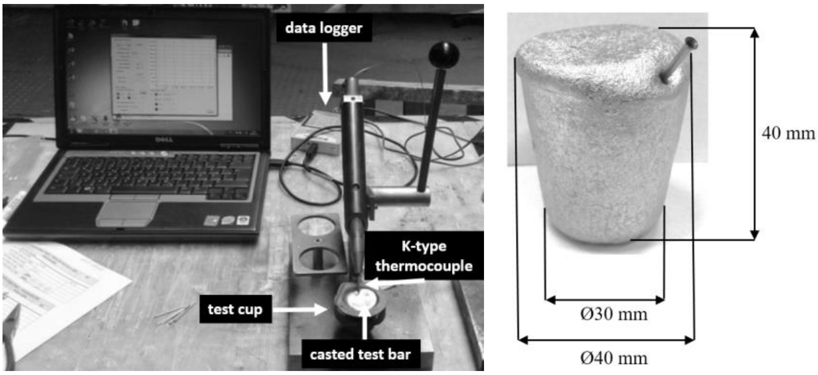

Figure 2
Thermal analysis equipment and casted test bar

For the examination of the mechanical properties, so-called Diez-test bars were casted after melt treatment in a Diez-die, which die was prepared according to a German standard. [8] Tensile test specimens were made from the Diez-test bars according to industrial standard. The test bars were cylindrical, 5 mm in diameter and 50 mm long.

Diez-test bars are technological test bars which were used to examine the grain refining effect of AlTi5B1 master alloy on the alloys. In this case, certain external influences that emerge during casting and the affect the mechanical properties can be eliminated.

To examine the mechanical properties, the test bars were heat treated (1st alloy-T5, 2nd alloy-T6, 3rd alloy-was not heat treated) under operating conditions. The Diez-die and test bar with their locations where the tensile specimens were taken can be seen in *Figure 3*.

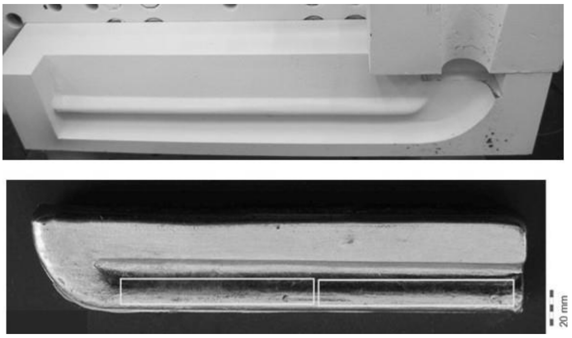

Figure 3

The Diez-die and test bar with the locations of the tensile specimens

1.1. Composition

The titanium concentration before and after the addition of AlTi5B1 master alloy, determined by compositional analysis, can be seen in *Table 1*.

Table 1

The titanium concentrations based on the compositional analysis

Alloys	**Techno-logical step**	**Titanium concentra-tion (wt%)**	**Titanium concentra-tion (ppm)**	**Difference of Titanium concentration (ppm)**	**Casting temperature (°C)**
(1st) AlSi7MgCu0.5	Before Ti addition (series)	0.11935	1,193.5	35.9	728
	After Ti addition	0.12294	1,229.4		
(2nd) AlSi9Cu1	Before Ti addition (series)	0.10766	1,076.6	11.9	737
	After Ti addition	0.10885	1,088.5		
(3rd) AlSi9Cu3Fe0.5	Before Ti addition (series)	0.08911	891.1	37.5	716
	After Ti addition	0.09286	928.6		

In case of the 2nd alloy, only 31.73% of the 37.5 ppm additional titanium was dissolved in 1,000 kg melt. The cause of this might be the presence of other alloying elements which formed intermetallic phases with titanium. Thus, the titanium content of the additional AlTi5B1 master alloy could not have any beneficial effects on grain refinement [9].

1.2. Thermal analysis

By thermal analysis, the efficiency of grain refinement can be determined by the evaluation of the cooling curves of the solidifying melt. The thermal analyser is equipped with a thermocouple which is connected to a signal processing data logger. The data logger produces the temperature – time cooling curves from which the various processes in the solidifying metal can be determined.

The cooling curves of test bars in case of ***1st alloy (AlSi7MgCu0.5)*** are shown in *Figure 4*. As it can be seen on the curve with dotted line, the starting temperature of the nucleus formation is 3.03 °C higher after AlTi5B1 addition.

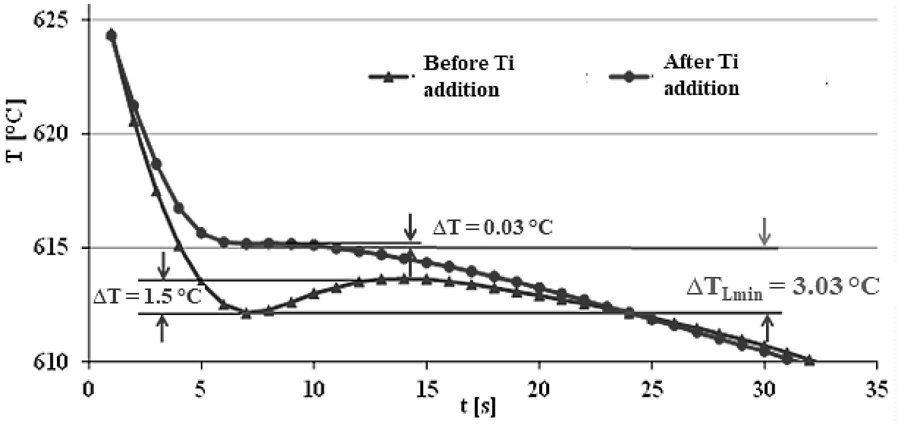

Figure 4

The liquidus temperature ranges of the cooling curves of the 1st (AlSiMgCu0.5) alloy

The differences of the starting temperature of nucleation before and after AlTi5B1 addition are shown in *Table 2*.

Table 2

The differences of the starting temperature of nucleation before and after AlTi5B1 addition

Alloys	**Titanium concentration after AlTi5B1 addition (ppm)**	**ΔT_{Lmin} (°C)**
(1st) AlSi7MgCu0.5	1,229.4	3.03
(2nd) AlSi9Cu1	1,088.5	4.87
(3rd) AlSi9Cu3Fe0.5	928.6	0.17

The addition of extra 750 g AlTi5B1 master alloy had a positive effect (mainly in case of 1st and 2nd alloys) on the nucleus formation and increased the ΔT_{Lmin}, cause the starting temperatures of the nucleation were increased.

1.3. Grain numbers – thermal analysis test bars

The thermal analysis test bars were cut horizontally, polished and Barker etched before further microstructure analysis. On the etched test specimen 15 microstructural images (226.8 mm^2 examined area/specimen) were taken from each one test bar, using an optical microscope with 25× magnification. The number of grains was determined on each image. The number of (α)Al grains on the surfaces of the test bars can be counted due to the various colours caused by polarised light. The Barker colour etched micrographs in case of 3rd alloy can be seen in *Figure 5*.

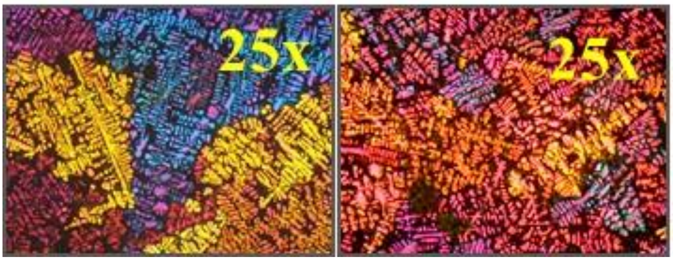

Figure 5
The Barker colour etched micrographs: (a) 3rd alloy before grain refinement, (b) after the addition of AlTi5B1 grain refining master alloy

The average grain number in case of the thermal analysis test bars are illustrated in *Figure 6*. The examination of the thermal analysis test bars revealed that the increased titanium concentration led to increased grain number. The grain number of the test bars with higher ΔT_{Lmin} (3.03 °C and 4.87 °C) temperature after AlTi5B1 addition was 2.8–2.9× higher. Based on the cooling curves and the microscopic particle analysis it can be stated that grain refinement occured in all three alloys. The objective of further research is to determine if the solved titan concentration of the second alloy was enough to achieve such effect.

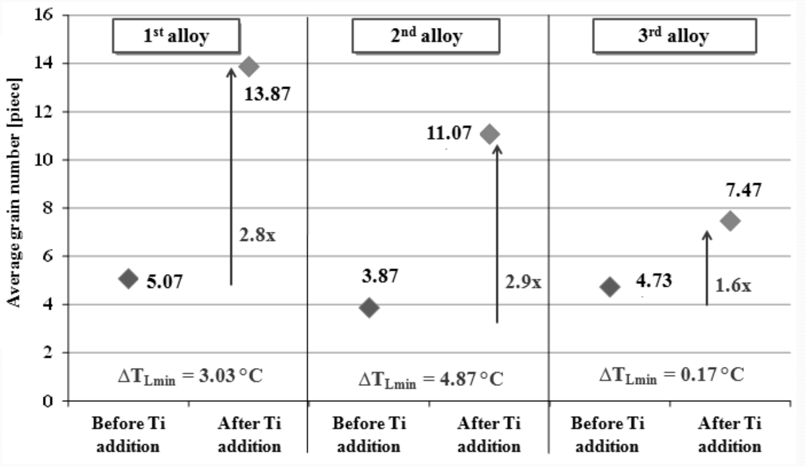

Figure 6
Average grain number in case of the thermal analysis test bars

1.4. The examination of Diez-test bars

Mechanical test and microstructure analysis were carried out on test specimens prepared from standard Diez-test bars. We determined the effect of extra 750 g AlTi5B1 master alloy addition on the mechanical properties and on the efficiency of the grain refinement.

Figure 7 shows the average grain numbers of the tensile test specimens made out of Diez-test bars. The AlTi5B1 addition resulted higher grain number.

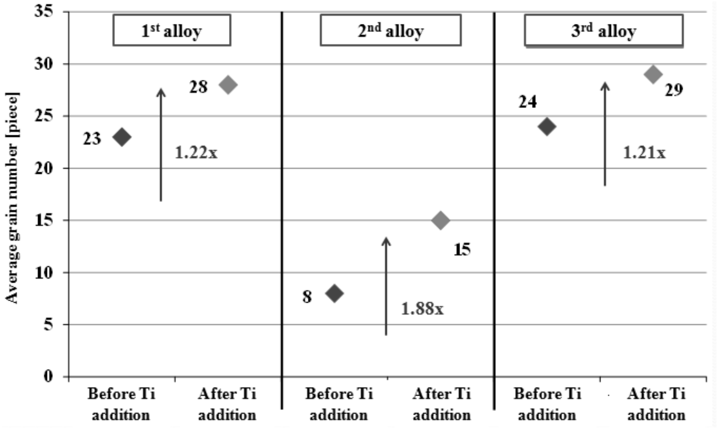

Figure 7

The average grain numbers of the tensile test specimens made out of Diez-test bars

During mechanical tests, the tensile strength, the yield strength and the elongation were determined. Three Diez-test bars were casted from each alloy, and two tensile test specimens were prepared from each Diez-test bars. The average values of six tensile specimens for each alloy can be observed in *Figures 8–10*. The results were compared to the required operational strength values.

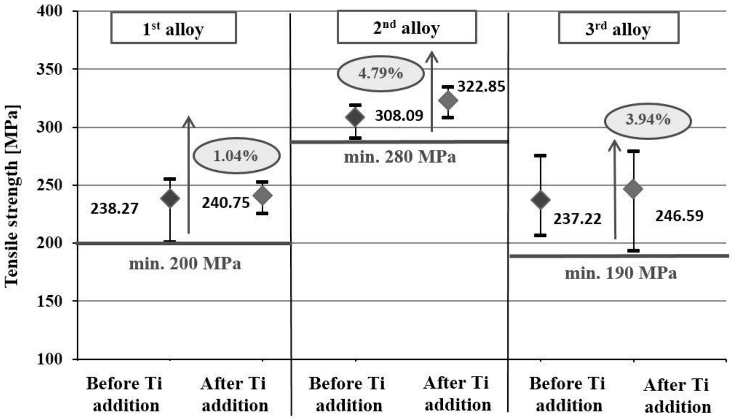

Figure 8

The average tensile strength of the specimens from the Diez-test bars

It can be observed that after the addition of the extra master alloy, the tensile strength *(Figure 8)* and yield point values *(Figure 9)* increased by a few percentage. In case of the 2nd alloy, the grain number of which was almost two times higher (1.88×), the average tensile strength increased with almost 4.79%. The average elongation after the AlTi5B1 master alloy addition increased with 7% in case of the 2nd alloy. In case of 1st and 3rd alloys the elongation values were decreased.

The average standard deviation of the elongation values was rather high. In order to determine the reason for the low strength values, the fracture surfaces of the tensile specimens were examined.

In case of all three alloys, the fracture surfaces of the specimens prepared from the Diez-test bars with mechanical properties below the limit values were examined with a stereo microscope. The following observations can be made based on the micrographs.

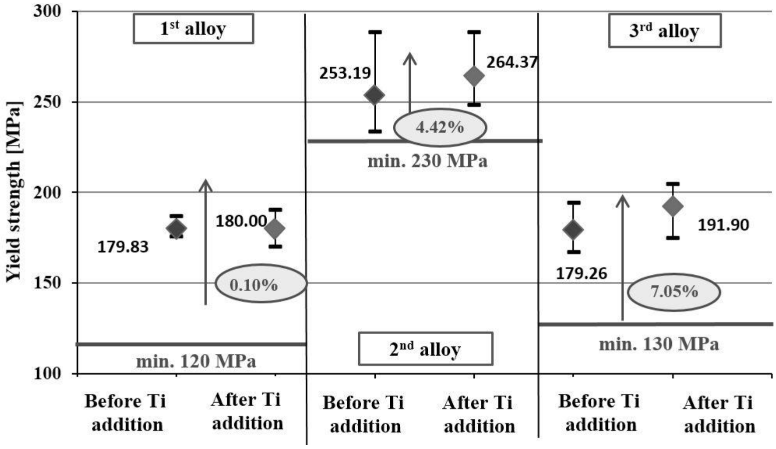

Figure 9

The average yield strength of the specimens from the Diez-test bars

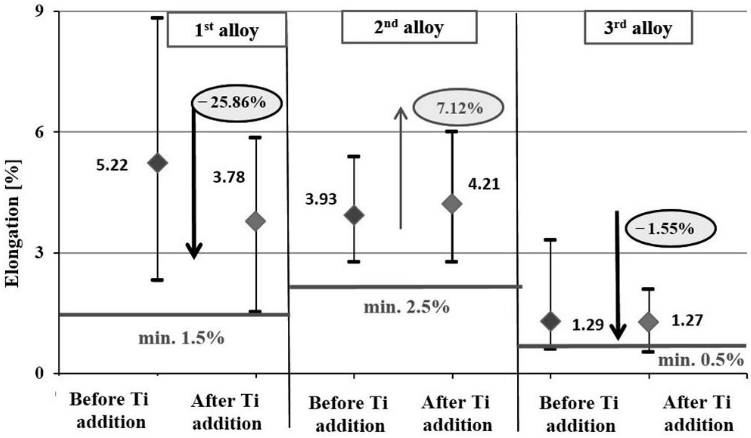

Figure 10

The average elongation of the specimens from the Diez-test bars

The stereo microscopic image of the test bar with the Al_2O_3 oxide inclusion can be seen in *Figure 11*.

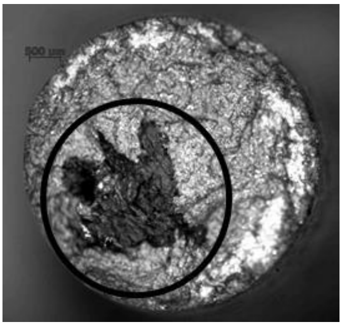

Figure 11
The surface of test bar prepared from the Diez-test bar of the melt of the 1st alloy before Ti addition, with large Al_2O_3 oxide inclusion

CONCLUSIONS

Based on the evaluation of the experimental test bars and the prepared diagrams, it can be concluded that the extra 750 g AlTi5B1 master alloy addition to the three Al-Si alloy melts (AlSi7MgCu0.5; AlSi9Cu; AlSi9CuFe0.5) had a positive effect on the nucleus formation and increased the starting temperature of the crystallization.

The additional titanium concentration resulted in increased average grain number. The grain number was 2.8–2.9 times higher of the thermal test bars after AlTi5B1 addition, in case of the alloys with higher ΔT_{Lmin} (3.03 °C and 4.87 °C) temperatures.

The effect of the additional 750 g AlTi5B1 master alloy on the mechanical properties could be observed on the Diez-test bars. A correlation can be observed between the average tensile strength, yield strength and grain number of the series and the test bars with higher titanium concentration: the increased grain number resulted in higher tensile strength and yield strength value. However, the elongation values were greatly affected by the inclusion content of the melt. The parameters influencing melt quality (e. g. the efficiency of the melt cleaning) should be reviewed, as the decreased mechanical properties cannot be attributed to the addition of AlTi5B1 master alloy, but the inclusion content of the melt.

ACKNOWLEDGEMENT

The authors are grateful to Árpád Kovács for carrying out the tests with scanning electron microscope. The authors are grateful to Mária Ambrus for her advice.

The described article/presentation/study was carried out as part of the EFOP-3.6.1-16-2016-00011 Younger and Renewing University – Innovative Knowledge City – institutional development of the University of Miskolc aiming at intelligent specialisation project implemented in the framework of the Szechenyi 2020 program. The realization of this project is supported by the European Union, co-financed by the European Social Fund.

REFERENCES

[1] Y. Birol (2012). Performance of AlTi5B1, AlTi3B3 and AlB3 master alloys in refining grain structure of aluminium foundry alloys. *Materials Science and Technology*, 28:4, pp. 481–486.

[2] K. T. Kashyap, T. Chandrashekar (2001). Effects and mechanism of grain refinement in Al alloy. *Indian Academy of Science*, Vol. 24, No. 4, pp. 345–353, Aug.

[3] P. S. Mohanty, J. E. Gruzleski (1995). Mechanism of grain refinement in Al, Department of Mining & Metal Engineering. *Acta Metallurgical Material*, Vol. 43, No. 5, pp. 2001–2012.

[4] M. Deni Ferdian (2014). *Effect de la vitesse de refroidissement sur la tailla des grains, la modification eutectique et la precipitation d´intermetalliques riches en fer dans des alliages Al-Si hypoeutectiques*. pp. 10, PhD-Thesis.

[5] Z. Zamkotowicz, T. Stuczynski, B. Augustyn, M. Lech-Grega, W. Wezyk (2004). Investigation of grain refinement fading in hypoeutectic aluminium-silicon alloys. *Light Metals*, pp. 807–816.

[6] P. S. Mohanty, J. E. Gruzleski (1995). Mechanism of Grain Refinement in Aluminium. *Acta Materialia*, Vol. 43, No. 5, pp. 2001–2012.

[7] F. C. Robles, Hernandez, J. M. H. Ramírez, R. Mackay (2017). *Al-Si Alloys – Automotive, Aeronautical, and Aerospace Application*. Springer International Publishing AG, p. 214.

[8] H. W. Rockenschaub, R. Gschwandter (2008). *Eigenschaftsprofil und Wärmebehandlung der kokillengusslegierung AlSi12 cunimg (EN1706 AC–48000)*. Österreichisches Gießerei Institut, Leoben.

[9] J. Campbell (2015). *Complete Casting Handbook*. 2nd Edition, Metal Casting Processes, Metallurgy, Techniques and Design. Boston: Butterworth–Heinemann.

Materials Science and Engineering, Volume 43, No. 1 (2018) pp. 26–30.

THE EXAMINATION OF THE MECHANICAL PROPERTIES OF WATER GLASS CORE SANDS

VIKTÓRIA DARGAI[1]–LÁSZLÓ VARGA[2]

One of the main challenges for environmentally responsible foundries that keep the health of the employees in mind is the decrease of emission values. The use of inorganic binders, i.e. water glass systems, in core production plays a significant role in the prevention of the release of toxic materials during production. The various developments in binder systems during the past years showed that the use of conventional organic binders can be an economically valid alternative to replace water glass binders. These developments almost solely focused on the fully modified water glass systems. Various researches and developments have been carried out for the successful use of inorganic binders.

Keywords: Inorganic binder, water glass solutions, regeneration, new sand

1. ALKALI-SILICATE SOLUTIONS

Water glass is not considered a standard compound but a collective term for various alkali-silicate melts and compounds that forms a glassy solid. The alkali salts of silica are also considered water glass. Water glass can be characterised with its module (SiO_2: Na_2O ratio), density and viscosity [1].

The module means the silica and alkali-oxide ratio of water glass. The general water glass composition can be described as: $x\mathrm{SiO_2} \bullet y\mathrm{M_2O} \bullet z\mathrm{H_2O}$, where M represents the alkali metals, such as sodium, potassium or lithium. The module of the most common sodium water glass used in the foundry industry, i.e. the SiO_2: Na_2O ratio, is 2.0–3.3. Certain technological properties of the moulding mixture and the binder system are influenced by the module [1], [2].

2. CORE PRODUCTION TECHNOLOGIES

Water glass binders have been successfully used during various manufacturing processes in the past. Water glass – CO_2 and water glass – ester methods are considered classic inorganic core-production technologies, during which various chemical processes are responsible for the setting [1]. Cores produced with these methods are not suitable for the modern market, because of their low strength, yield properties, knock-out ability and the limited reusability of the regenerated materials. New inorganic binder systems have been developed during the last 15 years, due to the new manufacturing processes and the developments in silicate chemistry. Chemical binding and drying are combined in most of the newly developed inorganic water glass based binding processes. The two main components of such systems are a liquid modified water glass binder and a powder-based additive [1], [2]. The commercially available binder systems are the following: Cordis binder system, Inotec binder

---

[1] Nemak Linz GmbH
Zeppelinstrasse 24, Linz, Upper-Austria 4030, Austria
Viktoria.Dargai@nemak.com

[2] Institute of Foundry, University of Miskolc
H-3515 Miskolc-Egyetemváros, Hungary
laszlo.varga.mak@gmail.com

system, AWB method, Laempe and Hydrobond processes. Inorganic binders can be used mostly for aluminium castings because of the low casting temperature. However, foundries are carrying out researches on the successful application of inorganic binders for iron casting production [1], [6].

3. REGENERATION TECHNOLOGIES

The aim of regeneration is to produce sand with similar properties to new sand which is reusable for core and form production [1], [3]. The regeneration of inorganic water glass bound core-sand mixtures poses a great challenge for foundries, as, dissimilarly to organic binders, the binder is not burnt out after casting. Various regeneration methods can be used for core-sand mixtures with inorganic binders. I.e. moist, thermal, mechanical and thermal-mechanical regeneration.

During moist regeneration, the used sand is washed in several steps. This technology is the most effective, as the silicate binder can be washed off of the sand particles. However, the technology is not in compliance with the ecological consideration of inorganic binders due to the high water and space demand, the issues of wastewater cleaning and the disposal of sludge. Furthermore, the sand needs to be dried as well. The industrial used of the technology is rather rare and no further developments have been made [1], [4].

Thermal regeneration can be used in case of water glass- ester binders. During burning, the organic components are burnt off of the surface of the sand. This regeneration method has high energy and space demand. Thus, the technology can be economic only for high volume production. It is used mostly for the regeneration of organic binder systems [1], [4], [5].

Lately, the use of mechanical regeneration equipment for the regeneration of inorganic binder based sands is getting more and more widespread. Mechanical abrasion is caused by either the different crusher balls or because of the friction between the particles. The space need of these devices is low, the operation is cheap and they can be easily incorporated into the system of any foundry [1], [4].

Furthermore, the combination of thermal and mechanical systems is also used by companies such as BMW [5], [6]. In these systems, a thermal step is included beside mechanical regeneration. This combination is also distributed by Scheuchel as a mass-production device. The investment costs are rather high because of the thermal regeneration block.

4. RESULTS AND DISCUSSION

During the experiments, new and reclaimed sand (from the first regeneration cycle) with similar inorganic binder and additive content, and mechanically reclaimed sand (from the first regeneration cycle) with various binder and additive content were used for the production of mixtures to compare. The inorganic binder system was made out of water glass binder and a powder additive. Measurement of three-point bending strength is commonly used as a basic characteristic property for moulding materials. Bending strength depends on the binder system used, its dosage as well as on properties of the base material used (chemical, mineralogical, grain shape, grain size). Three-point bending tests were carried out on test bars (170 × 22.5 × 22.5 mm) with various holding times and binder contents. The holding times were 30 sec, 1 hour and 24 hours after the production of test bars with a core shooter.

The bending strength of the mixtures from new and reclaimed sand with same binder and additive content is illustrated in *Figure 1*.

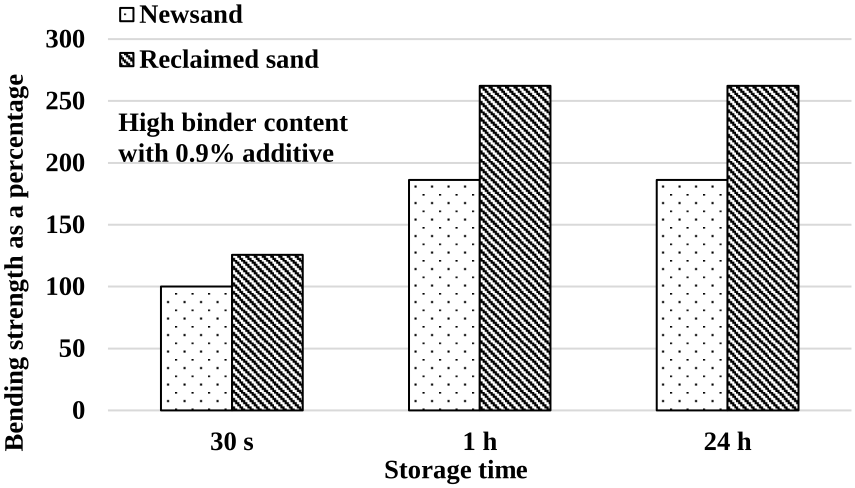

Figure 1
The bending strength of the mixtures from new sand and reclaimed sand with same binder and additive content

It can be observed that the bending strength values of the samples from regenerated sand with the same binder and additive content increased in all cases: with 20% at 30 s and 29% at 1 and 24 h. There was no significant difference between the bending strength in case of 1 and 24 h holding time.

The bending strength values of mixtures from reclaimed sand with similar additive and various binder content at different holding times can be seen in *Figure 2*.

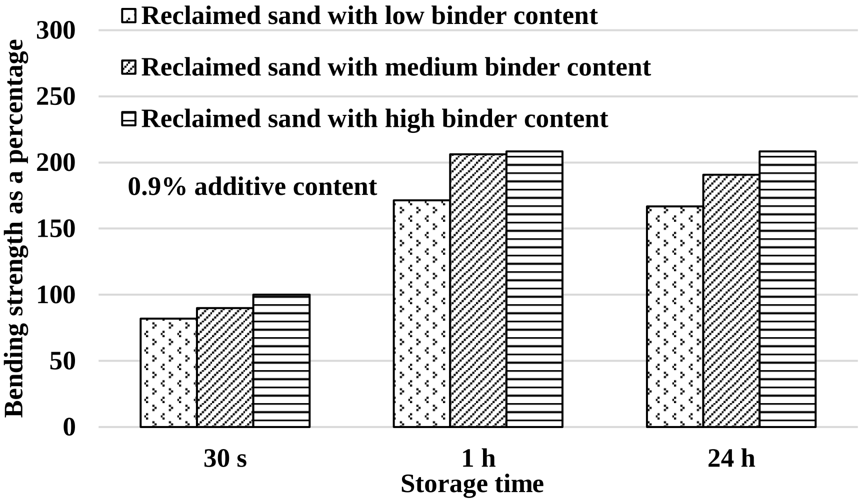

Figure 2
The bending strength values of mixtures from reclaimed sand with similar additive and various binder content

The decreased binder content led to lower bending strength. In case of the initial bending strength with the highest additive content, the bending strength of test bars decreased with 10% with medium binder content and 20% with low binder content. At 1 h holding time, the decrease in bending strength was 2% with medium and 18% with low binder content. The test bars with 24 h holding time exhibited 9% decrease in bending strength with medium binder content and 20% decrease with low binder content.

Figure 3 illustrates the bending strength values of mixtures form the mechanically reclaimed sands with similar binder and decreased additive content.

In case of the various additive contents, the mixtures with 30 s holding time exhibited significant differences. With 0.7% additive, the bending strength decreased with 8% and using 0.5% additive resulted in 17% bending strength decrease. The 1 h holding time resulted in approximately 3% strength decrease, and 7% in case of 24 h holding time.

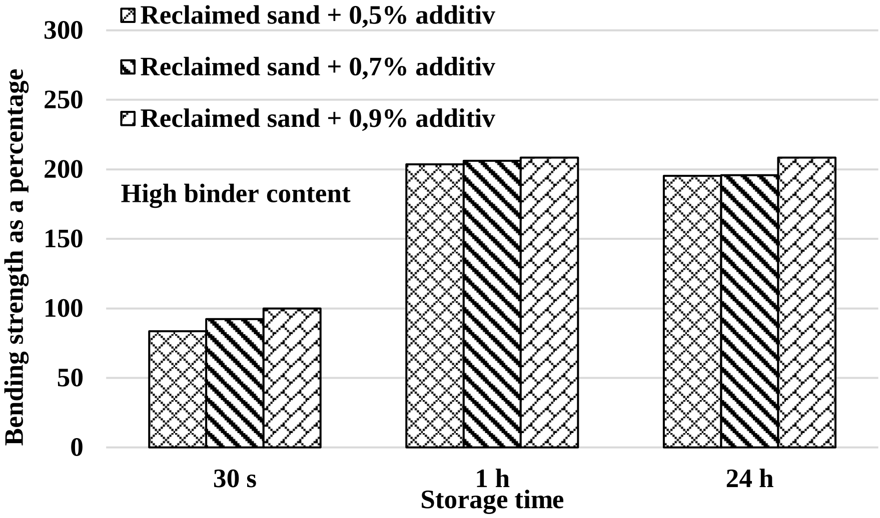

Figure 3

The bending strength of mechanically reclaimed sands with similar binder and decreased additive content

SUMMARY

In case of mixtures with the same binder and additive content, the use of reclaimed sand resulted in 29% higher bending strength, compared to the use of new sand. The bending strength values reach a maximum at 1 h holding time and decrease after 24 h. The decreased binder content had a greater effect on the bending strength values then the decreased additive content.

ACKNOWLEDGEMENT

The authors are grateful to Mária Ambrus for her advice.

REFERENCES

[1] H. Polzin (2014). *Inorganic binders for mould and core production in the foundry*. Germany, Schiele &Schön.

[2] Tóth L. (2011). *Forma és magkészítési ismeretek*. Oktatási segédlet.

[3] E. Flemming and W. Tilch (1993). *Formstoffe und Formverfahren*. Stuttgart, Deutscher Verlauf für Grundstoffindustrie, Leipzig.

[4] H. Polzin, P. Jaruszewski and J. Müller-Späth (2012). Die Regenerierung von Wasserglas-Ester-altsanden in einer mittelständischen Aluminium Gießerei. *Gießerei,* 99 S.70–81, 04/2012.

[5] Schwickal H., Hoffman H., Blümlhuber N. and Weissenbek E. (2009). Regenerierung von anorganisch gebundenen Gießereikernsanden. *Gießerei,* 96 S. 40–44, 11/2009.

[6] C. Wallenhorst (2010). Chemische Grundlagen der Anorganischen Bindemittel-Betrachtung der Kernherstellung auf molekularer Ebene. *Gießerei-Rundschau,* 57 S. 50–52.

Materials Science and Engineering, Volume 43, No. 1 (2018) pp. 31–41.

FLAME IMAGE PROCESSING AND ARTIFICIAL INTELLIGENCE AS A DIAGNOSTIC TOOL FOR INDUSTRIAL BIOMASS COMBUSTION

ATTILA GARAMI[1]–PÁL TÓTH[1,2]

The main objective of this work was to minimize emission levels and optimize thermal efficiency of a 3 MW, grate-fired biomass boiler without on-line fuel analysis systems by applying novel combustion process control based on routinely measured operating parameters and real-time flame image processing and machine learning. Two important tasks of image based combustion monitoring systems are providing alerts and predictions regarding the state of the system. The system issues alerts based on the location of the reaction zone and predicts boiler performance based on image and operating data.

Keywords: biomass, combustion, step-grate boiler, grate monitoring, flame imaging, machine learning

INTRODUCTION

Biomass is the oldest energy source in the history of mankind. Due to global climate change and depleting fossil fuel reserves, the incentive to move towards sustainable energy production has defined the last decade. Biomass is considered to be the only viable option for renewable energy generation that can meet global demand in the short-term – the annual availability of biomass is believed to be approximately equal to that of coal [5]. Considering forestry alone, the annually harvested 530 billion m^3 biomass has the potential to cover 10% of the world's power demand [18]. In the EU27 in 2010, of the approximately 3000 PJ of renewable energy generation for heating and cooling, biomass had a dominating share of approximately 91% – this decisive role is projected to remain in and after 2020 [2]. For heat and electricity generation from biomass, combustion is by far the most widespread technology, holding a share of over 90% [14].

Grate firing is the most widely used method for biomass combustion. When used for heat generation, grate-fired systems are normally limited to an output power of approximately 150 MW$_{th}$, which is not a disadvantage in certain decentralized industry segments. Flexibility in terms of fuel type and granularity further popularize the technology in smaller scale applications [22]. Grate-fired boilers are known to have lower efficiency compared to e. g., fluidized bed combustors [18], therefore, given the share of the technology in global renewable energy production, it is important to optimize their operation. Due to climate change and environmental issues, using low-quality and heterogeneous fuels or fuel blends has become a global trend [1]. Grate-firing technologies can potentially meet these requirements; however, the problems caused by using such fuels – such as reduced efficiency, increased emissions, slagging and fouling issues and poor flame stability – must be resolved [17].

The main objective of this work is to minimize emission levels and optimize thermal efficiency of a 3 MW, grate-fired biomass boiler without on-line fuel analysis systems by applying novel combustion process control based on routinely measured operating

---

[1] Department of Combustion Technology and Thermal Energy, University of Miskolc
H-3515 Miskolc-Egyetemváros, Hungary
attila.garami@uni-miskolc.hu

[2] RISE Bioekonomi / SP Energy Technology Center AB, Box 726, SE-941 28 Piteå, Sweden

parameters and real-time flame image processing and machine learning. Two important tasks of image based combustion monitoring systems are providing alerts and predictions regarding the state of the system. The system issues alerts based on the location of the reaction zone and predicts boiler performance based on image and operating data.

Historically, the reaction zone in step-grate combustors has not been monitored. Locating the reaction zone has several advantages. It provides information on the distribution of fuel over the grate, helps guarantee equal primary air supply to different regions of the grate and avoid the formation of “holes”, the elutriation of fly ash and unburned particles. The merits of a reliable boiler performance prediction system are obvious: operators can finetune parameters based on predicted future data. A prediction system can also alert for faulty operation as soon as it can be reliably predicted. To the best of the authors’ knowledge, no reports are available on the on-line monitoring and prediction of grate-fired biomass combustion.

1. MATERIALS AND METHODS

In this section, the boiler used for the experiments, the instrumentation and imaging system and the details of the data processing algorithms are discussed.

The approach can be best described as a combination of hardware and software elements. The hardware elements consisted of a camera and protective housing with a cooling system, an image acquisition and data transfer system and data processing hardware. The software component consisted of different modules for image processing, 3D reconstruction of the reaction zone and neural network prediction.

1.1. Boiler

Figure 1 shows a schematic drawing of the boiler used for the experiments. The boiler was a 3 MW nominal capacity, counter-current, inclined, stepping grate type combustor. The boiler was integrated into a sawmill process, producing heat for steaming timber products. Wood chips, by-products of the sawing process were used as fuel.

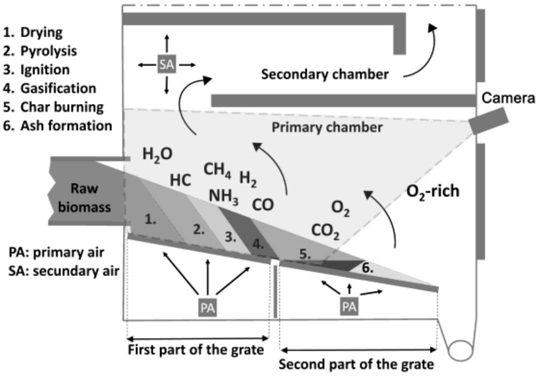

Figure 1

A schematic drawing of the 3 MW grate-fired biomass boiler used for the experiments. The location and field of view of the camera used for imaging is shown by the light gray area.

1.2. Instrumentation and imaging

The boiler was equipped with an on-line measurement system integrated into a distributed control system (DCS) that monitored several operational parameters, including chamber temperature, return and output water temperatures, fan speeds, boiler capacity and hydraulic pressures of the step-grate, fuel feeding and de-ashing systems. Additionally, high accuracy Vario Plus Industrial type continuous emission monitoring system (CEM) was used as a tool to monitor flue gas for simultaneous measurements of: O_2, CO_2, CO, NO_x components, gas temperature, differential pressure. Flame images were acquired by the current state-of-art, single CCD camera with response in the visible range of the spectrum [12]. The digital camera was a Basler Ace acA1300-22gc model. The camera utilized a global shutter CCD sensor. Images were acquired at a rate of 13 Hz. The duration of sampling was the same in all cases, 12 hours.

A high-temperature industrial pinhole lens was used for imaging the flame. The focal length of the lens was set at 3.6 mm, resulting in a field of view of approximately 80°. The lens had a 323 mm long stainless steel housing which enabled monitoring the combustion chamber by leading the lens through a hole in the refractory wall. The lens and the camera were protected by a tube-in-a-tube type cooling system. Compressed air was used as a coolant. Small holes in the front-end piece of the stainless-steel housing, outside of the first optical element in the lens, ensured positive pressures inside the pinhole lens, therefore avoiding dust deposition. The cooling system of the camera maintained lens and camera temperatures below 30 °C – the amount of air injected into the combustion chamber through the cooler was negligible. *Figure 2.a* shows an example flame image acquired by the installed camera with the locations of the fuel feeder and the grate.

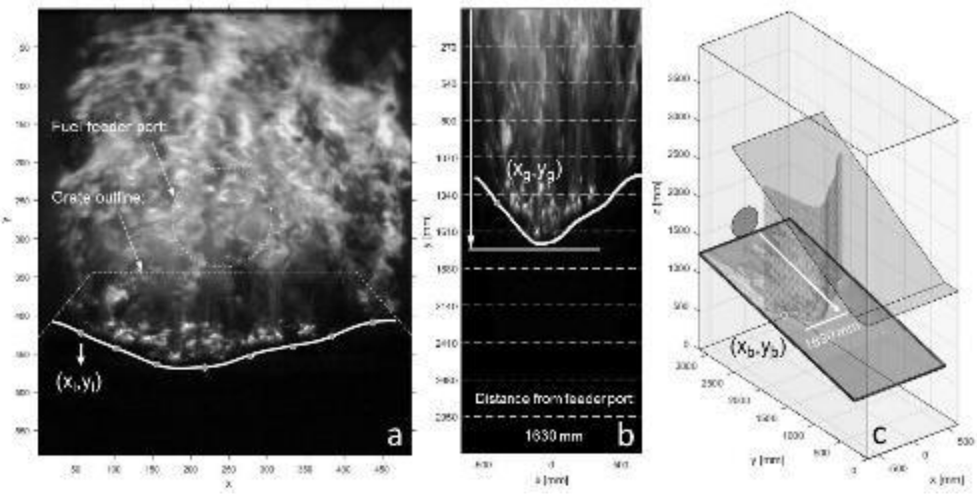

Figure 2

Localization of the reaction zone: a) located boundaries of the reaction zone with the fuel feeder and grate shown by white outlines; b) transformed coordinates of the reaction zone boundary in the coordinate frame of the grate. Dashed lines indicate the approximate location of grate elements; c) 3D reconstruction of the reaction zone in schematic drawing of the boiler.

1.3. Reaction zone monitoring: Image segmentation

As a first step, the raw image data was demosaicked [7] and the color channels (red, green and blue) were separated into different data vectors.

After that to locate the boundaries of the reaction zone, where the intensive burning takes place, the images were processed by segmentation algorithm. Since there may be some noise in flame images and sometimes the edge of the flame image is not very clear, it was detected by so called customized active contour model instead of conventional operators [23]. It is an energy minimizing, deformable spline influenced by constraint and image forces [13]. A typical result of this segmentation procedure is also shown in *Figure 2.a.* As demonstrated, the algorithm proved to be a robust and reliable method for the purpose of locating the reaction zone.

Then the acquired image, along with the coordinates of the reaction zone boundary, was transformed spatially to remove the effects of perspective distortion. This step ensured that the obtained spatial coordinates are in the coordinate frame of the grate *(Figure 2.b). Figure 2* illustrates the spatial transformation step. Therefore, real distance from feeder port can be easily defined by operator or control system. As seen, the obtained coordinates fit realistically into the coordinate frame of the grate. Finally, the 3D reconstruction of the reaction zone was carried out to visually be able to see where the reaction zone is located compared to the other parts of the chamber *(Figure 2.c).*

1.4. Prediction system: Image and operational parameter features

Since the images had a pixel resolution of 488 × 582 with an RGB bit depth of 24 bit, and the camera operated at 13 Hz, the image data rate was approximately 11 million 8-bit integers per second (which corresponds to 88 Mbit/s as opposed to the 1000 Mbit/s limit of the GigE standard).

Due to limited computing resources, an input space with a dimension of 488 × 582 × 3 cannot be handled in real time, therefore data reduction steps were necessary before feeding the inputs to the neural network. The data reduction process derives image features from the raw image data, namely from the ordered sets of pixel intensities corresponding to the color channels of the sensor. The parameters derived by the data reduction process are conventionally called learning features [3]. These features must be defined in a way so that the resulting feature set can be computed efficiently, while also conserving most of the information content of the images.

For the sake of simplicity, an image can be considered as a collection of radiometric measurements. Each pixel carries radiometric and spectral information (due to the selective color filters used in Bayer arrays), but also spatial information, since the spatial location from where a given sensor element collects data is known [10].

Several options for data reduction can be considered. In this study, statistical description was adapted as the data reduction method. To circumvent the loss of spatial data, features from the image gradient were also computed and added to the feature set.

After image pre-processing, the matrix form of the red channel was reconstructed in order to compute its smoothed spatial gradient [8]. From the spatial gradient, the gradient magnitude and orientation were computed and stored as vector data representing two virtual channels. In the second step, the first four statistical moments (the mean, variance, skewness and kurtosis) of each channel, including the two virtual channels, were computed. These statistical moments were used as image features, part of the feature set fed into the artificial neural network.

In the application described in this paper, the prediction scheme used was hybrid in the sense that it used features from both image and non-image data. The "non-image" part of the feature set consisted of routinely measured operational parameters by DCS. Previous studies reported the usage of similar hybrid schemes [21, 16, 15, 19].

Seven of the many recorded parameters were selected as inputs for the machine learning system: boiler capacity, output water temperature, return water temperature, flue gas O_2 content and the capacities of primary and secondary air fans. Operational parameters were collected at slower rates, therefore a piecewise constant extrapolation scheme was used to produce operational parameter values before a new set of measurements became available.

1.5. Prediction system: Artificial neural network

The artificial neural network (ANN) implementation used in this work was a type of fully connected, feedforward deep neural network. The role of the neural network was making predictions of the output water temperature. The predictions were made in a continuous multistep-ahead prediction scheme [6]. The predictions were computed for times-ahead up to approximately 28 minutes.

The set of inputs (27 learning features, as discussed in Section 2.4) were fed to a number of "blocks", each of which outputs a prediction for a given time-ahead. Each block can be considered as a separate deep multi-layer perceptron (MLP), independent of the other blocks.

Since the combustion process is assumed to be non-linear, non-unity activation functions were used in the presented ANN. Rectifiers were used as activation functions in all blocks. Neurons with the rectifier as their activation function are called rectified linear units (ReLU's).

The ANN implemented in this work can be considered a deep neural network. Deep neural networks are usually defined as MLP's that have more than one hidden layer and all neuron have non-linear activation functions.

In the ANN described in this paper, each block consisted of 5 hidden layers resulting in a total of 7 layers per block. Each layer contained 50 neurons. The width of the lines represents the weights associated with the connections. The network can be regarded as a collection of fully connected deep subnetworks, or blocks. Each input was connected to every top-level neuron of every block. The inputs were a set of 27 learning features. The outputs were predictions at different times ahead of the current instance. A total of 200 outputs were used, representing 200 discrete time bins ahead of the current time. Consequently, the number of blocks was also 200.

Several ANN architectures were implemented and tested, among which the presented architecture proved to be a good balance of architecture complexity and computational cost. The presented architecture can be trained and evaluated reasonably quickly, while still maintaining fairly low error.

In the present study, the training dataset was obtained in a 12-hour test campaign. The dataset contained all measured operational and image features. To train the network, "future" values of the output water temperature were paired with "present" values of the 27 learning features – in other words, a time lag between the input feature set and outputs was introduced representing the time-ahead values. The dataset acquired in the 12-hour campaign was split in half. One half was used for training, and the other was used for testing the predictive power of the ANN.

The neural network was trained using the stochastic gradient descent method (SGD) [4], with mean square error as a loss function and a sample size of 50,000. The learning rate was set to 0.01. In order to avoid overfitting, L2 regularization was used. Learning rate decay and momentum strategies were not used [11]. The neural network was implemented in Python 2.7, using the Theano machine learning framework [20].

2. RESULTS AND DISCUSSION

2.1. Validation of the segmentation algorithm

In this section the robust and reliable operation of the proposed algorithm were demonstrated by observing the changes of the obtained reaction zone coordinates.

Figure 3 illustrates the capability of the proposed system to follow quick changes in the reaction zone location following fuel feeding or grate motion events.

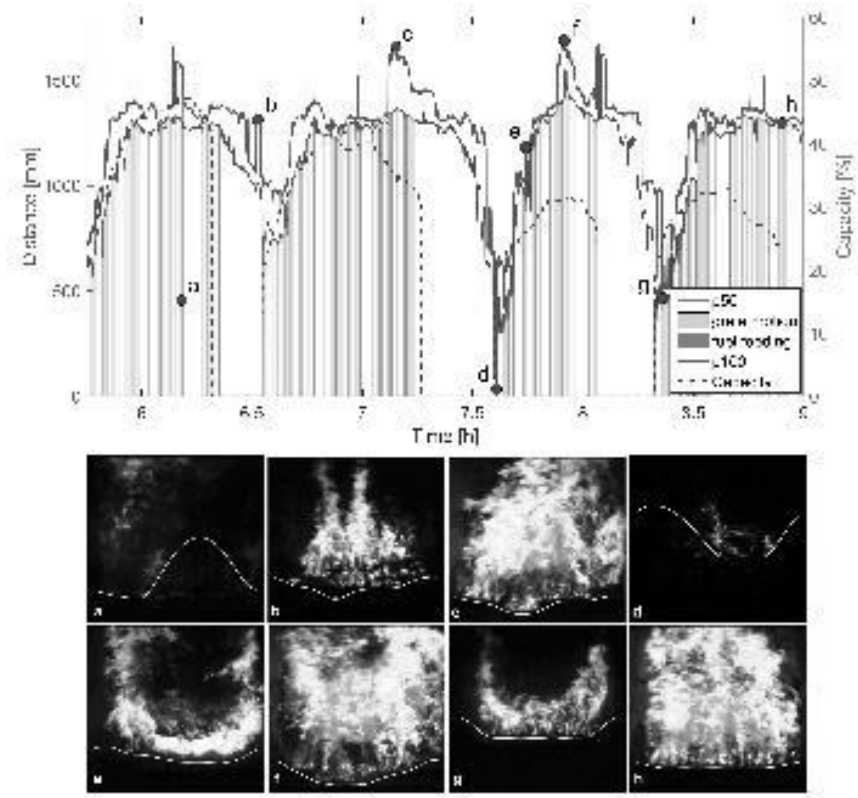

Figure 3

Changes in 50th (p50) and 100th (p100) percentile of the y coordinates of the reaction zone boundaries with binary fuel feeding and grate motion signals as a function of time. Marked points indicate time instances at which the images of the second row were captured. The snapshots demonstrate typical issues encountered in the operation of the monitoring system: a) reduced flame luminosity caused by a momentary cutoff in combustion air supply due to grate motion; b)–c) a displacement of a small portion of the bed due to grate motion; d) this event signifies the complete extinction of the flame due to the temporarily diminished dynamic load of the boiler; e)–g) these events are shown to demonstrate that although sharp changes are observed in the percentile values, the algorithm correctly detected the reaction zone boundary.

In the top row of the *Figure 3*, the motion of the grate elements, fuel feeding, 50th (p50) and 100th (p100) percentile of the y coordinates of the reaction zone boundaries and the boiler capacity are shown as a function of given time period during the measurements. The grate motion and the fuel feeding signals are logical signals, thus they only represent on/off events. As seen, the reaction zone coordinates followed the signals. The reaction zone migrated away from the feeding port when fuel was fed or the grate was moved, and receded towards the feeding port when there were no signals. Consequently, the calculated boiler capacity signal was zero at these times, indicating no injection of combustion air.

In the second row of the *Figure 3*, a)–g) show snapshots of the combustion chamber, taken at times indicated by markers in the time histories. The purpose of these snapshots is to illustrate and explain typical detection issues encountered during operation: a) reduced flame luminosity caused by a momentary cutoff in combustion air supply due to grate motion; b)–c) a displacement of a small portion of the bed due to grate motion; d) this event signifies the complete extinction of the flame due to the temporarily diminished dynamic load of the boiler; e)–g) these events are shown to demonstrate that although sharp changes are observed in the percentile values, the algorithm correctly detected the reaction zone boundary.

In summary, the proposed system reliably captured the motion of the reaction zone, with minor issues that could be easily identified and filtered out. Furthermore, the system was able to identify extreme operating states and undesirable fuel distribution that may lead to decreased efficiency and reduced grate lifetime.

2.2. Further research on the reaction zone location

Relationships between image flame features and combustion performance parameters are receiving added attention because of their potential in monitoring and control applications. Based on the observed empirical correlations, model-based controllers can be realized [9].

The relevance of locating the reaction zone coordinates was further demonstrated by exploring the correlation between selected, relevant operational parameters and the reaction zone location.

When computing the linear correlation coefficient between the percentile measures of the reaction zone boundary coordinates and selected parameters, it was found that the coefficients were above 0.8 for most percentiles and the major flue gas constituents. The correlation coefficients between the flue gas and combustion chamber temperature and reaction zone boundary coordinate percentiles were between 0.6 and 0.2, respectively, while the correlation was approximately or weaker than 0.2 for the pollutant concentrations. However, when recomputing the correlation coefficients with the time lag between signals removed via cross correlation analysis, the correlation coefficients increase to above 0.8 in the case of flue gas temperature, above 0.6 in the case of combustion chamber temperature and to approximately 0.3 in the case of pollutants *(Figure 4)*. This suggests that the percentile values of the obtained reaction zone coordinates can be used for estimating other, relevant operational parameters or for control purposes, based on the selected operational or emission parameters. Since the time lags are mostly functions of the inherent properties of the monitored system and persistent operating practices, they can be estimated easily during operation and the signals can be adjusted accordingly. In this case, the obtained correlation coefficients suggest that even the relationship between the pollutants and reaction zone boundary coordinates can be sufficient for monitoring or control purposes.

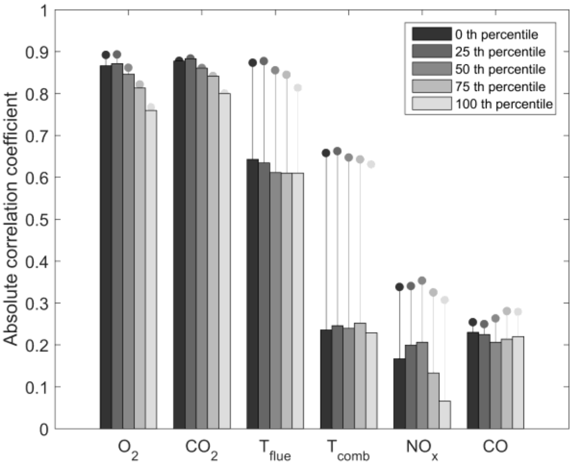

Figure 4

Absolute linear correlation coefficients between emission parameters and reaction zone location percentile values. Stems show correlation coefficients recomputed after the estimated time lag between signals had been removed.

2.3. Evaluation of the prediction

To assess the usefulness of the presented deep ANN learning scheme in predicting the output of the grate-fired biomass combustion system, the accuracy of the predictions can be evaluated by calculating deviations relative to measured outputs. The deviations can be expressed in terms of standard errors. The magnitude of these standard errors provide insight on the achievable fidelity of predictions.

Figure 5 shows typical prediction results obtained in an experimental campaign. Each plot shows a different, approximately 28 minutes-long scenarios. The solid black lines show the actual measurements in 20 scenarios. Shaded areas indicate the probability density of predictions made at time = 0 up to a time-ahead of approximately 28 minutes. Note that all shown time-ahead predictions were available at time = 0 in every given scenario. Bars show the feature spaces at time = 0. As seen, the predictions are fairly accurate and reproduce general trends. The errors and thus uncertainty increase with the time-ahead.

After training the ANN, the prediction performance was evaluated by using a test dataset acquired in the experimental campaign described. The accuracy of prediction was evaluated based on the root mean square error (RMSE) of predictions compared to the test dataset, as a function of time-ahead.

Figure 5 shows the RMSE of predictions as a function of time-ahead. As seen, the errors remain very low at time-ahead below 5 minutes – however, in this region, the accuracy of prediction decreases quickly. After a time-ahead of 5 minutes, the errors increase slowly up to an RMSE of approximately +/–1 °C at a time-ahead of 28 minutes.

After a time-ahead of approximately 28 minutes, the RMSE of predictions was found to increase rapidly, with the predictions becoming unrealistic, in some cases unable to follow general trends. This is probably due to the typical cycle time of the boiler in the training data, which was 20–50 minutes. Most likely, the ANN learns typical operation patterns including cycle times. The ANN utilizes these learned patterns for producing long-term predictions.

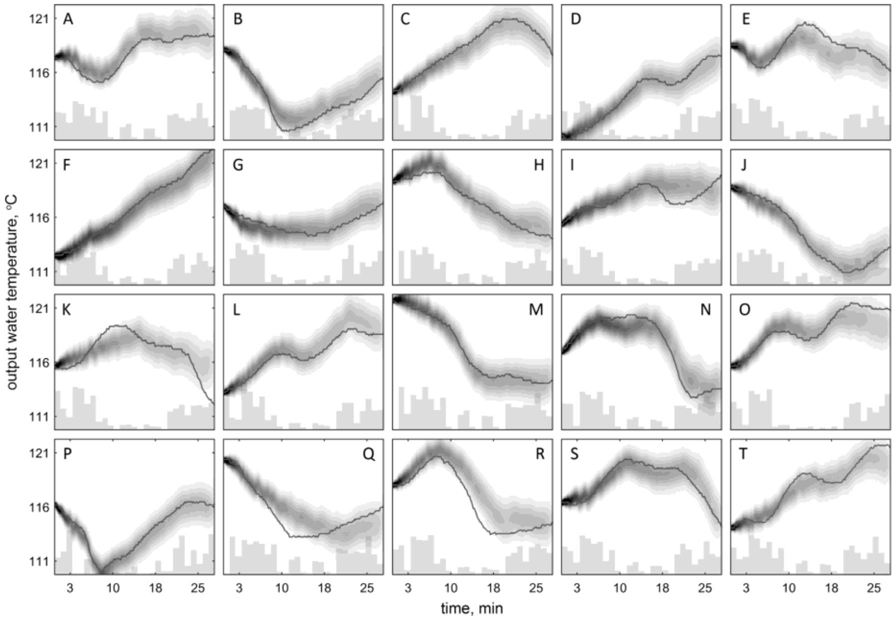

Figure 5
Deep ANN-based prediction of output water temperatures

SUMMARY

The main objective of this work is to minimize emission levels and optimize thermal efficiency of a 3 MW nominal capacity, step-grate fired biomass boiler without an on-line fuel analysis system by applying novel combustion process control based on routinely measured operating parameters and real-time flame image processing and machine learning. Two important tasks of image based combustion monitoring systems are providing alerts and predictions regarding the state of the system. The system issues alerts based on the location of the reaction zone and predicts boiler performance based on image and operating data. Using image processing of the acquired flame images, the edge of the reaction zone inside the boiler can be monitored. The accuracy of the system was demonstrated. We showed that there is strong correlation between the location of the reaction zone and emission and operating parameters. Using image data and a trained deep neural network, the results indicate that the proposed learning scheme can reliably predict output water temperatures with errors +/–1%, up to roughly 30 minutes ahead of the current time. The error depends on the time-ahead of the predictions. Without including image data, the errors were around +/–5%. To the authors' knowledge, neither reaction zone monitoring, nor neural network prediction methods were applied to optimize step-grate combustion, thus the custom algorithms are all part of the novelty of the work.

ACKNOWLEDGEMENTS

The described study was supported by the UNKP-17-3 New National Excellence Program of the Ministry of Human Capacities and carried out as part of the EFOP-3.6.1-16-00011 "Younger and Renewing University – Innovative Knowledge City – institutional development of the University of

Miskolc aiming at intelligent specialisation” project implemented in the framework of the Szechenyi 2020 program. The realization of this project is supported by the European Union, co-financed by the European Social Fund.

REFERENCES

[1] Javier Ballester and Tatiana Garcá-Armingol (2010). Diagnostic techniques for the monitoring and control of practical flames. *Progress in Energy and Combustion Science*, 36 (4), 375–411.

[2] Manjola Banja, Fabio Monforti-Ferrario and Nicolae Scarlat (2013). Review of technical assessment of national renewable energy action plans. *JRC*, EUR, 25757.

[3] Christopher M Bishop (2006). Pattern recognition. *Machine Learning*, 128.

[4] Léon Bottou (2010). Large-scale machine learning with stochastic gradient descent. *Proceedings of COMPSTAT’2010*, pp. 177–186. Springer.

[5] Toby G. Bridgeman, Jenny M. Jones, and Alan Williams (2010). Overview of Solid Fuels, Characteristics and Origin. Wiley-VCH Verlag GmbH & Co. KGaA.

[6] Haibin Cheng, Pang-Ning Tan, Jing Gao, and Jerry Scripps. Multistep-Ahead Time Series Prediction, pages 765–774. Springer Berlin Heidelberg, Berlin, Heidelberg.

[7] Adrian Davies and Phil Fennessy (2001). *Digital imaging for photographers*. Taylor & Francis.

[8] Rafael C. Gonzalez and Richard E. Woods (2007). *Image processing. Digital image processing.* 2.

[9] A. González-Cencerrado, B. Peña, and A. Gil (2012). Coal flame characterization by means of digital image processing in a semi-industrial scale pf swirl burner. *Applied energy*, 94, 375–384.

[10] A. González-Cencerrado, B. Peña, and A. Gil (2012). Coal flame characterization by means of digital image processing in a semi-industrial scale PF swirl burner. Applied Energy, 94, 375–384.

[11] Ian Goodfellow, Yoshua Bengio, and Aaron Courville (2015, 2016). Deep learning.

[12] R Hernandez and J Ballester (2008). Flame imaging as a diagnostic tool for industrial combustion. *Combustion and flame*, 155 (3), 509–528.

[13] Michael Kass, Andrew Witkin, and Demetri Terzopoulos (1988). Snakes: Active contour models. *International journal of computer vision*, 1 (4), 321–331.

[14] Jaap Koppejan and Sjaak Van Loo (2012). *The handbook of biomass combustion and co-firing*. Routledge.

[15] Xinli Li, Duo Sun, Gang Lu, Jan Krabicka, and Yong Yan (2012). Prediction of NOx emissions through flame radical imaging and neural network based soft computing. *2012 IEEE International Conference on Imaging Systems and Techniques Proceedings*, pp. 502–505. IEEE.

[16] Bao Lin and Sten Bay Jørgensen (2011). Soft sensor design by multivariate fusion of image features and process measurements. *Journal of Process Control*, 21 (4), 547–553.

[17] G. Lu, G. Gilabert, and Y. Yan (2005). Vision based monitoring and characterisation of combustion flames. *Journal of Physics*: *Conference Series*, Volume 15, p. 194, IOP Publishing.

[18] Lasse Rosendahl (2013). *Biomass combustion science, technology and engineering*. Elsevier.

[19] Duo Sun, Gang Lu, Hao Zhou, and Yong Yan (2013). Condition monitoring of combustion processes through flame imaging and kernel principal component analysis. *Combustion Science and Technology*, 185 (9), 1400–1413.

[20] Theano Development Team (2016). *Theano: A Python framework for fast computation of mathematical expressions*. arXiv e-prints, abs/1605.02688, May 2016.

[21] F. Wang, X. J. Wang, Z. Y. Ma, J. H. Yan, Y. Chi, C. Y. Wei, M. J. Ni, and K. F. Cen (2002). The research on the estimation for the NOx emissive concentration of the pulverized coal boiler by the flame image processing technique. *Fuel*, 81 (16), 2113–2120.

[22] Chungen Yin, Lasse A. Rosendahl, and Søren K. Kǣr (2008). Grate-firing of biomass for heat and power production. *Progress in Energy and Combustion Science*, 34 (6), 725–754.

[23] Jinhua Zhang, Jian Zhuang, Haifeng Du, Xiaohu Li et al. (2006). A flame detection algorithm based on video multi-feature fusion. *International Conference on Natural Computation*, pp. 784–792. Springer, 2006.

Materials Science and Engineering, Volume 43, No. 1 (2018) pp. 42–53.

CURRENT RESEARCH TRENDS IN FOAMED CONSTRUCTION AND BUILDING MATERIALS: A REVIEW

RÓBERT GÉBER[1]–ISTVÁN KOCSERHA[2]

Concrete is the most widely used building material in the world today. Thanks to its excellent properties *(mechanical strength, workability, durability)* and long service life it can be used as a building material in various forms *(for example as frame structure, wall unit, beams, blocks)*. Special foaming techniques and curing methods can be used to produce low density lightweight concretes, and excellent thermal insulating materials, as well.

At the same time for the production of cement, which is the binder material of concrete, not only a large quantity of mineral deposit, but high energy consumption is needed. The quantity of raw materials available is limited and the production of cement evolves significant amount of CO_2 which contributes to the greenhouse effect. Therefore, researches are undergo to develop materials and technologies that offer solutions to reduce raw material consumption and energy consumption, and to increase the use of secondary raw materials and different waste materials. One possible application area could be geopolymers, which can be produced mainly from secondary raw materials.

The aim of this paper is to review the research trend of foamed construction and building materials and materials systems used today with autoclaving technology. This paper also contributes to the research work of foamed thermal insulating materials which is currently undergo with the co-operation of Institute of Ceramics and Polymer Engineering and Institute of Raw Material Preparation and Environmental Processing at the University of Miskolc.

Keywords: autoclave, construction material, concrete, geopolymer, geopolymer foam

1. INTRODUCTION

1.1. The most common building material: concrete

Concrete is the largest quantity of building material produced in the world. Cement is the binder material of concrete, the largest producing countries are China, India, the USA, Vietnam, Turkey, respectively. China is responsible for more than half of the world cement production [1]. However, the quantity of raw materials, which are needed to produce cement, is limited. According to the report *Cement production in vertical shaft kilns in China – Status and opportunities for improvement* [2] the quantity of limestone available for the production exclusively of cement, taking into account the current growth in cement production, is sufficient for 59 years in China. However, there are some difficulties of cement production:

- the quantity of raw minerals available *(clay, sand, limestone)* is limited;
- a significant amount of energy consumption is needed for the production of cement;

---

[1] Institute of Ceramics and Polymer Engineering, University of Miskolc
H-3515 Miskolc-Egyetemváros, Hungary
robert.geber@uni-miskolc.hu

[2] Institute of Ceramics and Polymer Engineering, University of Miskolc
H-3515 Miskolc-Egyetemváros, Hungary
istvan.kocserha@uni-miskolc.hu

- during the production of cement evolves a large quantity of CO_2 *(about 8% of global CO_2 emissions).*

The classification of concrete is possible on the basis of its physical and mechanical *(e. g. bulk density, consistency, compressive strength, environmental exposure)* properties. According to its bulk density concrete can be classified as [3]:

- Lightweight concrete, LC: ρ = 800–2,000 kg/m^3
- Concrete, C: ρ = 2,001–2,600 kg/m^3
- Heavy concrete, HC: ρ > 2,600 kg/m^3

As this paper focuses only on concrete and other types of building materials produced by foaming technology, the Authors would like to focus on the construction of lightweight concrete and other foamed or aerated building materials in more detail.

Table 1 contains the comparison of conventional concrete *(C)* and other artificial construction materials *[aerated concrete (AC), autoclaved aerated concrete (AAC), geopolymers and geopolymer foams]* on the basis of raw materials, manufacturing technology, curing conditions and application areas.

Table 1

Comparison of ordinary and artificial construction materials and their foams

Construction material	Raw materials	Manufacturing technology	Curing conditions	Application areas
Concrete	water, cement, sand, aggregates	casting, moulding, pumping	in water or in steam; curing time: 28 days	buildings, roads
Aerated Concrete, AC	water, cement/lime, foaming agent (Al powder, H_2O_2, calcium carbide liberate hydrogen, oxygen and acetylene, synthetic foam, enzyme-based foaming agent)	mechanical foaming: • in-mixed foaming pre-foamed method; chemical foaming: • air-entraining method (gas concrete); • casting into mould, • pumping	• in ambient conditions, • in steam at 70 °C	thermal insulation material, filling voids, ground stabilization, buildings, shock-absorbing buildings
Autoclaved aerated concrete, AAC	Water, cement, lime, sand/fly ash type F, foaming agent (Al powder or paste)	casting into mould	in autoclave under high temperature (~T = 190 °C) and pressure (0.8–1.2 MPa)	insulation material, building block, building beam
Geopolymer	Aluminosilicate minerals (metakaolinite/fly ash, granulated blast furnace slag, waste glass, red mud, construction and demolition waste), alkaline activator	casting into mould, vibration	in air, T = 25 °C–95 °C, curing time max.: 7 days	building blocks, insulation materials, geopolymer cement, tiles, fire-proof coatings

Construction material	Raw materials	Manufacturing technology	Curing conditions	Application areas
Geopolymer foam	Aluminosilicate minerals (metakaolinite/fly ash, granulated blast furnace slag, waste glass, red mud, construction and demolition waste), alkaline activator, foaming agent (Al powder; diluted surfactant solution)	• high temperature processing; • low temperature mixing method; • chemical foaming technique; • silica fume in situ foaming technique; • mechanical pre-foaming technique	in air, T = 20 °C–150 °C; high pressure, high vacuum; curing time max.: 7 days	insulation materials, tiles, bricks

1.2. Lightweight concretes

Lightweight concretes can be classified according to several criteria. The most commonly used method is the classification of concrete according to its raw materials and manufacturing technology. Thus, we differentiate [4], [5]:

- lightweight aggregate concrete *(LAC)*;
- cellular lightweight concrete *(CLC)*;
- no-fines concrete.

Cellular Lightweight Concrete *(also known as aerated, foamed or gas concrete)* is a lightweight concrete which, according to its manufacturing technology, is classified into two groups: 1. foamed concrete, or non-autoclaved aerated concrete *(NAAC)* and 2. autoclaved aerated concrete *(AAC)* [5].

NAAC: this type of lightweight concrete *(cement paste or mortar)* produced by the use of organic, or synthetic foams or protein-based foams. Depending on the quantity of foam used, bulk density of the foam concrete may vary between wide limits *(between 500 and 1,600* kg/m^3*)* [6], [7]. Two different method is known for producing NAAC:

- In-mixed foaming: the foaming agent is mixed in the mixer by adjusting high rotation to generate air bubbles. All of the raw materials are added to this prepared foam, then mixing is continued. This method, thanks to its simple implementation, is widely used [8]. The disadvantage of this method is that, there are a lot of fractured pores within the foam concrete, therefore it cannot be prepare a homogenous foam structure.
- Pre-foamed: during the method a water-soluble foam material is produced by compressed air and the foam is added to the concrete. This is a costly technique, than the in-mixed foaming technique, but a more stable and homogenous foam structure can be achieved [9].

AAC: manufactured by chemically expansion. For the production of AAC cement and lime are used as binders, high silica sources *(mainly quartz sand or fly ash)*, water and pore-forming agent *(mainly aluminum powder or paste)* are used, as well. In the aspect of the quality of the AAC product, chemical composition, quantity and the particle size of raw materials are of particular importance.

During the production of AAC a dilute concrete slurry, which are made from the above mentioned raw materials, poured into a mould, after that the pore-forming agent *(Al powder or paste)* is added to the slurry. At this time aluminum reacts with water and hydrated lime (1) and due to the evolved hydrogen gas a specific foam structure is generated.

$$2\ \mathrm{Al} + \mathrm{Ca(OH)_2} + 6\ \mathrm{H_2O} = \mathrm{Ca(Al(OH)_4)_2} + 3\ \mathrm{H_2} \tag{1}$$

In order to achieve the proper strength of AAC it is also necessary to use autoclaving technology. After a pre-curing method AAC samples are placed in a pressure vessel *(so-called autoclave)*, where high temperature *($T \approx 190$ °C)* and high pressure *($p \approx 1.0$–1.2 MPa)* are used to cure the sample. Thanks to this curing method, crystals of tobermorite mineral, which give the required strength of AAC, are formed. AAC is environmentally friendly, acts as an inert material, non-toxic and it does not contribute to the indoor air pollution syndrome [10].

CLC have an edge on AAC, that it does not require autoclave curing, making it economically advantageous. However, according to Panesar [11] the properties and application areas are highly effected on the type and manufacturing method of foam and its properties.

1.3. Geopolymers, as alternatives to conventional concrete

Geopolymers can be alternative materials for substituting conventional concrete [12], [13], [14]. In fact, these materials are inorganic polymer-structured artificial binders. For the production of geopolymers aluminosilicate materials and alkali activator are required. Mixing these raw materials and activators together, during an exothermic reaction "artificial stone" is formed. Beside metakaolinite numerous industrial wastes, construction & demolition wastes *(e. g. cuttings, fly ash, blast furnace slag, brick powder)* can be used [15], [16], [17], [18], [19], [20], [21]. Geopolymers are very popular materials today, because of their excellent properties *(fire and heat resistance, excellent mechanical strength, low shrinkage, excellent immobilising capability of heavy metals).*

Similarly in concrete foaming technologies, these methods can also be used to produce heat-insulating materials from geopolymers [15], [16], [17], [18], [19], [22], [23]. As it was formerly mentioned, in the case of different types of concrete, the improvement of the insulating capacity has been suggested to widen the scope of application of geopolymers. *Table 2* summarizes some researches, which are carried out on the production of foamed geopolymers.

Table 2

Researches dealing with the foaming of geopolymers

Ref.	Material	Raw materials	Foaming agent
[15]	Geopolymer foam concrete, GFC	Metakaolinite, Fly ash	Al paste
[16]	Geopolymer foam, GF	Metakaolinite, potassium hydroxide	H_2O_2, olive oil, sunflower oil, canola oil as stabilizer
[17]	Geopolymer foam concrete, GFC	Fly ash (class F), granulated blast furnace slag, sodium hydroxide, sodium silicate	Diluted aqueous surface active concentrate; foaming with air pressure foam generator
[18]	Geopolymer eco-cellular concrete (GECC)	ordinary portland cement (OPC), fluid catalytic catalyst (FCC), sodium hydroxide, sodium silicate	Commercial aluminium powder, recycled aluminium foil

Ref.	Material	Raw materials	Foaming agent
[19]	Aerated metakaolinite-based geopolymers (AMKG)	metakaolinite, waterglass, sodium hydroxide	Al powder, incinerator bottom ash (IBA)
[22]	IBA aerated geopolymer	incinerator bottom ash (IBA), mixture of sodium hydroxide solution and waterglass	Incinerator bottom ash (IBA)
[23]	Alkali-activated fly ash foam (FAF)	Fly ash (class F), sodium hydroxide	Al powder
[24]	Oil palm shell foamed geopolymer concrete	Fly ash (class F), palm oil fuel ash (POFA), sodium hydroxide, polycarboxylate ether (superplasticizer)	Sika AER-50/50 (blend of synthetic surfactants and polymer)
[25]	Geopolymer fly-ash based foam	Fly ash (class F), waterglass, sodium hydroxide	Al powder and H_2O_2

As described in *Table 2*, beside the raw materials of traditional geopolymers *(metakaolinite, fly ash)*, researches are focus on the utilization of other secondary raw materials, industrial wastes *[incinerator bottom ash (IBA), ground granulated blast furnace slag (GBFS), recycled aluminum foil]* as geopolymer raw materials, or as foaming agents *(IBA, recycled aluminum foil or other commercial foaming agents*). In the aforementioned researches, autoclaving has not been used for curing foamed geopolymers. It should be noted that the designation of foamed geopolymers are not yet standardized, the names of the developed materials are arbitrarily selected by researchers *(e. g. GF, GFC, GECC, AMKG)*.

2. AUTOCLAVING OF BUILDING MATERIALS

2.1. Autoclaved aerated concretes

Different industrial raw materials can be used for the production of aerated concrete with the use of autoclaving technology, through hydrothermal reactions. Autoclaving is a crucial technological step in the formation of crystalline tobermorite mineral, which responsible for the proper strength of AAC.

According to Mostafa [26] the intensity of formation of tobermorite phase is not change after 2 hours of autoclave curing anymore. However, Kunchariyakun et al. [27] also demonstrated that increasing the curing time in autoclave from 8 hours to 18 hours does not increase the quantity of tobermorite phase. Thus, material structure and mechanical properties of AAC are no longer improved after 8 hours of autoclave curing.

Shrinkage of AAC is influenced both by curing method and curing time, autoclaving pressure, the fineness and mineral composition of SiO_2, the geometry and dimensions of prepared sample and storage time [26]. Researchers also found that the presence of Al^{3+} used to foam AAC accelerates the formation of tobermorite crystals, and a lower curing temperature and a shorter curing time are sufficient to produce the corresponding crystal structure.

Table 3

Raw materials and autoclave conditions of some AACs

Ref.	**Used materials**	**Other curing method**	**Autoclave conditions**		
			Temperature [°C]	**Pressure [MPa]**	**Curing time [h]**
[26]	S, L, OPC, W, air-cooled slag, Al powder	after autoclaving: T = 50 °C for 24 hours	183	1	2, 6, 12, 24
[29]	FA (class F), SF, OPC, G, L, W, Al powder	after casting: T = 60–70 °C for 1 hour	no data	(a) 0.115, 0.4, 0.8 and (b) 1.15	(a) 8 and (b) 12
[30]	OPC, L, RS, FA (class F), Al powder	after autoclaving: immersing the specimens in water for 72 hours then T = 30 °C and relative humidity set to 45%	no data	0.98	10
[31]	FA (high calcium high sulfate), L, OPC, G, W, Al paste, modifier	after casting: T = 40 °C for 4 hours	no data	no data	10
[32]	CT, BFS, QS, cement clinker, G, W, Al powder, naphtalene as superplasticizer	after casting: T = 48 °C for 12 hours in steam	no data	1.35	8
[33]	OPC, RS, BA, W, Al powder, $Ca(OH)_2$	after autoclaving:specimens were cured in air until 7 days	126	0.14	6
[34]	cement, carbide slag, RS, W, Al paste, naphthalene-high efficiency water reducing agent	after casting: T = 50 °C for 4 hours; after autoclaving: T = 105 °C for 2 hours	145–220	no data	8–18
[35]	GBFS; OPC, waterglass activator, W	none	100, 200, 300	no data	24

Ref.	Used materials	Other curing method	Autoclave conditions		
			Temperature [°C]	**Pressure [MPa]**	**Curing time [h]**
[36]	GBFS (alkali-activated), waterglass, QP, W	none	170	0.8	0.5; 1; 4; 6; 10
[37]	OPC, L, QS, G, W, water hyacinth fiber, polypropylene fiber, Al powder	after autoclaving: T = 75 °C for 24 hours (drying the specimens)	180–190	1.0–1.2	8
[38]	OPC, QL, S, rice husk ash, W, Al powder	after casting: T = 40 °C for 3 hours; after autoclaving: T = 40 °C for 24 hours	180	no data	8; 18
[39]	FA, G, OPC, L, W, Al powder, polycarboxylic admixture	After casting: T = 50 °C in steam for 3 hours	180	1	12
[40]	OPC, clayish crushed stone, W, Al powder	none	180	1.0	12
[41]	OPC, SL, ash-slag mixture, W, Al powder	none	185	1.2	1.5 + 1.5 + 6 + 1.5 h (preliminary heating, vacuuming + rise of temperature + isothermal holding + cooling)
[42]	no data	none	180–190	1.0–1.2	8
[43]	CBP, OPC, S, L, Al powder	After casting: T = 40 °C for 3 hours	180–200	1.2	18

Ref.	Used materials	Other curing method	Autoclave conditions		
			Temperature [°C]	Pressure [MPa]	Curing time [h]
[44]	OPC, BL, S, G, waste glass (CRT cullet, glass cullet, calsiglass), W, Al powder	after casting: T = 60 °C for 5 hours	190	1.2	6
[45]	Z, OPC, L, QS, W, Al powder	none	200	1.15	12

Abbreviations: FA: fly ash; SF: silica fume, OPC: ordinary portland cement; G: gypsum; W: water, L: lime; RS: river sand; CT: copper tailings; BFS: blast furnace slag; QS: quartz sand; QP: quartz powder; BA: bottom ash; GBFS: ground granulated blast furnace slag; QL: quick lime; S: sand, SL: slaked lime; CBP: clay brick powder; BL: burnt lime; Z: zeolite

2.2. Autoclaving of geopolymer foams

Till today, according to the references few researches are found in the relevant literature concerning the production of foamed geopolymer cured with autoclave. *Table 4* summarize the curing methods, curing conditions and some results of autoclaved geopolymers.

Table 4

Curing method, conditions and some results of autoclaved geopolymers

Ref.	Curing method	Curing conditions	Result of curing
[46]	Climatic chamber or furnace or autoclave can be used for harden the geopolymer at higher temperatures.	T_{min} = 40 °C	curing time of geopolymer is shorter
[47]	Autoclave curing	T = 80 °C–120 °C; p = 0.1 MPa; curing time: 4–48 hours	density of geopolymer can be achieve: 1,000–1,700 kg/m^3
[48]	Autoclave curing	T = 150 °C; p = 2 MPa; curing time: 3 hours	compressive strength was increased
[49]	Heating chamber or hot air oven or autoclave	T = 80 °C; p = 2.05 MPa; curing time: 1–24 hours	increase in compressive strength; decrease in thermal conductivity
[50]	Autoclave curing	T = 150 °C; curing time: 2 hours	increase in compressive strength

Keulen and Kakebeeke [46] patented a preparation method that suitable for producing geopolymers with the use of sugar and/or organic acids *(curing time = 24 hours, curing temperature: minimum 40 °C)*. As the curing temperature increases, hardening of geopolymers can be reduced and, according to their opinion, this can be achieved by using an oven, a climate chamber or an autoclave.

Hao and Qin [47] patented the preparation method of geopolymer-based fiberboard. As raw material red mud was used. According to their method geopolymer paste is placed into an autoclave using the following conditions: T = 80 °C–120 °C; p = 0.1 MPa; curing time: 4–48 hours. Using this method they achieved a final product of 1,700 kg/m^3 of bulk density.

Bondar et al. [48] carried out tests on geopolymer cements, which were produced by various mineral additives *(kaolinite, hydrated lime, pozzolanic materials and andesite)* as raw materials. Their results have shown that mineral additives improve the mechanical strength of geopolymers. It has also been observed that autoclave curing has also resulted in an increase in the compressive strength values *(45.6 MPa).*

Narayanan and Shanmugasundaram [49] investigated thermal *(heat resistance and thermal conductivity)* and mechanical properties of fly ash-based geopolymer mortars. Fly ash *(class F),* river sand as raw materials, sodium hydroxide and sodium silicate as alkali activators were used. Different curing methods and curing conditions were used during the research. The effect of curing time (1 h–24 h) was also investigated.

- ambient curing,
- heating chamber, 1,200 W; T = 80 °C;
- hot air oven, 1,000 W; T = 80 °C;
- autoclave: p = 2.05 MPa; T = 80 °C;

According to the tests among all curing conditions, hot air oven curing shows the best result *(T = 80 °C; curing time: 6 hours).* In this case compressive strength of the geopolymer was increased by 36 percent and coefficient of thermal conductivity was decreased by 6.34 percent.

Yunsheng et al. [50] prepared slag based geopolymers using metakaolinite precursor. Their aims were the improvement of mechanical strength and to study the immobilization behaviour of heavy metals *(mainly Pb and and Cu).* Geopolymer mixtures were prepared with 4 different slag contents *(10%, 30%, 50%, 70% by weight)* and 3 different curing methods *(conventional curing, curing in steam, autoclave curing)* were also applied.

During the study of the effects of curing methods and curing time it was found that autoclave curing is the most effective method to increase the mechanical strength *(compressive and flexural strengths reach 70 MPa and 8.82 MPa, respectively)* of slag-based geopolymers.

CONCLUSIONS

As this review attempted to present, the development of conventional and artificial materials produced by foaming technology is continuous. Researchers try to develop more and more foamed materials, mainly with the use of secondary raw materials and other waste materials, with better properties and performance. Therefore, both raw materials and foaming technologies are required to develop.

ACKNOWLEDGEMENT

The described article was carried out as part of the Sustainable Raw Material Management Thematic Network – RING 2017, EFOP-3.6.2-16-2017-00010 project in the framework of the Széchenyi2020 Program. The realization of this project is supported by the European Union, co-financed by the European Social Fund.

REFERENCES

[1] https://minerals.usgs.gov/minerals/pubs/mcs/2018/mcs2018.pdf (Accessed April, 2018)

[2] UNIDO (2006). *Cement production in Vertical Shaft kilns in China – status and opportunities for improvement*. A report to the United Nations Industrial Development Organization.

[3] Forrai Jánosné. *A beton minősítések, minőség ellenőrzés; Monolit beton készítése I*. Nemzeti Szakképzési és Felnőttképzési Intézet, Available: http://kepzesevolucioja.hu/dmdocuments/4ap/9_0482_tartalomelem_010_munkaanyag_100331.pdf (Accessed May, 2018)

[4] *Cement-Beton Zsebkönyv*. A Duna-Dráva Cement Kft. kiadványa, 2007. Available: http://www.sasovits.hu/cnc/irodalom/4594fc87222fa-BETON-.pdf (Accessed March, 2018)

[5] J. H. Mohammed, A. J. Hamad (2014). A classification of lightweight concrete: materials, properties and application review. *International Journal of Advanced Engineering Applications*, Vol. 7, Iss.1, p. 5257.

[6] K. Jitchaiyaphum, T. Sinsiria, P. Chindaprasirt (2011). Cellular Lightweight Concrete Containing Pozzolan Materials. *Procedia Engineering*, Vol. 14, pp. 1157–1164.

[7] Y. H. M. Amran, N. Farzadnia, A. A. A. Ali (2015). Properties and applications of foamed concrete: a review. *Construction and Building Materials*, Vol. 101, pp. 990–1005.

[8] K. Ramamurthy, E. K. K. Nambiar, G. I. S. Ranjani (2009). A classification of studies on properties of foam concrete. *Cement and Concrete Composites*, Vol. 31, No. 6, pp. 388–396.

[9] N. Narayanan, K. Ramamurthy (2000). Structure and properties of aerated concrete: a review. *Cement & Concrete Composites*, Vol. 22, pp. 321–329.

[10] E. C. Pytlik, J. Saxena (1991). Fly ash based autoclaved cellular concrete: The building material of the 21st century. *Proceedings of the Ninth International Ash Use Symposium, ACAA, EPRI Report*, No. GS-7162, Palo Alto, CA, 1, 25-1-25-12. Jan 1991.

[11] D. K. Panesar (2013). Cellular concrete properties and the effect of synthetic and protein foaming agents. *Construction and Building Materials*, Vol. 44, pp. 575–584.

[12] K. De Weerdt (2011). *Geopolymers – State of the art*. COIN Project report 37.

[13] Mucsi G., Csőke B., Molnár Z. (2012). Alkáli aktivált pernyealapú kötőanyag vizsgálata. *Hulladék Online*, Vol. 3, No.1, pp. 1–11.

[14] Developments in strategic materials. *A Collection of Papers Presented at the 32nd lnternational Conference on Advanced Ceramics and Composites* January 27–February 7, 2008 Daytona Beach, Florida; Editors: H. Lin, K. Koumoto, W. M. Kriven, E. Garcia, I. E. Reimanis, D. P. Norton, Wiley 2009.

[15] R. A. Aguilar, O. Burciaga Díaz, J. I. Escalante García (2010). Lightweight concretes of activated metakaolin–fly ash binders, with blast furnace slag aggregates. *Construction and Building Materials*, Vol. 24, pp. 1166–1175.

[16] C. Bai, T. Ni, Q. Wang, H. Li, P. Colombo (2018). Porosity, mechanical and insulating properties of geopolymer foams using vegetable oil as the stabilizing agent. *Journal of the European Ceramic Society*, Vol. 38, pp. 799–805.

[17] Z. Zhang, J. L. Provis, A. Reid, H. Wang (2015). Mechanical, thermal insulation, thermal resistance and acoustic absorption properties of geopolymer foam concrete. *Cement & Concrete Composites*, Vol. 62, pp. 97–105.

[18] A. Font, M. V. Borrachero, L. Soriano, J. Monzó, Jordi Payá (2017). Geopolymer eco-cellular concrete (GECC) based on fluid catalytic cracking catalyst residue (FCC) with addition of recycled aluminium foil powder, *Journal of Cleaner Production*, Vol. 168. pp. 1120–1131.

[19] W. Zhu, X. H. Rao, Y. Liu, E.-H. Yang (2018). Lightweight aerated metakaolin-based geopolymer incorporating municipal solid waste incineration bottom ash as gas-forming agent. *Journal of Cleaner Production,* Vol. 177, pp. 775–781.

[20] G. Mucsi, A. Szenczi, Z. Molnár, J. Lakatos (2016). Structural formation and leaching behavior of mechanically activated lignite fly ash based geopolymer. *Journal of Environmental Engineering and Landscape Management,* Vol. 24, No. 1, pp. 48–59.

[21] S. Kumar, G. Mucsi, F. Kristály, P. Pekker (2017). Mechanical activation of fly ash and its influence on micro and nano-structural behaviour of resulting geopolymers. *Advanced Powder Technology,* Vol. 28. pp. 805–813.

[22] Z. Chen, Y. Liu, Zhu, E-H. Yang (2016). Incinerator bottom ash (IBA) aerated geopolymer. *Construction and Building Materials,* Vol. 112, pp. 1025–1031.

[23] P. Hlaváček, V. Šmilauer, F. Škvára, L. Kopecký, R. Šulz (2015). Inorganic foams made from alkali-activated fly ash: Mechanical, chemicaland physical properties. *Journal of the European Ceramic Society,* Vol. 35, pp. 703–709.

[24] M. Y. J. Liu, U. J. Alengaram, M. Z. Jumaat, K. H. Mo (2014). Evaluation of thermal conductivity, mechanical and transportproperties of lightweight aggregate foamed geopolymer concrete. *Energy and Buildings,* Vol. 72, pp. 238–245.

[25] V. Ducman, L. Korat (2016). Characterization of geopolymer fly-ash based foams obtained with the addition of Al powder or H_2O_2 as foaming agents. *Materials Characterization,* Vol. 113, pp. 207–213.

[26] N. Y. Mostafa (2005). Influence of air-cooled slag on physicochemical properties of autoclaved aerated concrete. *Cement and Concrete Research,* Vol. 35, pp. 1349–1357.

[27] K. Kunchariyakun, S. Asavapisit, K. Sombatsompop (2015). Properties of autoclaved aerated concrete incorporating rice husk ash as partial replacement for fine aggregate. *Cement and Concrete Composites,* Vol. 55, pp. 11–16.

[28] Jin H., Wu Y., Guan W. (2001). Research on Producing Gas Concrete With Burnt Waste Residue. *Coal Technology,* Vol. 20, pp. 45–46.

[29] M. S. Baspinar, I. Demir, E. Kahraman, G. Gorhan (2014). Utilization Potential of Fly Ash together with Silica Fume in Autoclaved Aerated Concrete Production. *KSCE Journal of Civil Engineering,* Vol. 18, No. 1, pp. 47–52.

[30] K. Ramamurthy, N. Narayanan (2000). Influence of composition and curing on drying shrinkage of aerated concrete. *Materials and Structures,* Vol. 33, pp. 243–250.

[31] J. Wan, S. Jia (2015). *Research on Preparation and Influencing Factors of High Calcium High Sulfate Ash to Autoclaved Aerated Concrete.* Proceedings of the 11th International Congress for Applied Mineralogy (ICAM), Springer, pp. 335–341.

[32] X. Huang, W. Ni, W. Cui, Z. Wang, L. Zhu (2012). Preparation of autoclaved aerated concrete using copper tailings and blast furnace slag. *Construction and Building Materials,* Vol. 27, pp. 1–5.

[33] W. Wongkeo, P. Thongsanitgarn, K. Pimraksa, A. Chaipanich (2012). Compressive strength, flexural strength and thermal conductivity of autoclaved concrete block made using bottom ash as cement replacement materials. *Materials and Design,* Vol. 35, pp. 434–439.

[34] J. Fan, D. Cao, Z. Jing, Y. Zhang, L. Pu, Y. Jing (2014). Synthesis and Microstructure Analysis of Autoclaved Aerated Concrete with Carbide Slag Addition. *Journal of Wuhan University of Technology-Mater. Sci. Ed.,* pp. 1005–1010, 2014. October.

[35] T. Sugama, L. E. Brothers (2004). Sodium-silicate-activated slag for acid-resistant geothermal well cements. *Advances in Cement Research*, Vol. 16, No. 2, pp. 77–87.

[36] A. M. Rashad, S. R. Zeedan, H. A. Hassan (2012). A preliminary study of autoclaved alkali-activated slag blended with quartz powder. *Construction and Building Materials,* Vol. 33, pp. 70–77.

[37] B. Israngkura Na Ayudhya (2016). Comparison of compressive and splitting tensile strength of autoclaved aerated concrete (AAC) containing water hyacinth and polypropylene fibre subjected to elevated temperatures. *Materials and Structures*, Vol. 49, pp. 1455–1468.

[38] K. Kunchariyakun, S. Asavapisit, K. Sombatsompop (2015). Properties of autoclaved aerated concrete incorporating rice husk ash as partial replacement for fine aggregate. *Cement & Concrete Composites,* Vol. 55, pp. 1–16.

[39] M. Li (2016). Influence of Polycarboxylic-type Admixture on the Strength of Autoclaved Aerated Concrete. *Journal of Wuhan University of Technology-Mater. Sci. Ed.,* Vol. 31, No. 6. pp. 1319–1322.

[40] Q. Wang, Y. Chen, F. Li, T. Sun, B. Xu (2006). Microstructure and Properties of Silty Siliceous Crushed Stone-lime Aerated Concrete. *Journal of Wuhan University of Technology-Mater. Sci. Ed.,* Vol. 21, No. 2, pp. 17–20.

[41] F. L. Kapustin, A. A. Vishnevskii, V. M. Ufimtsev (2017). Use of an ash-slag dump mixture in the production of autoclaved aerated concrete. *Power Technology and Engineering*, Vol. 51, No. 4, pp. 390–393.

[42] B. I. N. Ayudhya, Y. Ungkoon (2010). Bond Strength of Fiber Reinforced Polymer (FRP) Bars in Autoclaved Aerated Concrete (AAC). *CICE 2010 – The 5th International Conference on FRP Composites in Civil Engineering,* Beijing, China, September 27–29.

[43] A. A. Aliabdo, Abd-Elmoaty M. Abd-Elmoaty (2014). H. H. Hassan, Utilization of crushed clay brick in cellular concrete production. *Alexandria Engineering Journal*. Vol. 53, pp. 119–130.

[44] P. Walczak, J. Małolepszy, M. Reben, P. Szymański, K. Rzepa (2015). Utilization of waste glass in autoclaved aerated concrete. *Procedia Engineering,* Vol. 122, pp. 302–309.

[45] M. Albayrak, A. Yörökoglu, S. Karahan, S. Atlıhan, H. Yılmaz Aruntas, I. Girgin (2007). Influence of zeolite additive on properties of autoclaved aerated concrete. *Building and Environment,* Vol. 42, pp. 3161–3165.

[46] A. Keulen, P. I. J. Kakebeeke (2013). Geopolymer materials comprising alkaline activator and an additive selected from sugar and/or organic acids. Patent WO2015076675A1.

[47] H. C. Hao, Z. Qin (2014). Preparation method of geopolymer-based fiberboard with red mud as raw material. Patent CN103951332A.

[48] D. Bondar, C. J. Lynsdale, N. B. Milestone, N. Hassani, A. A. Ramezanianpour (2010). Geopolymer Cement from Alkali-Activated Natural Pozzolans: Effect of Addition of Minerals. *2nd International Conference on Sustainable Construction Materials and Technologies*.

[49] A. Narayanan, P. Shanmugasundaram (2017). An Experimental Investigation on Fly ash-based Geopolymer Mortar under different curing regime for Thermal Analysis. *Energy and Buildings* Vol. 138, pp. 539–545.

[50] Z. Yunsheng, S. Wei, C. Qianli, C. Lin (2007). Synthesis and heavy metal immobilization behaviors of slag based geopolymer. *Journal of Hazardous Materials,* Vol. 143, pp. 206–213.

Materials Science and Engineering, Volume 43, No. 1 (2018) pp. 54–61.

THE EFFECT OF INCLUSIONS ON THE TENSILE PROPERTIES OF AlSi7Mg0.4Cu0.5 CASTING ALLOY

GÁBOR GYARMATI[1]–MONIKA TOKÁR[2]–GYÖRGY FEGYVERNEKI[3]

In this study, the effects of different melt cleaning fluxes on the inclusion content and tensile properties of an aluminum casting alloy were compared. Melt treatments, consisting of rotary degassing with N_2 gas, and flux addition were executed using four different fluxes. The inclusion content of the melts was investigated with the evaluation of K-mold samples. In order to get information about the impact of the differences of melt quality on the mechanical properties of final products, cylindrical tensile specimens were machined from heat treated castings and tensile tests were carried out. The fracture surfaces of tensile specimens and K-mold samples were inspected with stereomicroscope and scanning electronmicroscope.

Keywords: aluminum casting alloys, inclusions, rotary degassing, flux treatment, tensile properties

INTRODUCTION

Inclusions are discontinuities of the material which are non-metallic or sometimes intermetallic phases embedded in a metallic matrix [1], [2]. Inclusions can occur in the form of solid particles, films or liquid droplets in the molten alloys [3]. The quantity and type of inclusions in the melt are determined by the quality of charge and alloying materials, as well as the melting and melt handling processes. The most common inclusions in aluminum alloys are non-metallic compounds: oxides, nitrides, carbides, and borides. Inclusions can be observed in the form of single particles, clusters and agglomerates [4].

Inclusions reduce mechanical properties by detracting from the effective cross-sectional area when stress is applied and because of the concentration of stresses at the inclusion interface. *Figure 1* shows an example of the property reduction effect of inclusions.

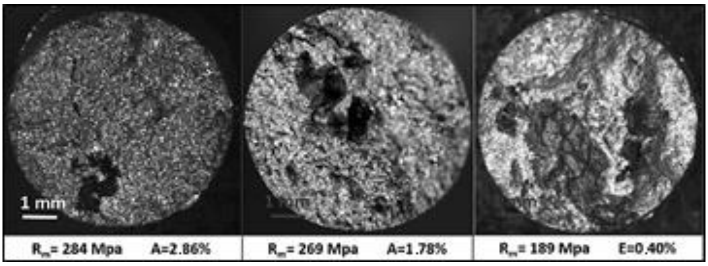

Figure 1

The fracture surface of tensile specimens with different inclusion contents [7]

---

[1] Foundry Institute, University of Miskolc
H-3515 Miskolc-Egyetemváros, Hungary
gygabor007@gmail.com

[2] Foundry Institute, University of Miskolc
H-3515 Miskolc-Egyetemváros, Hungary
monika.tokar@uni-miskolc.hu

[3] Foundry Institute, University of Miskolc
H-3515 Miskolc-Egyetemváros, Hungary
gyorgy.fegyverneki@nemak.com

The three tensile specimens shown have different inclusion contents on the fracture surface. It can also be observed that the larger the oxide films on the fracture surface are, the lower the tensile properties of the test bar become. Properties such as elongation, yield strength, and ultimate tensile strength decrease with the increased inclusion content in the metallic matrix. Inclusions in the melt can negatively influence melt fluidity and can prevent interdendritic feeding [5], [6].

Flux treatment usually includes the addition of a solid blend of inorganic compounds to the melt. These compounds may perform several functions, such as the removal of non-metallic impurities from the melt, the protection of the melt surface, or the refinement, and/or degassing of the molten alloy [8]. The effect of fluxes is determined by their chemical composition, morphology, added quantity, as well as the temperature of the melt, and the method of flux addition [9]. Modern melt treatment stations can automatically add flux blends to the melt during the first stages of rotary degassing. During the first part of the treatment, the rotor is lowered to the melt and a vortex is created around the shaft by the rotor, which is rotating at a higher speed during this stage of the cycle. At this part of the treatment, the baffle plate remains in the upper position. Then, the hopper feed system adds the required amount of flux to the vortex. The flux is taken to the bottom of the melt by the vortex and effectively mixed throughout the melt by the rotor. After flux addition, the baffle plate is lowered into the melt, and the rotor speed is decreased in order to terminate the vortex. Finally, a controlled degassing and floatation treatment takes place [10–12].

1. EXPERIMENTAL

1.1. Melt preparation

Melt treatment, consisting of rotary degassing with N_2 gas and flux addition, was executed on an AlSi7Mg0.4Cu0.5 alloy melt using four different fluxes (A, B, C, and D). Each flux was used in 8 treatment cycles. The quantity of metal treated in one cycle was approximately 1 ton. The metal was melted in a stack smelter then transported by a transport ladle to a resistance heated holding furnace where the melt treatments were performed *(Figure 2)*. In each case, the melt was poured over a lesser quantity of melt (ca. 200 kg) which remained in the holding furnace from the previous cycle. The treatment parameters and the quantity of flux added (400 g) were the same in each cycle. The N_2 gas flow rate was 20 L/min; the rotor revolution was 500 RPM during vortex formation and 250 RPM in the degassing phase. The treatment time was 10 minutes in each case. The molten metal temperature in the holding furnace was maintained between 740 ^{o}C and 750 ^{o}C.

Figure 2
The stages of melt preparation: a) pouring from melting furnace, b) melt transport to holding furnace, and c) melt processing

1.2. Inclusion analysis

The inclusion content of the melts treated with different fluxes was investigated by the evaluation of K-mold samples, which were prepared in the gravity die illustrated in *Figure 3*. The sample itself is a flat plate with four notches that act as fracture points. The fracture surface of the samples can be examined either by visual inspection or with microscope. Based on the number of inclusions, a K-value can be determined which can be used for the quantitative characterization of the melt purity:

$$\mathrm{K} = \frac{\mathrm{S}}{\mathrm{n}} \tag{1}$$

where **K** is the K-value, **n** is the number of examined samples, and **S** is the total number of inclusions found in **n** pieces [6].

Figure 3
K-mold apparatus

During each melt preparation, K-mold samples were cast from the melt in the transport ladle, and from the melt in the holding furnace before and after the melt treatments. Five samples were cast at each stage. The fracture surfaces of K-mold samples were inspected with a stereomicroscope at a magnification of 25×. The inclusions found on the fracture surfaces were examined with SEM combined with EDS analysis.

The effect of different fluxes on the melt purity was evaluated using the comparison of K-values determined before and after the melt treatments. The percentage of change in K-values **(ΔK)** was calculated using the following equation:

$$\Delta K = \frac{K_2 - K_1}{K_1} \cdot 100 \quad [\%] \tag{2}$$

where $\mathbf{K_1}$ is the K-value determined before the melt treatment and $\mathbf{K_2}$ is the K-value determined after the melt treatment.

1.3. Tensile testing

In order to study the effect of melt treatments on the tensile properties of castings, tensile tests were executed on cylindrical specimens (with a diameter of 5 mm) machined from T5 heat treated castings with a Zwick Z010 testing machine. Altogether, 12 castings were investigated (3 casting/flux blend), the number of specimens machined from a casting was 3. The castings were made with Rotacast® technology. The inclusions found on the fracture surface of specimens were examined with stereomicroscope. The area fraction of the inclusions on the fracture surfaces was calculated by MATLAB® Image Processing Toolbox$^{\mathrm{TM}}$.

2. RESULTS AND DISCUSSION

The average K-values of the melts at the different stages of melt preparation can be observed in *Figure 4*. It can be seen that melts had different inclusion contents even in the transport ladle which was the result of the differences in the quality of charge materials. In each case, the melt in the transport ladle was poured onto a small quantity of melt remaining in the holding furnace from the previous cycle. Thus, the inclusion content of the melt was influenced by the quality of the residual melt. This way, the applied flux blends had an indirect effect on the average K-values of the melts even before the treatments were executed.

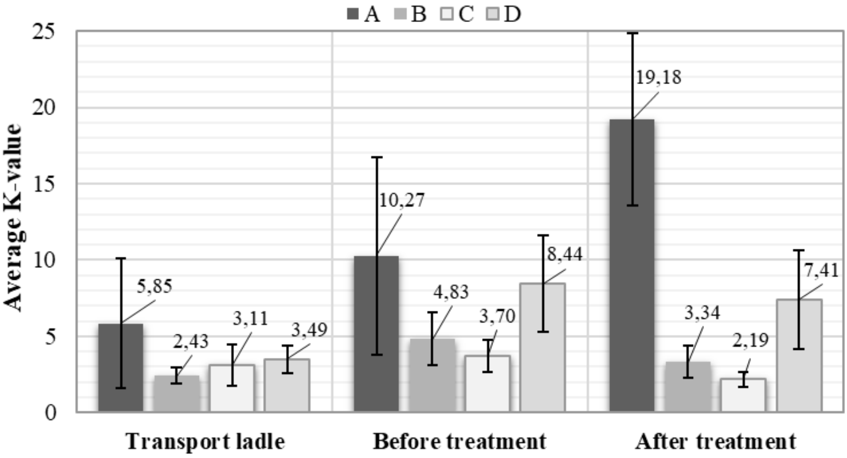

Figure 4
Average K-values at different stages of melt preparation

The average ΔK values for each flux blends are illustrated in *Figure 5*. The treatments executed with flux *C* were the most effective in reducing the K-values and flux *B* was the second most efficient. Flux blend *A* had the poorest results. The melt treatments performed with flux *A* resulted in the increased inclusion content of the melt, which caused a positive change in the average K-value.

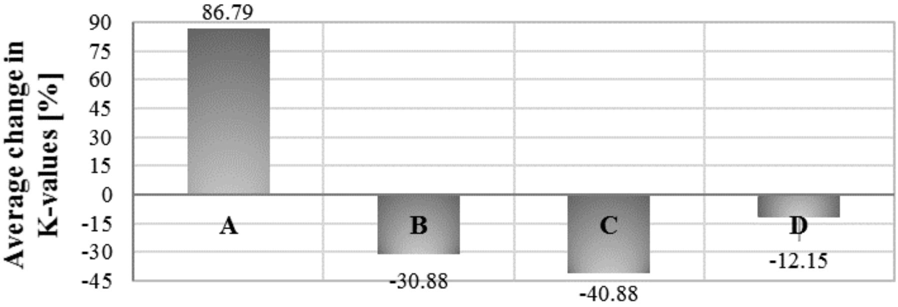

Figure 5
Average change in K-values (ΔK)

Some examples of inclusions found during the examination of K-mold samples can be seen in *Figure 6*. In most cases, creased film-like inclusions were found on the fracture surfaces.

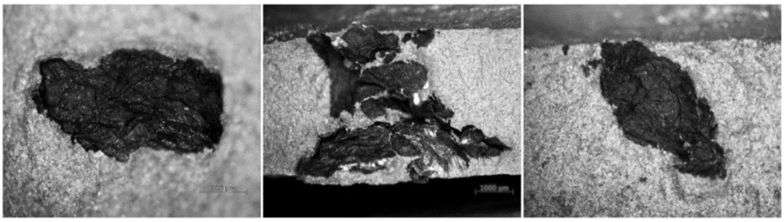

Figure 6
Inclusions found on fracture surfaces of K-mold samples

The inclusions found on the fracture surfaces of K-mold samples were investigated with SEM. The composition of inclusions was determined by EDS microanalysis. *Figure 7* shows some examples of the SEM images of the inclusions. Based on the EDS analysis, the inclusions found are nonmetallic compounds like Al_2O_3, AlN, $MgO{\cdot}Al_2O_3$ and various strontium-oxides.

Figure 8 summarizes the results of the tensile tests. There is no significant difference between the ultimate tensile strength (UTS) and the yield strength (YS) results. Some differences can be observed between the elongation results, but there is no clear relationship between the determined K-values and the elongation values. It can be concluded that the effect of melt treatments with different fluxes on the tensile properties of castings cannot be determined from the tensile test results. The reason might be that the tensile test results of species machined from heat treated castings depend not only on the inclusion content of the melt but several other technological parameters as well, like casting technology and the parameters of the heat treating process.

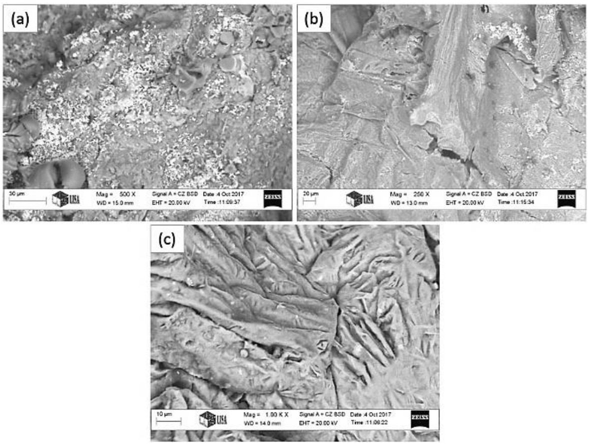

Figure 7
SEM images of inclusions: a) Al_2O_3 inclusion with numerous different strontium-oxide particles (white phases), b) $MgO{\cdot}Al_2O_3$ film with some strontium-oxide particles, c) creased Al_2O_3 film

It can be seen in *Figure 8* that there is a significant scatter in the elongation at the fracture values of the samples, regardless of the type of flux blend used during the melt treatments. In order to explore the reason for the high standard deviation in elongation values, the fracture surfaces of tensile test specimens were examined with a stereomicroscope. It was found that all tensile specimens with lower elongation value had inclusions on the fracture surfaces.

In order to investigate the relationship between the size of inclusions and the extent of reduction in the elongation values, the area of inclusions was measured by quantitative image analysis. The area fraction of inclusions was determined by the following equation:

$$A_f = \frac{A_i}{A_{fs}} \cdot 100 \ \ [\%] \tag{3}$$

where $\mathbf{A_f}$ is the area fraction of inclusions, $\mathbf{A_i}$ is the total area of inclusions, and $\mathbf{A_{fs}}$ is the area of the fracture surface.

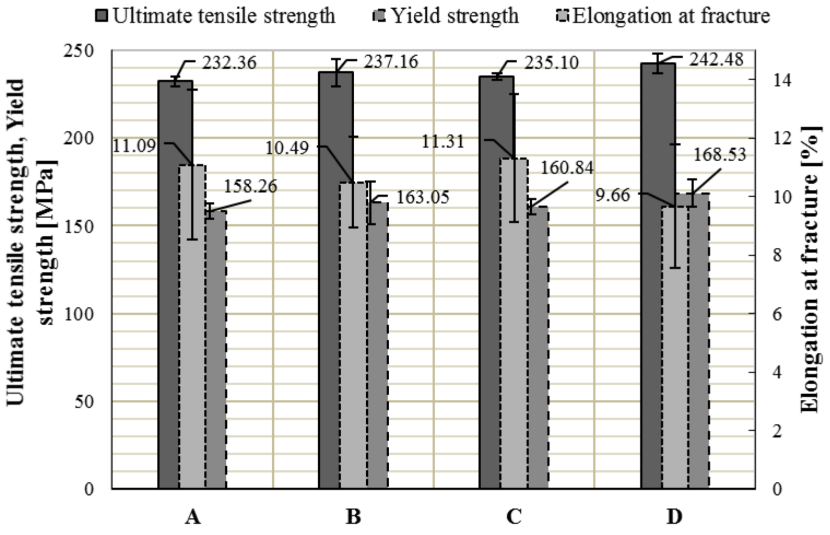

Figure 8

Tensile test results of specimens machined from castings

Figure 9 shows the steps of the applied binary image making process.

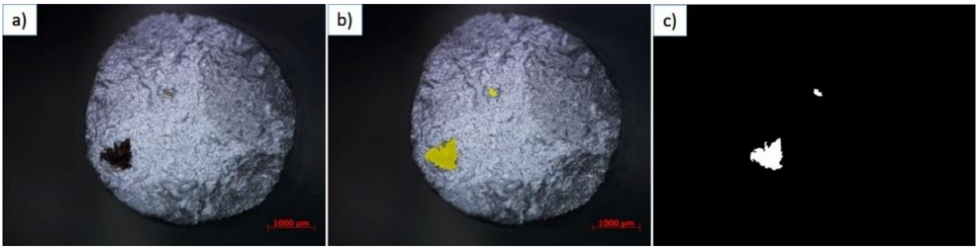

Figure 9

Production of binary image: a) original, b) segmented, and c) binary image

The total number of specimens with inclusion on the fracture surface was 9. The average elongation of samples with no inclusions was 11.74 ± 0.78%. The results of the image analysis of specimens with inclusions are given in *Table 1*. Based on the results, an inclusion contributing to 1% of the fracture area can cause the reduction of the elongation value by 55% compared to the average elongation of samples with no inclusions. *Figure 10* summarizes the results of tensile testing and image analysis. It can be seen, that the results of the specimens can be divided into three groups: specimens with $A_f > 1\%$, $A_f < 1\%$, and samples with no detected inclusions ($A_f = 0\%$). Where $A_f > 1\%$, the elongation values are significantly lower compared to the cases when inclusions are not present. The inclusions found on samples with $A_f < 1\%$ are much smaller and the elongation values of these specimens are better.

Table 1

Area fraction of inclusions (A_f) and elongation values of specimens

Elongation [%]	5.236	5.894	8.537	5.603	5.234	8.670	9.310	9.230	8.426
A_f [%]	2.262	1.121	1.913	2.021	1.043	0.224	0.544	0.193	0.180

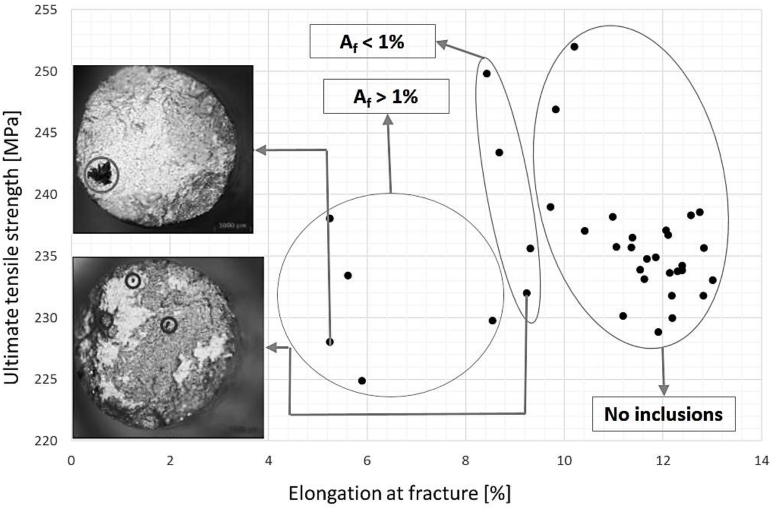

Figure 10

Comparison of the area fraction of inclusions (A_f) and tensile test results

CONCLUSION

In this study, the effects of different melt cleaning fluxes on the inclusion content and tensile properties of an AlSi7Mg0.4Cu0.5 casting alloy were compared.

There was a significant difference between the melt cleaning efficiency of the applied fluxes. The effect of melt treatments on the tensile properties of castings could not be determined from the tensile test results because there were no significant differences between the results of samples made from melts treated with different fluxes. It was found that all tensile specimens with lower elongation value had inclusions on their fracture surfaces. Based on the image analysis results, the size of inclusions is an important factor because an inclusion contributing to 1% of the fracture area can cause the reduction of an elongation value by 55%, as compared to the average elongation of samples with no inclusions.

The results clearly indicate that the presence of inclusions (especially oxide-films) can lead to a significant scatter in the elongation values of the cast alloy due to early initiation of fracture. The removal of inclusions is essential in order to achieve more consistent mechanical properties and to prevent unpredicted failure of cast components.

ACKNOWLEDGMENT

The main author is thankful for the rest of the authors' help, patience and advice to make the realization of this article possible.
The authors are grateful to Árpád Kovács from the Institute of Physical Metallurgy, Metal Forming and Nanotechnology at the University of Miskolc for carrying out the tests with scanning electron microscope.
Supported by the ÚNKP-18-2 New National Excellence Program of the Ministry of Human Capacities.

REFERENCES

[1] P. K. Trojan (2008). Inclusion-Forming Reactions. In *ASM Handbook Vol. 15.: Casting*. ASM International, pp. 74–83.

[2] Vörös Á. (1978). *Öntészet – Műszaki értelmező szótár 45–46*. Budapest: Akadémiai Kiadó, p. 301.

[3] J. Morscheiser, P. Le Brun, M. Gökelma, M Badowski, T. Dang, S. Tewes (2015). Observation on Inclusion Settling by LiMCA and PoDFA Analysis in Aluminium Melts. *International Aluminium Journal*, Vol. 91, No. 4, pp. 56–61.

[4] R. Gallo (2017). I have Inclusions! Determining the Best Cost Saving Approach. *Modern Casting*, Vol. 107, No. 8, pp. 31–35.

[5] J. G. Kaufman, E. L. Rooy (2004). The Influence and Control of Porosity and Inclusions in Aluminum Castings. In *Aluminum Alloy Castings: Properties, Processes, and Applications*. J. G. Kaufman, E. L. Rooy (eds.), ASM International, pp. 47–54.

[6] S. W. Hudson, D. Apelian (2016). Inclusion Detection in Molten Aluminum: Current Art and New Avenues for in Situ Analysis. *International Journal of Metalcasting*, Vol. 10, No. 3, pp. 315–321.

[7] Q. Chen, W. D. Griffiths (2017). The Effect of Sr Modifier Additions on Double Oxide Film Defects in 2L99 Alloy Castings. *Metallurgical and Materials Transactions A*, Vol. 48, pp. 5688–5698.

[8] T. A, Utigard, K. Friesen, R. R. Roy, J. Lim, A. Silny, C. Dupuis (1998). The Properties and Uses of Fluxes in Molten Aluminum Processing. *JOM*, Vol. 50, No. 11, pp. 38–43.

[9] R. Gallo, D. Neff (2008). Aluminum Fluxes and Fluxing Practice. In *ASM Handbook Vol. 15.: Casting*. ASM International, pp. 230–239.

[10] A. Pascual (2009). Emerging Melt Quality Control Solution Technologies for Aluminium Melt. *China Foundry*, Vol. 6, No. 4, pp. 358–365.

[11] P. Careil, R. Simon (2008). MTS 1500 – Automatisierte Schmelzebehandlung Mit Chemischen Produkten. *Giesserei Rundschau*, Vol. 55, Issue 3/4, pp. 46–50.

[12] R. Kendrick, G. Muneratti, S. Consoli, F. Voltazza, S. Barison (2012). The Use of Metal Treatment to Control the Quality of an Aluminium Casting Produced by the High-Pressure Diecasting Process. *Metallurgical Science and Technology*, Vol. 30, No. 2, pp. 3–11.

Materials Science and Engineering, Volume 43, No. 1 (2018) pp. 62–70.

NUMERICAL INVESTIGATION OF CLINCHED JOINTS

SZABOLCS JÓNÁS[1]–MIKLÓS TISZA[2]

This paper studies the clinch joints. After the material testing and model validations the different influencers were examined. The different types of hardening laws have a high effect on the undercut of the joints, so should always be considered which is the appropriate for the task. The frictional condition during forming processes is interesting topic and has a high impact on the results. The knowledge of the effect of the geometrical variations is useful for designers, therefore it was studied.

Keywords: clinch joint, simulation, FEA, DP600 steel

INTRODUCTION

Clinch joints are used mostly in automotive, computer and aircraft industries, but for instance according to the standards not allowed to use in food industry [3], [4], [5]. The clinch joints are quite new types of joints; the first patent has been accepted in 1989. This joint can be done between 2-3 thin sheets. The cross section of a joint can be seen in *Figure 1*. This figure shows the main geometrical parameters of a joint (2 sheets were joined). The undercut size (C value) and the size of the neck thickness (t_N value) are highly affecting the strength of the joints. In optimal case both of them are as high as possible.

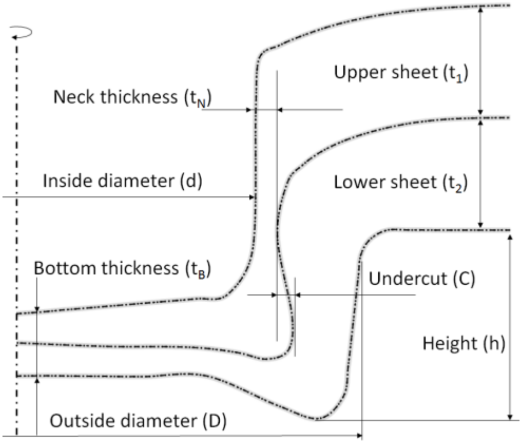

Figure 1
Cross section of a clinched joint and the main geometrical sizes

---

[1] Institute of Materials Science and Technology, Department of Mechanical Technology, University of Miskolc
H-3515 Miskolc-Egyetemváros, Hungary
szabolcs.jonas@gmail.com

[2] Institute of Materials Science and Technology, Department of Mechanical Technology, University of Miskolc
H-3515 Miskolc-Egyetemváros, Hungary
miklos.tisza@uni-miskolc.hu

The material of the sheets can be ferrous or non-ferrous at the same time, so there is a possibility to realize dissimilar joints without any added material (weld material or glue). The joint made by metal plastic forming by a special tool. After the patent the increasing industrial needs of clinching led the researchers to analyse the joint much more deeply. Several studies carried out the geometry optimization of the clinching tool to get better joints by different optimization methods [7], [8]. Other studies were carried out on the so-called hybrid joints. This variant has an adhesive layer between the sheets. The hybrid joints have higher strength but need much more time because of the adhesive layer's drying is a time-consuming process [1], [2].

In this study some influencers of the clinch joint were studied through a 2D axisymmetrical FE model with an advanced high strength steel type (DP600).

1. IDENTIFICATION OF THE MATERIAL

For the simulations the used material type is the DP600 type of steel. The DP600 is an advanced high strength steel, which is a multiphase (ferrite and martensite) steel with excellent combination of strength and formability. The dual phase steels (DP) consist of a soft ferrite matrix with disperse, hard second phase in a form of islands. It has got high strength, high work hardening rates and high strain energy absorption properties.

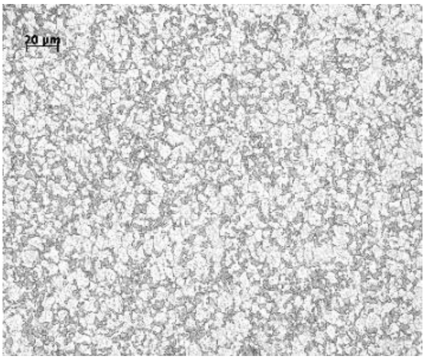

Figure 2

Microstructure of the DP600 (light: ferrite, grey: martensite)

Figure 2 shows the microstructure of the used steel. 100-200-600-1,200 µm series of grind paper, 3 µm polish pasta and 3% Nital was used for the specimen preparation. The measurements were done with a Carl Zeiss microscope with an image recognition software module. According to the measurements, this steel contains ~23% of martensite, and the average grain size is 5 µm. For the chemical composition a 60 µm grind paper was used. The measurements were performed with Oxford Instruments Foundry Master Pro spectroscopy machine. The chemical composition can be seen in *Table 1.*

Table 1

Chemical composition

	Fe	**C**	**Si**	**Mn**	**P**	**S**	**Cr**	**Mo**
wt% [%]	98.6	0.16	0.171	0.876	<0.005	<0.005	0.262	0.077
	Al	Co	Cu	Nb	Ti	V	W	Pb
wt% [%]	0.0553	0.0125	0.074	0.0214	<0.005	00124	0.0103	0.0114

To determine the mechanical properties tensile tests were performed with an MTS electro-hydraulic testing machine. The results can be seen in *Table 2*. The values show quite high difference between the orientations.

Table 2
Mechanical properties

			Mean value	**0°**	**45°**	**90°**
Ultimate tensile strength	R_m	N/mm^2	680	669	679	691
Yield strength	$R_{p0.2}$	N/mm^2	451	448	451	454
Fracture elongation	A_{80}	%	19	19	20	18
Hardening exponent	n	–	0.14	0.14	0.14	0.14
Anisotropy	r	–	0.81	0.71	0.73	0.98

2. CLINCHING PROCESS

The TOX produced clinching tool was set up in an MTS servo-hydraulic testing machine. The maximum load which the tool can survive is 50 kN. The set up can be seen in *Figure 3*.

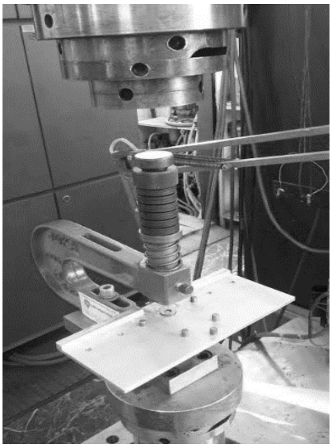

Figure 3
Clinching test set up

During the forming process the force-displacement curves were recorded in each case.

3. FE MODEL BUILDING

The FE simulation model was built in ANSYS WB 18.2 [11]. The geometry of the model was built up in ANSYS Design Modeler as a parametric model. A 2D axisymmetric model is presented below *(Figure 4)*. The tools were taken into consideration as linear-elastic materials, the two sheets were simulated with elastic-plastic behaviour with multilinear isotropic hardening rule. The two sheets were 1-1 mm thick. The tool has a spring row which was taken into consideration as an elastic body with 57 GPa of Young’s modulus. The mesh was built up by 2^{nd} order axisymmetrical quadrilateral and triangular elements (PLANE183). Both of the sheets contain 10 elements in thickness which provides adequate results. For better solution the edges in the contact zones were finer. The contact definition between the parts is Augmented Lagrange formulation with a frictional coefficient of $\mu = 0.12$ between the parts. Between the punching tool and the simplified spring row the contact definition was bonded with MPC algorithm. There are 3 time steps in the simulation. The simulation is performed as a displacement controlled model. According to the final, measured bottom thickness and the measured piston displacement, the vertical movement of the clinching tool was 3.25 mm. The holder was constrained in vertical direction by a compression only support and in the 1^{st} step a force (F = 1000 N) was applied which is constant in the 2^{nd} and 3^{rd} steps. In the 3^{rd} step the tool was removed from the joint.

The distribution of the equivalent plastic strain was checked with the unaveraged display option. The unaveraged distribution of the plastic strain can be seen in *Figure 5*. The high (greater than 2 mm/mm) plastic strains are acceptable, according to the literature [10].

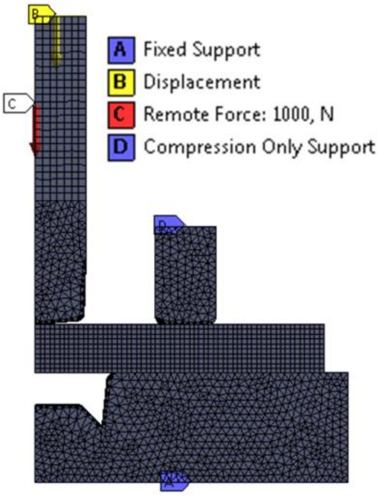

Figure 4
FE mesh and boundary conditions of the model

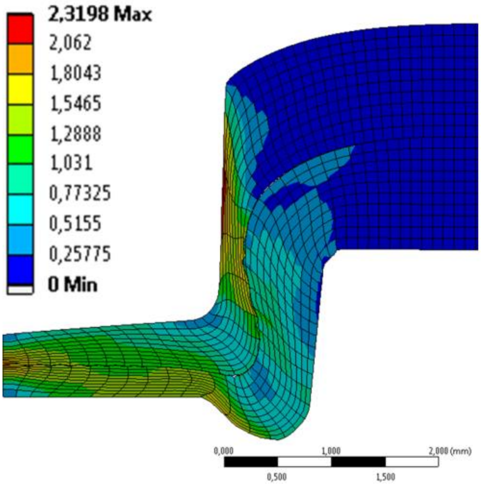

Figure 5
Equivalent plastic strain distribution after forming process (unaveraged)

4. MODEL VALIDATION

In this study the formed geometry and the forming force – relative punch displacement (F-d) curves were used to validate the FE results. The geometry comparison can be seen in *Figure 6*. The forming force – displacement results of the FE model can be compared after the correction of the measured values *(Figure 7)*. The difference between the model and the measurement is acceptable. The simulated curve shows a very good agreement with the measured one.

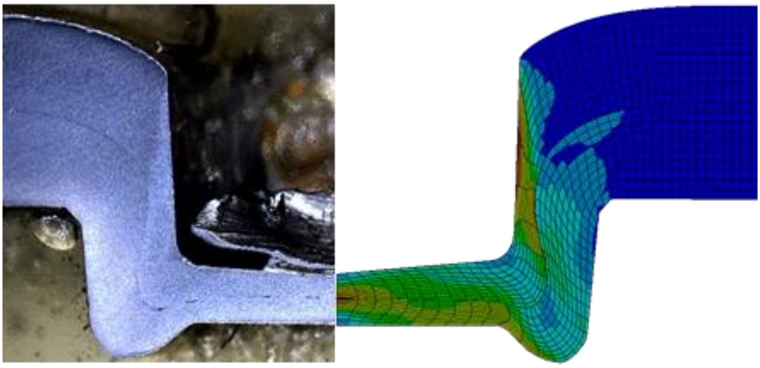

Figure 6

Cross section of the clinched and the simulated sheets (FE: eq. plastic strain)

According to [3] the measured curve can be divided into 3 main phases and 5 steps. In Phase I. the testing machine starts to work, the punching tool moves down, the holder moves downward to fix the sheets, the tool comes into contact with the upper sheet (punch side) and the joining process is started (Step I.). The tool punches the sheets and they move together (Step I. – Step II.) and this part of the process continues until the first bending point (Step II.). The lower sheet (die side) reaches the die; that is why the slope of the curve changes after Phase I. In Phase II. the sheets start to flow around the punching tool and start to flow inside the free space of the die (Step III.). The last part of the process needs more deformation force; the curve raises with the highest slope. In Step IV. the punching tool reaches the end position. In this phase the setting force reaches the maximum also. After this point the tool starts to remove from the joint with a certain slope depeding on the stiffness of the machine. After Step V. the joint is totally released.

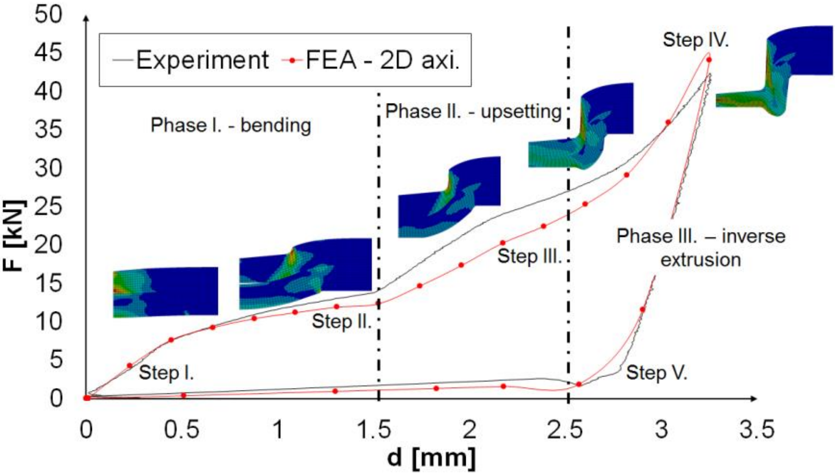

Figure 7

Comparison of the forming force-relative punching tool displacements

5. INFLUENCE OF MATERIAL PARAMETERS

Severe plastic deformation occurs during the forming process (Step III. according to *Figure 7*). As already stated, true plastic strains of the order of 2-3 are not unusual and stress-strain data far beyond the maximum uniform strain have to be available for the analysis [10]. For better simulation results the use of extrapolation methods is necessary. In this section the influence of the different hardening laws are presented through the comparison of the undercuts. The parameter identification was done by the least-squares method. The k_f is the true stress in MPa, φ is the true plastic strain, K is the strength coefficient in MPa, n is the strain hardening exponent and m is a material coefficient. The used hardening laws follow the equations (1–4):

$$k_f^{Nádai} = K \cdot \varphi^n \tag{1}$$

$$k_f^{Swift} = K \cdot (m + \varphi)^n \tag{2}$$

$$k_f^{Voce} = K \cdot (1 - m \cdot e^{-n\varphi}) \tag{3}$$

$$k_f^{Swift-Voce} = \alpha \cdot k_f^{Swift} + (1 - \alpha) \cdot k_f^{Voce} \tag{4}$$

Constants of the equations can be seen in the following table *(Table 3)*:

Table 3
Parameters of the models

	K [MPa]	m[-]	n [-]
Nádai	1,013.1	–	0.1329
Swift	1,063.9	0.0023	0.1533
Voce	772.13	26.17	0.4149

In case of the mixed or combined model (Swift-Voce) the α = 0.7495, which is a weighting factor of the two laws. *Figure 8* shows the curves fitted to the measured one.

Figure 10 shows the undercuts with the different methods. The Nádai and the mixed equations resulted nearly in the same sized undercut as it can be presumed according to the extrapolated curves *(Figure 9)*. The difference is quite large (~14%) between the Voce and the Swift strain-hardening models in the undercut region.

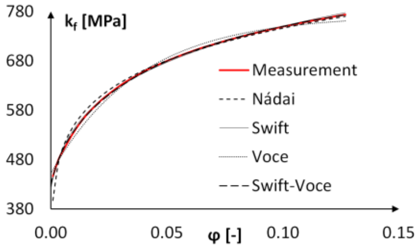

Figure 8
Parameter identification

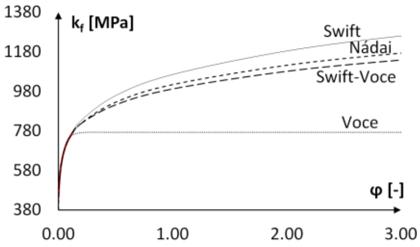

Figure 9
Extrapolated flow curves

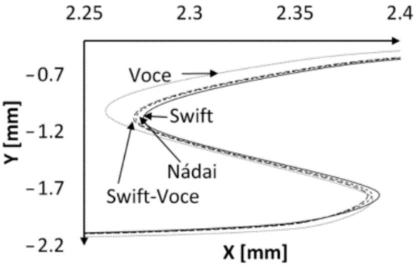

Figure 10
Influence of the hardening laws to the undercut

6. INFLUENCE OF THE TOOL GEOMETRY AND FRICTIONAL CONDITIONS

For a better understanding of the clinch joints a sensitivity analysis has been performed. The basis of the comparison is the size of the undercut (C) depending on the punching tool's geometry. In this case the tip angle and tip radius of the tool were taken into consideration. The *Table 4* contains the analysed geometry variations and the calculated undercut sizes.

Table 4
Analysed sizes

tip angle [°]	tip radius [mm]	C [mm]
1	0.2	0.213
1	0.3	0.175
1	0.4	0.141
2	0.2	0.162
2	0.3	0.117
2	0.4	0.110
3	0.2	0.154
3	0.3	0.112
3	0.4	0.101

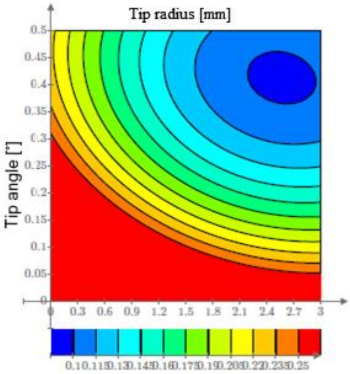

Figure 11
Influence of the punching tool's geometry on the undercut (fitted surface)

The fitted surface *(Figure 11)* shows the calculated data. It can be seen how the given parameter affect the undercut if there are only two variables. For tool designers *Figure 11* can be a helpful tool. This map can use for optimization procedures because its function can be easily calculated.

The frictional behaviour of a forming process is always a problematic question. In this subsection the effect of the frictional conditions between the sheets and tools were analysed through a few cases. The basic case is the μ = 0.12. For comparison a higher one and a lower one of frictional coefficients were taken into consideration as a global and constant variable. It means that all of the contacts have the same frictional coefficient during the given simulation. The figures *(Figure 12)* show the different force need and different undercut formation after forming. As it can be seen the higher (μ = 0.2) frictional coefficient has ~10 kN higher forming force need compared to the lower (μ = 0.05) case and the shape and the size of the undercuts are also different. The too high forming forces can easily lead to the failure of the tools; the use of monitoring systems is highly recommended.

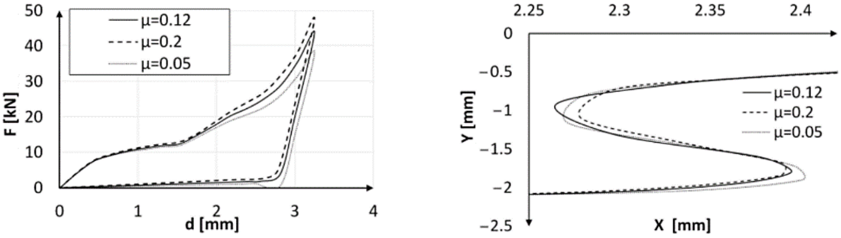

Figure 12

Influence of frictional coefficients (F-d curves and undercuts)

CONCLUSION

In this study the different influencers of DP600 clinch joints were analysed with a 2D axissymmetrical FE model. The appropriate hardening law is a key to have an accurate enough result. Next step in this research is the consideration of changing frictional behaviour of sliding surfaces in the FE simulation during the clinching process.

REFERENCES

[1] T. Sadowski, T. Balawender and P. Golewski (2015). *Technological aspects of manufacturing and numerical modelling of clinch-adhesive joints.* Springer, 2015

[2] L. Kascák and E. Spisák(2012). Clinching as a non-standard method for joining materials of dissimilar properties. *Zeszyty naukowe politechniki rzeszowskiej*, Nr. 284. Mechanika z. 84, pp. 31–41.

[3] Y. Tan, O. Han and F. Du (2005). Process Monitoring Method with Window Technique for Clinch Jointing. *ISIJ International*, Vol. 45, No. 5. pp. 723–729.

[4] M. Tisza, G. Gaszton, A. Kiss, P. Z. Kovács and Zs. Lukács (2014). Alakítható nagyszilárdságú lemezanyagok klincs kötése. *Multidiszciplináris tudományok*, Vol 4. pp. 49–58.

[5] Kovács P. Z. and Tisza M. (2016). Klincs kötés technológiai paramétereinek vizsgálata, végeselemes modellezéssel. *Anyagmérnöki Tudományok*, Vol. 39, No. 1, pp. 7–18.

[6] Béres G., Danyi J. and Végvári F. (2015). Clinching of steel sheets used in automotive industry. *Modern Technologies in Manufacturing*, Vol. 808, pp. 75–79.

[7] Eshtayeh, M. M., Hrairi, M. Mohiuddin, A. K. M. (2016). Clinching process for joining dissimilar materials: state of the art. *Int J Adv Manuf Technol*, Vol. 82, p. 179.

[8] F. Lambiase and A. Di Ilio (2014). An experimental study on clinched joints relized with different dies. *Thin-Walled Structures*, Vol. 85, pp. 71–80.

[9] S. Coppieters, S. Cooreman, H. Sol and D. Debruyne (2011). Reproducing the experimental strength of clinched connections with finite element methods. *International Journal of Material Forming*, Vol. 4, No. 4, p. 429.

[10] S. Coppieters (2012). Experimental and numerical study of clinched connections. Ph.D dissertation, KU Leuven.

[11] ANSYS 18.2 User's manual.

Materials Science and Engineering, Volume 43, No. 1 (2018) pp. 71–78.

REDUCING OF DNT CONTENT IN RED WATER FORMED DURING TDI PRODUCTION

ÁKOS KORBÁCS[1, 2]–R. ZSANETT BOROS[1, 3]–ANGELICA RODRIGUEZ[4]–
LÁSZLÓ FARKAS[1]

A well-known reagent was tested for industrial cleaning and extracting of dinitrotoluene (DNT) (80/20) from red water which is a waste water of the toluene-diisocyanate (TDI) production. The capability of different extraction agents, such as 1-methyl-2-nitro benzene and 1-methyl-4-nitro benzene mixture MNT (60/40) and methylbenzene (toluene) was studied. The toluene seemed to have a great efficiency, and only a low amount was needed for the extraction process and less DNT (60/40) remained in the water after the extraction. The red water contains infinitesimal toluene after the extraction which can be distilled easily with small quantity of introduced heat at the distillation column, because of the toluene-water azeotrope behavior. Nevertheless, heat integration is also a possibility at the distillation step.

Keywords: DNT, MNT, toluene, extraction, distillation, CAD simulation

INTRODUCTION

Polyurethanes (PUR) are widely used nowadays. There are five main areas of the PUR market: (1) the furniture and mattress sector, which uses almost exclusively flexible foams, (2) the automotive industry which provides a market for flexible foams, filling foams, rigid and flexible integral skin foams as well as elastomers for engineering components, (3) the consumer sector, which is diversified in a manner similar to the automotive industry, (4) the building industry, which is by far the largest consumer of rigid foams as insulation materials, and (5) refrigeration engineering, which represents the second largest area for use of rigid polyurethane foams as insulation materials [1].

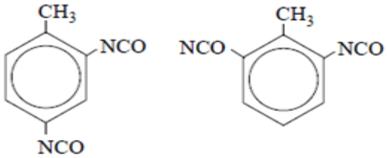

Figure 1
2,4-TDI (on the left) and 2,6 TDI are the two components of commercial TDI (80/20) where 80:20 is the mass ratio of the two isomers

---

[1] Wanhua-BorsodChem Ltd., Bolyai tér 1.
H-3700 Kazincbarcika, Hungary
akos.korbacs@borsodchem.eu

[2] Department of Chemical and Environmental Process Engineering, Faculty of Chemical Technology and Biotechnology, Budapest University of Technology and Economics
H-1111 Budapest, Hungary

[3] Institute of Chemistry, Faculty of Materials Science and Engineering, University of Miskolc
H-3515 Miskolc-Egyetemváros, Hungary

[4] Kalamazoo College, Kalamazoo,
US MI 49006, United States of America

Toluene diisocyanate (TDI) *(Figure 1)* is one of the most important raw material of polyurethane industry. The main isomers of TDI are the 2,4 and 2,6; IUPAC: [2,4-diisocyanato-1-methylbenzene, (80 m/m%)] and [2,6-diisocyanato-1-methyl-benzene, (20 m/m%)]. It is formed by the phosgenation of the appropriate amine (toluene-diamine, TDA). In the first step of TDA synthesis toluene reacts with acid (HNO_3/H_2SO_4) resulting in the formation of mono-nitrobenzene (MNT) mixture (1-methyl-2-nitro benzene and 1-methyl-4-nitro benzene, MNT [60/40]). The sulphuric acid-nitric acid mixture, which is responsible for nitration is used at the second nitration step first, where nitration of MNT to DNT occurred, and after that, this acid mixture circulates to the first nitration step, where nitration of toluene to MNT (this first nitration needs milder, less acidic condition) happen [2]. After a catalytic hydrogenation of MNT an isomer mixture of dinitro toluene is produced (1-methyl-2,4-dinitro benzene-ones and 1-methyl-2,6-dinitro benzene-ones, DNT [80/20]) *(Figure 2)* [3].

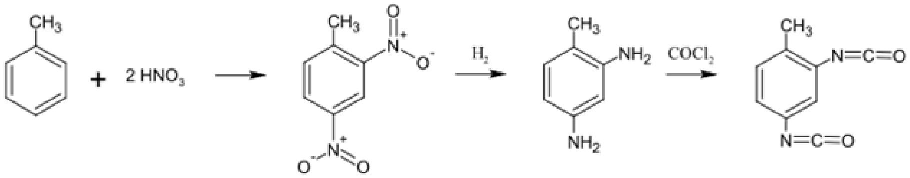

Figure 2
2,4-TDI transformation from toluene, industrial method

In terms of economy, a two-step nitration of toluene to DNT in mixed acid is still the most favorable procedure for manufacturing DNT. During this process methyl-(di)nitrophenols and its derivatives, so called (di)nitrocresols are formed which can be found in the DNT product [4]. It is important to get pure DNT, so this contaminated product is washed with water that contains NH_3 which makes these (di)nitro-cresols water soluble. Due to the colour of this water it is known as red water.

Search for solutions

This red water also contains DNT (1,100–1,500 mg/l) which is responsible for its characteristic colour. It is relatively easy to extract this chemical out of water with organic solvents, due to DNT's low water solubility, which increases with temperature *(Table 1)*.

Table 1
Water solubility data for different toluene derivates related with this extration [5]–[7]

Temperature	2,4-dinitrotoluene	2,6-dinitrotolene	2-nitrotoluene	4-nitrotoluene	toluene
20 °C	1.03E-03 mol/l	8.07E-04 mol/l	4.44E-03 mol/l	2.12E-03 mol/l	6.37E-03 mol/l
30 °C	1.48E-03 mol/l	1.46E-03 mol/l	4.74E-03 mol/l	2.35E-03 mol/l	5.07E-03 mol/l
40 °C	2.28E-03 mol/l	2.32E-03 mol/l	5.64E-03 mol/l	3.05E-03 mol/l	–
62 °C	5.35E-03 mol/l	–	–	–	1.73E-02 mol/l

Reaction intermediate MNT can be used as extraction agent, however, it contains a quite high amount of DNT because of the technology. As the basis and starter reagent of TDI production, the toluene can be considered also as extraction material, since it does not have any dissolved DNT, yet more water soluble *(Table 1)*. Toluene could be a better choice for this DNT recovery step.

Our goal is to examine the capability of toluene and intermediate MNT as extracting agents, to measure its capacity and compare its partition coefficient results. To maximize the information about this DNT recovery technology, data were gathered from ChemCAD simulations which were based on the distillation step.

1. APPLIED METHODS

It was necessary to develop a method that can be appropriately used for demonstrating the technology where MNT or toluene is applied as an extracting agent. On one hand a laboratory system was set up for carrying out experiments and providing data, on the other hand simulation was used so as to calculate the efficiency of the suggested extracting agents.

1.1. Experimental method for extraction step

Our laboratory system was based on a 1,500 ml reactor vessel with duplicated wall for its temperature control. A mixer was put inside the vessel to mix-up the two phases and help with even homogenization. Julabo® thermostat and Digi-Sense® thermometer have been used. Temperature was set to 65 °C. For the quantitative analytical measurements HPLC equipment was used.

The schema on which our experiments are based requires fresh extracting agents at each step *(Figure 3)*. Only a small amount of agent is needed, however the quality of this method gives great yields of extract at the end. During the experiments 1,000 ml red water was added into the reactor vessel with 27 g of extracting agent. After an hour of intense mixing, the two phases were separated from which samples were taken.

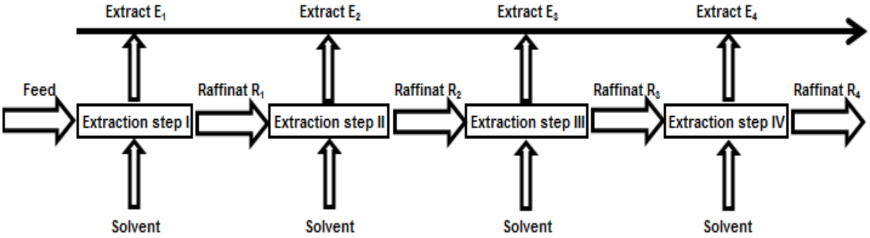

Figure 3
The schema of this multi-step extraction

The red water was fed back to the vessel with fresh extracting agent restarting the experiment. This procedure was repeated four times with MNT and toluene extracting agents. As a result, the DNT content in red water appeared constant. One of the targets was to gather accurate data for plant equipment's design.

1.2. Simulation method for distillation step

Data were collected by analyzing the samples that were taken giving the possibility to obtain more information about the extracted red water quality in relation with solved extracting agents. By using this data, simulations could have been set up in Chemstations™ ChemCAD environment, to check the heat needs for the extracting agents and water distillation process. Through knowledge of these results, the economic factors of the whole technology also could have been examined.

1.3. Combination of methods

The best way is to see the extraction and distillation technological steps as a whole process. In this study the authors first obtained information about each step separately and then tried to conclude the main points. Finding the best extracting agent is good for the extraction step as well as for the after cleaning distillation procedure, which has a rather great heat need.

2. RESULTS OF EXTRACTION

2.1. MNT

The extraction of red water (initial DNT content: 135,350 mg/l) by the use of MNT seems inadequate because notable amount of DNT remained in the red water with 150 mg/l concentration. This DNT concentration in red water became constant and did not go lower. The MNT's DNT content was raised up to 155,000 mg/l *(Table 2)*. After the experiments 1,100 mg/l of MNT was remained in the red water requiring to be distilled.

Table 2

MNT and toluene extraction results when different amount of extraction agents with variant quality were used

	DNT content after the steps, starting with used water and fresh extracting agents [mg/l]			
	First extraction	**Second extraction**	**Third extraction**	**Fourth extraction**
MNT *(27 g)*				
Red water	214	163	158	151
K-value	711	867	881	935
Toluene *(27 g)*				
Red water	92	11	2	0.2*
K-value	499	571	254	221
Toluene *(14 g)*				
Red water	141	48	8	2
K-value	647	466	515	383
Toluene° *(14 g)*				
Red water	246	191	179	161
K-value	737	549	547	566

2.2. Toluene

The same amount of toluene was measured (27 g) as in the case of MNT for the extraction of 1,000 ml red water. After the extraction DNT concentration in toluene was 45,786 mg/l. The remaining DNT in the red water was infinitesimal and it was out of our proper measuring range* (it was under 0.2 mg/l) *(Table 2)*. The residual toluene concentration was measured, its content in the red water was 260 mg/l. This amount needs to be distilled out from the system. In another experiment less toluene (14 g) was added as extracting agent. The extraction efficiency was worse, more steps were required for the cleaning process *(Table 2)*. This experiment was repeated with model toluene, where the DNT concentration was set to

82,750 mg/l in the toluene. This experiment showed that the efficiency was already decreased when significant amount of DNT was solved in the extracting agent because DNT content in the red water lower less *(Table 2)*.

2.3. K-value – partition coefficient

The partition coefficient numbers were determined by the following equation (1).

$$K = \frac{c_{DNT}\,organic\ solvent}{c_{DNT}\,water} \tag{1}$$

The results are demonstrated by the following diagrams. According to *Figure 4* the DNT concentration in water stayed relatively high until the end of the process (up to 150 mg/l) when intermediate MNT has been used. This phenomenon can be explained by the fact that MNT already contained DNT which reduced its extraction capacity. However, until the second extraction step the K-values were increased and afterwards the K-values remained constant and high (935).

In the case of *Figure 5* the highest K-value was achieved after the second step (571) and then it was decreased, which could be explained by decreased amount of DNT in water in function of extraction steps. The water's DNT content was decreased as well, to 0.2 mg/l at the end of the fourth extraction step. According to the results, both intermediate MNT (27 g) and toluene (27 g) are favorable because intermediate MNT has higher K-values. Yet, toluene also works since there is less DNT remaining in the red water.

2.4. Extracting agent in red water

After the experiments the data were collected and evaluated. The content of the remaining extraction agents in water were determined in mg/l concentration. These amounts of extracting agents need to be distilled.

• MNT in red water	1,100 mg/l
• Toluene in red water	260 mg/l

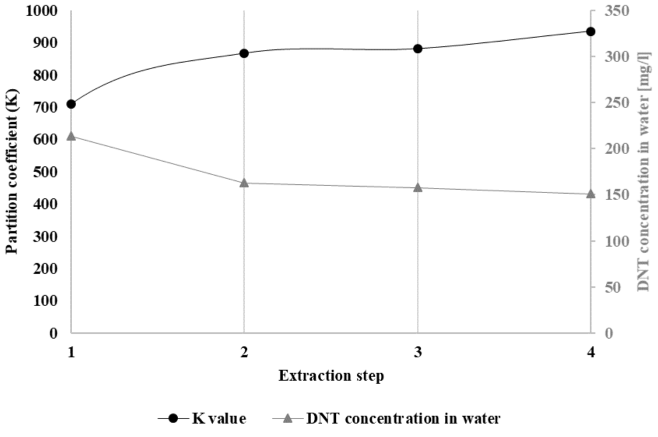

Figure 4
Partition coefficient and DNT's water concentration change in the function of extraction steps, with MNT extracting agent

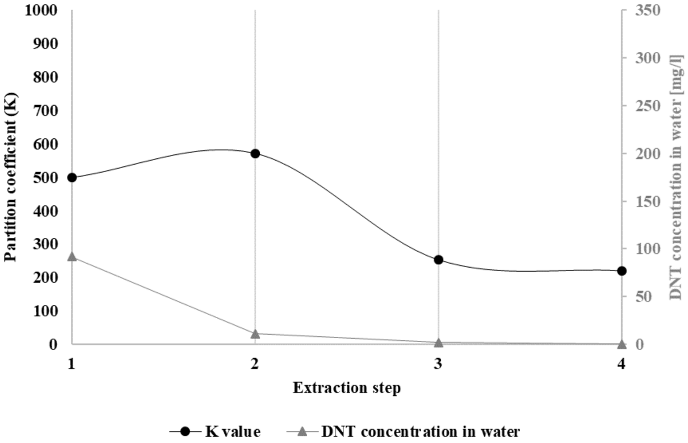

Figure 5
Partition coefficient and DNT's water concentration change in the function of extraction steps, with toluene extracting agent

3. RESULTS OF DISTILLATION

First of all, a simulation in Chemstations™ ChemCAD environment has been set up. UNIFAC global K-value model and model vapor/liquid/liquid/solid global phase option have been chosen because of the azeotrope (toluene-water).

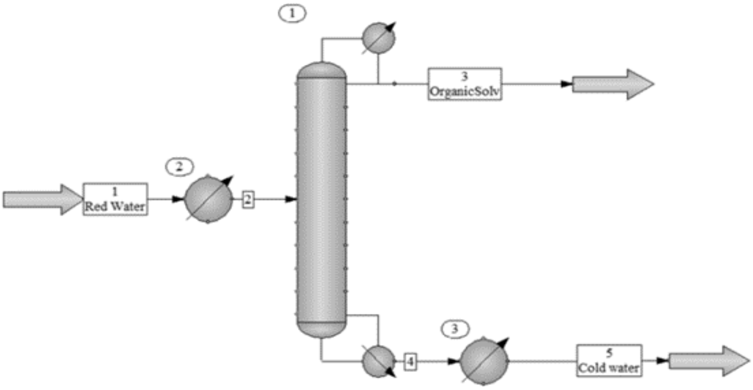

Figure 6
The basic design of the distillation step, created in Chemstations™ ChemCAD environment where equipment 1: distillation column, 2 and 3: heat exchangers; stream 1: red water, 2: heated red water, 3: top product, 4: bottom product, 5: cooled bottom product

3.1. MNT

The boiling point (bp.) of MNT is 222 °C, the water's is 100 °C if p = 101.3 kPa [8]. Due to this difference steam distillation is needed. This means to remove the MNT, a relative large volume of water needs to be boiled in order to eliminate all of the MNT.

This steam distillation was modelled as packed column (Pall ring tower packing was used), where the pressure was set to 0.040 bar and it boils 32.2 liter/hour for each cubic meter of red water to sprout the MNT out. The reflux ratio is 2.5. Less than 3E-05% of all MNT remained in the red water. Based on these data, it was calculated that this system needs 558,438.5 kJ/h/m^3, if the heat exchangers' efficiencies are 90% *(Table 3)*. This setup is the optimum for this distillation.

In this case heat integration is possible, but not efficient, because the pre-heater (*Figure 6*, equipment number 2) needs to heat up the red water to 100 °C, and there are not enough ΔT temperature difference between the two streams. The red water could condensate the bottom column product water to increase its temperature a little bit, but also needs to go through in the pre-heater, which works with steam to reach the 100 °C. Building a pre-heater is considered to have low efficient.

According to the results the MNT distillation is highly energy consuming.

3.2. Toluene

Toluene creates azeotrope with water, bp. of toluene: 110.9 °C, bp. of the toluene-water azeotrope: 84.1 °C, ($p = 101.3$ kPa) [9], which helps to eliminate it more easily than the MNT. Due to the azeotrope property the distillation became more energy efficient. For this distillation tray columns could be more suitable [10], therefore a model was created.

After the optimization process of this column the number of trays were set to 6 (actual trays 4) and feed stream for red water was set to the second tray. The optimal working pressure value of the column was 0.5 bar using at least 75 °C feed stream (*Figure 6* stream "Red Water"). This adjusted pressure gave us the best results for heat demand.

The 0.5 bar pressure column also requires an 80 °C input temperature, which means a small pre-heater is needed. In this case, a pre-heater cannot be integrated because the bottom product was only 81 °C, but, if 1 bar pressure is used the bottom product is 99 °C and can heat up the feed stream including red water. Reflux ratio is 1 in both cases.

The energy required for these circumstances can be seen in *Table 3*. For both 0.5 bar and 1 bar pressures, the system could distillate all toluene, only less than 2.7E-05% of all toluene remained in the water, and 0.4 l/h for each cubic meter of toluene-water mixture would be distilled.

Table 3

Distillation pressures and heat needs for the extracting agents

	Pressure [bar]	Needed heat [kJ/kg/m^3]	Is heat integration possible?
MNT (1,100mg/l)	0.040	5.6E05	No
Toluene (260mg/l)	0.5	0.3E05	No
Toluene (260mg/l)	1	1.1E05	Yes

CONCLUSION

According to the experiments it can be seen that the pure fresh toluene can dissolve more DNT than the intermediate MNT. Less toluene remains in the water after the extraction than MNT extracting agent. Even more DNT can be withdrawn from the red water whether toluene is chosen to be used in the extraction step. Less energy is needed to distillate red water in the case of toluene extraction and recover the useful organic materials of the water (toluene and MNT and DNT) which can be reused in order to create less organic chemical waste. By two-step extractions with 2% of toluene more than 99.9% DNT recoveries can be reached.

Heat integration is also a possible process in the case of toluene distillation using 1 bar pressure in the column. However, the heating energy needs drops by more than 80% without heat integration, and by 85% with heat integration. If 0.5 bar pressure is applied the energy need of heating decreases by more than 93%. The vacuum pump at the top of the column would need less energy as well than in case of MNT distillation, where 0.040 bar pressure is required.

To summarize this series of experiments, it is suggested to choose toluene over intermedia MNT as extracting agent in TDI technology.

ACKNOWLEDGMENTS

The authors acknowledge the research possibility for Wanhua-BorsodChem Ltd. and the support for Tamás Purzsa Vice President of Chief General Engineering. This research was supported by the European Regional Development Fund in the framework of the GINOP-2.3.4-15-2016-00004 project.

REFERENCES

[1] I. Boustead (2005). Tolylene diisocyanate (TDI). *Eco-profiles Eur. Plast. Ind.*, No. March, pp. 1–20.

[2] W. J. Mazzafro, S. I. Clarke, M. S. Simpson, and R. Van Court Carr (2003). Weak acid process for producing dinitrotoluene – EP 0 903 336 B1.

[3] H. Hermann, J. Gebauer, and P. Konieczny (1996). Industrial Nitration of Toluene to Dinitrotoluene. *Josef Meissner GmbH Co.*, No. 5, pp. 234–249.

[4] F. Fiedler, H.-J. Schöbel, and M. Otto (2000). Identification of Nitrogen Compounds from Degradation of Dinitrotoluene and Toluylenediamine Isomers Within an Industrial Purification Plant. *Microchim. Acta*, Vol. 135, No. 1–2, pp. 1–7.

[5] D. J. L. Prak and D. W. O. Sullivan (2007). Solubility of 4-Nitrotoluene, 2,6-Dinitrotoluene, 2,3-Dinitrotoluene, and 1,3,5-Trinitrobenzene in Pure Water and Seawater. *J. Chem. Eng.*, pp. 2446–2450.

[6] J. M. Phelan and J. L. Barnett (2001). Solubility of 2,4-Dinitrotoluene and 2,4,6-Trinitrotoluene in Water. *J. Chem. Eng.*, Vol. 46, pp. 375–376.

[7] S. H. Yalkowsky, Y. He, and P. Jain (2010). *Handbook Of Aqueous Solubility Data*.

[8] D. R. Lide (2005). *CRC Handbook of Chemistry and Physics, 85th Edition*. Vol. 53.

[9] J. Gmehling, J. Menke, J. Krafczyk, K. Fischer, J. Fontaine, and H. V Kehiaian (1996). Azeotropic Data for Binary Mixtures. *Handb. Chem. Phys.*, pp. 6-210–6-228.

[10] M. Siegert, J. Stichlmair, J. U. Repke, and G. Wozny (2000). Heterogeneous azeotropic distillation in packed columns: experimental results. *Chem. Eng. Technol.*, Vol. 23, No. 12, pp. 1047–1050.

Materials Science and Engineering, Volume 43, No. 1 (2018) pp. 79–91.

THE EFFECT OF AGE ON COMBUSTION PROPERTIES OF ENERGY WILLOWS

DÓRA MENTES[1]–CSABA PÓLISKA[2]–TAMÁSNÉ SZEMMELVEISZ[3]

In this study, we investigated the conditions of combustion of one- and two-year-old Energo twigs. We were inquired into the answer how the age of the Energo willow influences its combustion properties. During the research we have determined that some properties may be significantly affected by the age.

Keywords: energy willows, combustion, higher heating value, moisture, ash

INTRODUCTION

Due to the fight against climate change and the ever-increasing energy needs, renewable energy sources have come into view. Using of them, we can replace the fossil fuels and reduce the release of greenhouse gases that cause climate change.

Renewable energy sources include biomass. A large group of it is the woody energy crops. We have many examples of setting up and operating energy woodcutters in the world. In Europe we find intensive experimentation in Sweden, Germany, Great Britain, Croatia, Serbia and Montenegro, Finland, and Hungary. In these countries, studies are carried out primarily with willow, poplar, acacia, birch and alder clones [1].

The woody plants of acacia, willow and poplar have favorable cultivation conditions because of the continental climate in Hungary. The range of wood species and breeds that can be used for the production of woody plantations in Hungary is set out in the MARD 45/2007. number decree. According to this, planting technology can only be used for the aforementioned plants [1], [2].

In researches on energy crops found in international literature, the same plant variety may exhibit different properties. These differences can be explained by dissimilar climatic conditions, soil quality and planting systems in different European countries. Besides the above mentioned parameters, the combustion properties can be influenced by the different genotypes and age of the plants as well. For example, the willow calorific value change widely, depending on the above-mentioned factors, up to 16.2 to 22.6 MJ/kg [3], [4], [5], [6], [7].

Investigations on woody energy plantations focus primarily on harvesting methods and their economic, energetic and environmental impacts.

The aim of our work is to determine how the age of the Energo willow influences its combustion properties.

---

[1] Department of Combustion Technology and Thermal Energy, University of Miskolc
H-3515 Miskolc-Egyetemváros, Hungary
mentes.dora@t-online.hu

[2] Department of Combustion Technology and Thermal Energy, University of Miskolc
H-3515 Miskolc-Egyetemváros, Hungary
tuzcsaba@uni-miskolc.hu

[3] Department of Combustion Technology and Thermal Energy, University of Miskolc
H-3515 Miskolc-Egyetemváros, Hungary
tuzszemt@uni-miskolc.hu

1. LABORATORY EXPERIMENTS

During our research we examined in detail the combustion properties of one- and two-year-old Energo willow. This will help to ascertain how the age of the plant affects the conditions of its firing.

The pictures of the twig from the examined willows are shown in *Figure 1*.

Figure 1

Twigs of the one-year-old (right) and two-year-old (left) Energo willow

1.1. Moisture content

Determination of the hygroscopic moisture content of the biomass happens in drying oven at 105 ± 5 °C by mass constant, according to MSZ EN 14774:2010 standard. The final results were calculated with the following formula [8]:

$$W = \frac{m_1}{m} \times 100,\ \text{\% m/m} \tag{1}$$

where

W	hygroscopic moisture content [% m/m],
m_1	weight loss (of the sample) on drying [g],
m	the initial weight of the sample [g].

One of the most important combustion parameter is the moisture content. The moisture content of willow sample can be influenced by several factors: what time of the year was it harvested, how much diameter it has and what genome it has.

1.2. Ash content

Ash is the solid burnings residues left from the complete combustion of fuel. Determination of it happens in closed chamber at 815 ± 15 °C by mass constant, according to MSZ EN 14775:2010 standard. All results are reported relative to the oven dry weight of the sample, according to the formula [8]:

$$A = \frac{m_3 - m_1}{m_2 - m_1} \times 100, \text{\% m/m} \tag{2}$$

where

A	ash content [% m/m],
m_1	the weight of the crucible [g],
m_2	the initial weight of the crucible and the sample together [g],
m_3	the weight of the crucible and the ash produced [g].

The ash content of the samples, as well as their moisture content, can be influenced by a number of factors such as the breed of willow (genotype), the environment where it grew, the way and the time of harvest, and other conditions.

One of the studies examined a sample of 19 different genotype in five different environments. The samples with different genotype had an ash content between 1.27 and 2.57% m/m. In the case of environmental impact analysis, the range of the ash content of the samples is smaller: 1.37–2.16% m/m. So the environment has less impact on ashes than the genotype of the samples [9].

In another study, two types of willow samples were investigated. It was found that the age of the samples significantly influenced their ash content. While one breed of willow the one-year-old samples – in the case of the other breed the three-year-old sample had the largest ash content. The difference between the tree and bark part was also examined. For both species, the tree part contained less ash than the bark part [6].

The ash content of the plants harvested by the machine is also lower than that of manually harvested plants, which is explained by the fact that several pollutants may adhere to the surface of the plants when they are harvesting by hand [10].

1.3. Ultimate analysis

In this study, a Carlo Erba EA1108 type elemental analyser was used for the measurement of the a C-, H-, N-, S-, O- content in the biomass, according to MSZ EN 15104:2011 standard. The elemental analysis is based on the perfect combustion of the fuel. From the composition of the resulting flue gas, we can deduce the quantity of elements forming the sample. The flue gas is driven by helium carrier gas through the oxidizing and reducing parts to a chromatographic column where the thermal conductivity sensor detects the CO_2, H_2O, N_2, SO_2 gas components. From these data, the amount of elements in biomass can be calculated [11].

1.4. Determination of higher heating value (HHV)

Calorific test were performed using a Parr 6200 type isoperibol oxygen bomb calorimeter according to MSZ EN 14918:2010 standard.

The higher heating value of the samples were automatically computed by the data processing system. The principle of the measurement was based on a substitution procedure in which the heat obtained from the sample was compare with the heat obtained from combustion of a similar amount of calibration material (benzoic acid) whose calorific value was known [12].

Measurement were obtained by burning the representative sample in high pressure oxygen atmosphere within a metal pressure vessel or bomb. The energy released by the combustion. The amount of heat released during combustion is absorbed by distilled water.

During the process, the device records the temperature change of the distilled water. Multiplication of this data and calorimeter heat capacity, we can calculate the heat released during combustion. By dividing this value, the mass of the sample is obtained by releasing heat from the unit weight mass [12].

In several studies the correlation between the age and calorific value of the willow samples was studied. In the samples of 15 genomes of nine breeds of willow, the correlation was found that the calorific value of one-year-old samples was higher than that of the three-year-old [7].

In another study, the calorific value of wood and bark of two breed of willow was studied. In the case of both willow it can be stated that the heating values of one-year-old wood parts are in all cases greater than the calorific values of the two- or three-year-old wood parts. The bark tests showed different results between the two breeds. In one case, one-year-old bark samples, while the other one, three-years-old bark samples had higher calorific value [6].

1.5. Ash softening characteristics

The softening and melting parameters of the ashes and slags were determined with a Sylab IF 2000G type ash fusion analyzer and an IRF 1500 furnace attached to it. The morphological changes of the ash and slag samples were recorded with a digital camera. The instrument allows for the execution of standardized measurements according to CEN/TS 15370-1-2006, ISO 540 1995, ASTM E 953-8 (2004), AFNOR M03048, BRITISH1016-70, AS 1038.15, DIN 51730.

Cylindrical specimens of 3 mm height and 3 mm diameter were made of ashes, which were placed on a sample holder and slid into the furnace. The device registers the image of the test specimen placed in the furnace using the digital camera as a function of the temperature of the samples and the softening parameters can be determined from the series of images. The softening point meter is made up of the following parts:

- furnace heated up to 1,600 °C, with a tubular working surface comprising a sample and a furnace atmosphere during the measurement;
- a softening point meter incorporating the external control equipment of the furnace atmosphere and the furnace temperature, which is built with computer data collection software;
- a digital camera for photographing samples of willow.

Melting features were characterized with the specific temperature points given below.

- Initial Deformation Temperature (IT): the temperature at which the tip of the test sample shows 5% shrinkage in height as compared to the original height of the test sample.
- Deformation Temperature (DT): the temperature at which the test sample starts to fuse into a hemispherical shape with edges and corners starting to round off.
- Softening temperature (ST): the temperature at which signs of softening (change in surface, rounding of edges) start appearing, the test sample starts blowing up.
- Hemispherical temperature (HT): the temperature at which the shape of the test sample resembles a hemisphere, the hight of the test sample is equal to 1/2 of the width of the base.
- Fluid temperature (FT): the temperature at which the sample height shrinks to 1/3 of the original height, i.e. the sample melts.

1.6. Ash characterization

The scanning electronic microscopy and energy dispersive spectroscopy (SEM/EDS) analyses were applied to the ash and slag samples were observed experimentally, confirming prediction using the fusibility properties.

This type of preparation allows to observe the morphology of the agglomerates, and to identify the major elements that may be responsible for the melting effects. It was used a high resolution Zeiss Evo MA10 scanning electron microscope. Samples were coated with a thin golden layer, in order to obtain the conductivity needed for SEM observation. Software included in the equipment allowed data acquisition for semi-quantitative analysis.

1.7. Thermoanalytical examination

Thermal analysis contains a group of techniques in which the property of the sample is monitored against temperature and time. Due to the temperature increase, the structural composition of the sample and the process of the drying, the disappearance of volatile substances and oxidation can be determined. Thermoanalytical methods are shown in *Table 1* [14].

Table 1

Major Thermoanalytical Methods [14]

The name of the method	The measured property as a function of temperature	Applied device
Thermogravimetry (TG)	mass	Thermobalance
Differential Thermogravimetry (DTG)	speed of mass change	Manufactured with a computer
Differential Thermoanalysis (DTA)	temperature difference between the sample and the reference material	DTA equipment
Dual Differential Thermoanalysis (DDTA)	speed of change in the temperature difference between the sample and the reference material	Manufactured with a computer

A derivatography is a complex thermoanalytical method, by which heat energy and weight changes that accompany transformations during the heating of the test sample can be determined simultaneously with one sample. The suitable instrument for this measurement is a derivatograph that automatically picks up the TG, DTA, DTA and DDTA curves at the same time. With this method, the slightest mass change or heat change can be detected with the highest sensitivity and precision. The equipment we use is MOM Q1500D type derivatograph [8], [15].

There are four curves on the derivatogram, which are the following [8].

- Thermogravimetry (TG): this curve shows the mass change of the sample as a result of a rise in temperature.
- Differential Thermogravimetry (DTG): where the TG curve has an inflection point, there is a peak on the DTG curve, which makes it an accurate picture of mass-change processes in the sample.
- Differential Thermoanalysis (DTA): the minium of the resulting curve refers to endothermic process and the maximum of it refers to exothermic process.
- Dual Differential Thermoanalysis (DDTA): where the DTA curve has an inflection point, there is a DDTA curve peak to give an accurate picture of the thermal processes occurring in the sample.

2. RESULTS AND DISCUSSION

2.1. Characterization of fuels

The hygroscopic moisture content in air-dry state, while the ash content, the elemental composition and the calorific value in dry state of the examined energywillows are shown in *Table 2*.

Table 2

Proximate analysis, ultimate analysis (% m/m) and calorific values of the fuels

Sample	**W** **% m/m**	**Ash** **% m/m**	**C** **% m/m**	**H** **% m/m**	**N** **% m/m**	**O** **% m/m**	**S** **% m/m**	**HHV** **MJ/kg**
Energo 1 year	7.31	1.81	49.84	5.47	0.73	42.12	0.05	19.0
Energo 2 year	7.39	1.9	48.06	5.49	0.04	44.46	0.05	18.6

The hygroscopic moisture content of the different ages of energy willows are 7.3 and 7.4% m/m. Ashes of energy willows are also similar: 1.8–1.9% m/m. The ultimate analysis shows that the percentage of carbon, hydrogen and oxygen are comparable for all samples. All willow breeds are characterized by very low sulphur content (0.05% m/m), implying that SOx emissions during combustion are not of concern for these fuels. Because of the similar hygroscopic moisture-, carbon, hydrogen- and oxygen content, there is no significant difference between the calorific value of one- and two-year-old samples. In the two-year-old samples, the nitrogen content is lower compared to one-year-old. This is due to the fact that nitrogen is found in those parts of the biomass that are still growing. The willow shows a stronger growth in the first year, the nitrogen content decreases in the second year, so the growth rate of the willow is also decreasing. The decreasing nitrogen content of the two years and increasing oxygen content means improving the combustion properties.

2.2. Softening characteristics

The pictures of the softening test of the ash molds of twigs of energy willow made under laboratory conditions are shown in *Figure 2*.

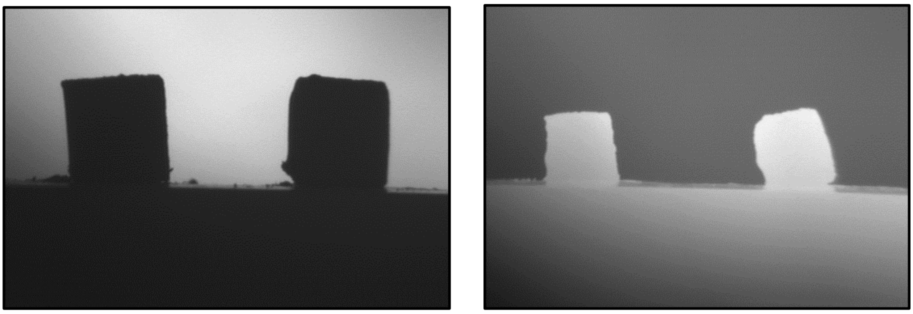

Figure 2

Pictures of the softening test of one-year-old Energo sample at 401 °C (left) and 1,541 °C (right)

From the five typical temperature points, only two temperature points can be detected during the test [sintering temperature (IT) and deformation temperature (DT)]. The samples showed only a small shrinkage, which is due to the high Ca content found in ash. We couldn't do the softening test of the ash of the two-year old willow because of the available little amount of ash. There is also a high amount of Ca in the ashes of two-year-old Energo willow, so the ash would probably be the same behavior during the test.

The *Figure 3* shows the degree of change in the size of ash samples from one-year-old twigs of willow.

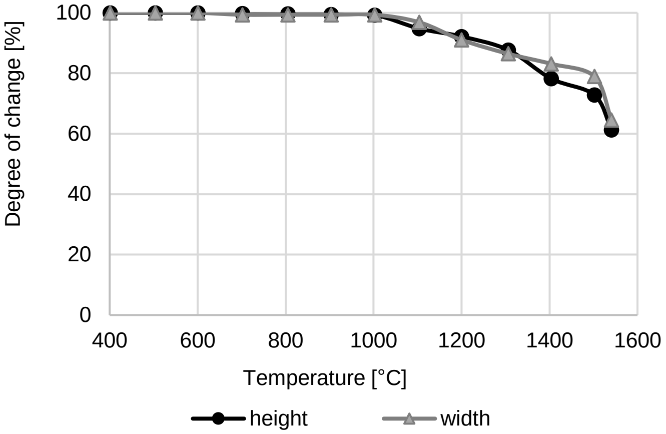

Figure 3

The degree of change in ash samples (one-year-old twigs of willow)

It can be seen that the height and width of the samples remain unchanged up to 1,000 °C. Between 1,000 °C and 1,550 °C, the rate of decrease in height and width is the same. At 1,541 °C, the height and width of the ash sample were approximately 60% of the original height and width.

2.3. Ash characterization using scanning electronic microscopy – energy dispersive spectroscopy

It can be found below the SEM recordings of the samples and the avarage compositions of the recordings and the composition of the selected points.

We homogenized the one-year-old ashes with mortar. It can be seen that several particles in the sample are drawn, mainly CaO particles. The avarage compositions of the recordings and the composition of the selected points shown in *Figure 4* are shown in *Table 3*.

Table 3

Semi-quantitative analysis of Energo 1 year willow

Ashes of Energo 1 year willow (see Fig. 4.)	**Elements [% m/m]**													
	C	O	Na	Mg	Al	Si	P	S	Cl	K	Ca	Ti	Mn	Fe
a) picture average	9.5	30.66	1.09	4.87	0.56	0.73	6.28	2.36	0.25	16.24	26.68	0.13	0.29	0.38
b) picture average	12.15	35.89	0.43	4.48	0.13	0.52	5.78	1.88	0.08	15.20	22.40	0.08	0.41	0.57
b) picture, point 1	4.96	28.83	1.12	6.56	0.78	0.85	8.10	1.88	0.39	19.72	25.90	0.06	0.48	0.38
b) picture, point 2	7.99	33.58	0.68	1.02	0.70	0.75	1.03	1.60	0.58	3.54	46.92	0.46	0.54	0.62
c) picture average	15.75	35.36	0.53	3.69	0.07	0.46	5.10	1.49	0.00	14.76	22.11	0.00	0.30	0.38
d) picture average	9.50	30.66	1.09	4.87	0.56	0.73	6.28	2.36	0.25	16.24	26.68	0.13	0.29	0.38

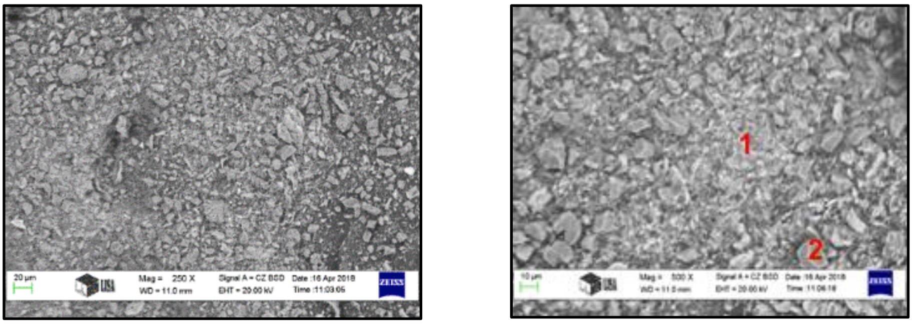

a) Energo 1 year, magnification: 250×   *b) Energo 1 year, magnification: 500×*

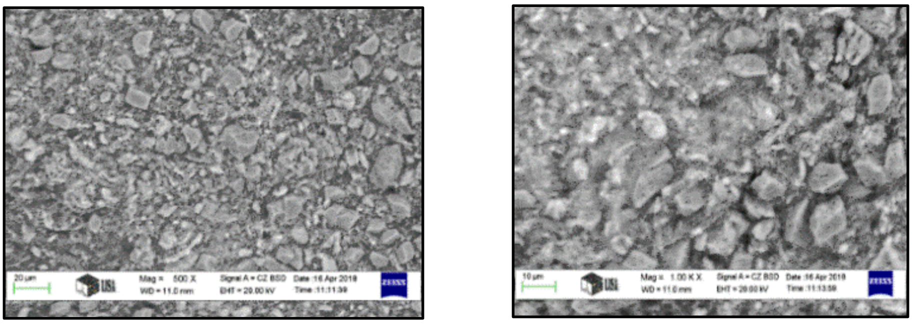

c) Energo 1 year, magnification: 500×   *d) Energo 1 year, magnification: 1,000×*

Figure 4
SEM image of ashes of Energo 1 year willow

One of the major problems when burning a biomass, is that the melting point of the resulting ash is similar to the furnace temperature and the molten ash causes significant problems in the combustion chamber (heat insulation of heat exchanger surfaces). The decrease of the melting point of the ash is mainly caused by the alkali metal and phosphorus oxides contained therein. Although the K content is relatively high in the ashes of one-year-old willow, due to the high Ca content, this does not cause any major damage to the combustion chamber, because the softening temperature increases.

We were inquired into the answer how the location of different particles were affected by the homogenization in unhomogenised ash, that is why the ashes of the two-year-old samples were not homogenized. It can be seen that the CaO particles are grouped together in a row. The Ca content of the one- and two-year-old plants is also high, which can be explained by the fact that these plants are probably planted in calcic/lime soil. The avarage compositions of the recordings and the composition of the selected points shown in *Figure 5* are shown in *Table 4*.

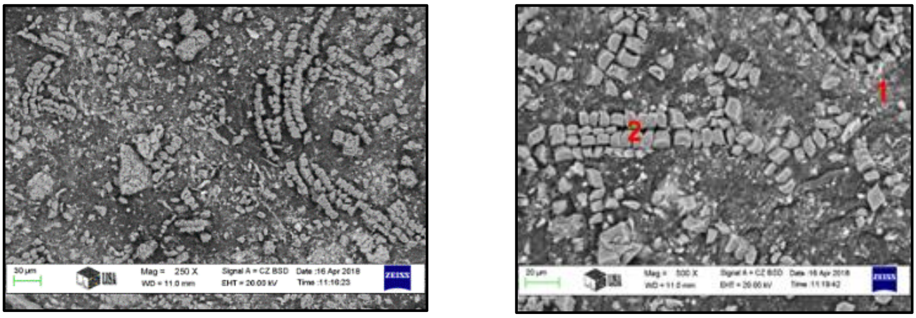

a) Energo 2 year, magnification: 250× *b) Energo 2 year, magnification: 500×*

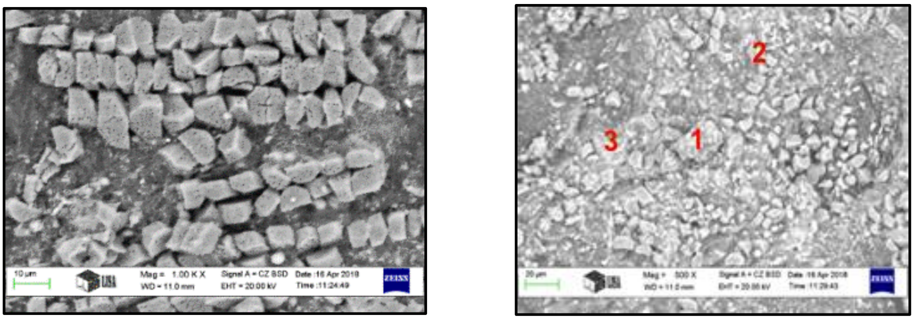

c) Energo 2 year, magnification: 1,000× *d) Energo 2 year, magnification: 500×*

Figure 5
SEM image of ashes of Energo 2 year willow

Table 4
Semi-quantitative analysis of Energo 2 year willow

Ashes of Energo 2 year willow (see Fig. 5.)	Elements [% m/m]												
	C	O	Na	Mg	Al	Si	P	S	Cl	K	Ca	Ti	Mn	Fe
a) picture average	22.78	34.62	0.74	2.39	0.66	1.13	2.73	0.98	0.00	5.67	27.33	0.04	0.37	0.55
b) picture average	24.71	34.98	0.77	1.96	0.38	0.85	2.25	0.85	0.12	4.70	27.41	0.13	0.34	0.56
b) picture, point 1	34.36	37.53	0.82	3.55	0.31	0.32	2.60	0.83	0.00	4.17	14.98	0.00	0.13	0.40
b) picture, point 2	9.76	38.68	0.86	0.94	0.70	0.75	0.97	0.87	0.47	1.78	43.52	0.27	0.18	0.26
c) picture average	13.00	35.26	0.49	1.63	0.50	0.59	1.77	1.08	0.30	3.36	41.09	0.11	0.24	0.56
d) picture average	18.38	35.81	0.48	2.80	0.40	0.66	3.06	1.02	0.04	6.10	29.93	0.17	0.41	0.73
d) picture, point 1	7.53	37.76	0.88	1.58	0.62	0.61	1.48	0.90	0.23	1.87	46.28	0.00	0.15	0.10
d) picture, point 2	7.82	30.48	0.78	0.95	0.77	0.78	0.95	1.46	0.65	2.06	51.81	0.52	0.50	0.48
d) picture, point 3	6.69	39.29	1.16	6.26	0.27	0.59	9.42	2.02	0.13	14.55	18.91	0.11	0.13	0.45

The ash of two-year-old sample has a higher carbon content, suggesting that the burning of carbon in the samples was incomplete. Carbon content can be reduced by intensifying air/fuel mixing or possibly by tertiary air intake. Due to the carbon content thus burnt, the amount of fly ash may be reduced in the flue gas.

Compared to the ash of one year old samples, the sulfur, phosphorus, potassium, magnesium content and calcium content increase in the two years old samples. This can be explained by the fact that in the first year of the plant, due to its stronger growth, it drains much more nutrients from the ground and supplies the nutrients needed to its younger parts.

The results of the elemental composition of the ashes confirm the results of the softening tests.

2.4. Thermoanalytical examination

Figure 6 and *7* shows a derivatogram of one- and two-year-old willow samples.

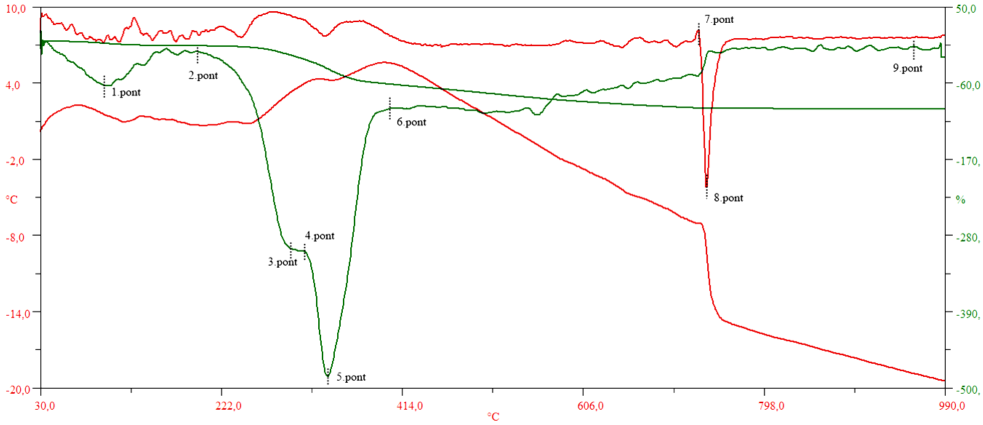

Figure 6
Derivatogram of the one-year-old willow

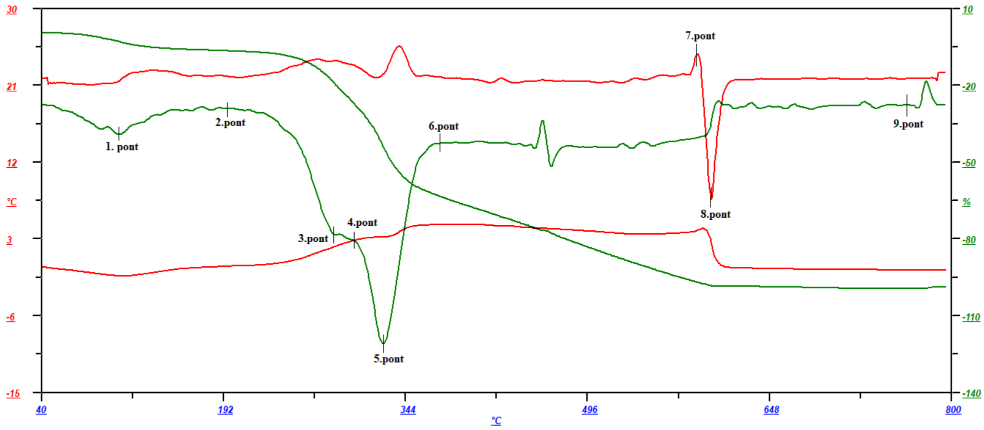

Figure 7
Derivatogram of the two-year-old willow

Table 5 shows the parameters of thermal analysis of the one- and two-year-old samples.

Table 5
Parameters of thermal analysis investigation

Parameters	One-year-old	Two-year-old
Starting temperature [°C]	30	40
Ending temperature [°C]	1,000	800
Heating speed [°C/min]	8	10
Test time [sec]	122	77.5
Sample weight [g]	101.4	54.6

Table 6 shows the temperature and weight change of the characteristic points that can be read from the derivatogram.

Table 6
Typical temperature and weight change points for the derivatogram

Typical point	One-year-old		Two-year-old	
	T [°C]	TG [%]	T [°C]	TG [%]
1	98.3	–2.75	105.1	–3.02
2	194.2	–6.28	195.7	–6.52
3	292.4	–19	285.1	–19.74
4	310.2	–26.37	301.6	–27.95
5	334.2	–39.1	325.5	–44.62
6	403.0	–62.0	373.9	–63.71
7	727.8	–96.16	587.6	–96.99
8	736.3	–96.55	599.2	–98.33
9	955.2	–97.12	762.7	–99.4

Based on the derivatogram of the one- and two-year-old Energo willows, the following can be established:

- drying process of Energo willlows begins at ambient temperature and continues at an accelerating pace up to 98.3 °C in case of one-year-old, and 105 °C in case of two-year-old;
- at temperatures ranging from 95 to 110 °C the moisture is the most intense of leaving the samples;
- the drying of the tested samples at 194.2 °C (in case of one-year-old) and 195.7 °C (in case of two-year-old) it was completely completed;
- the leaving of the volatiles at a temperature between 195 and 200 °C and are accelerating at 334.2 °C (in case of one-year-old) and at 325 °C (in case of two-year-old);
- at temperatures ranging from 300 to 350 °C the leaving of the volatiles are the most intensive, and it ends at 403 °C (in case of one-year-old) and at 373 °C (in case of two-year-old);
- above 955 °C (in case of one-year-old) and 762 °C (in case of two-year-old) the weight loss the heat development and the combustion have been completed.

Based on this, it is possible to say that both samples has similar temperature of the completion of drying and starting temperature of the secession of the volatiles. Due to the differently selected parameters of the tests, temperature range of intensive combustion of the two-year Energo was lower and the combustion was completed at a lower temperature.

From the results provided by the derivativogram, the approximate structural composition of the energy willow (moisture, volatile, fixed carbon and ash content) can be calculated, as shown in *Table 7*.

Table 7

Calculated composition as the results of the thermoanalytical measurements

Name of the substance	**Moisture**	**Volatile**	**Fixed carbon**	**Ash**
	[% m/m]			
One-year-old Energo	6.28	55.72	34.55	3.45
Two-year-old Energo	6.52	57.19	34.62	1.67

By increasing age, hygroscopic moisture and fixed carbon content do not change significantly. Differences can only be measured in the volatile and ash content.

CONCLUSION

Based on the combustion tests carried out on one- and two-year-old energy willow, it can be stated that:

- Increasing the age of the plant reduces the nitrogen content and increases the oxygen content.
- The calorific value of one-year-old willow is greater than the two-year-old. This result is the same as that available in the literature.
- In the ashes of plants planted in presumably calcareous soil the Ca ratio and the ash softening temperature is high, therefore it hasn’t to be afraid of damage of the combustion chamber. In the ash of two-years-old sample the Ca ratio is higher than in one-year-old.
- Increasing the age of the willows reduces the sulfur, phosphorus, potassium, and magnesium content of the ash. This can be explained that biomass supplies nutrients to tissue parts that are still growing, in the older twigs it has less nutrients.
- Due to the differently selected parameters of the tests, temperature range of intensive combustion of the two-year Energo was lower and the combustion was completed at a lower temperature.

AKNOWLEDGEMENT

Hereby we express our special thanks to Tamás Koós for the ultimate analysis, thermal analysis and softening test, to Árpád Kovács and Dániel Koncz-Horváth for the scanning electron microscope measurements.

The research supported by the ÚNKP-17-2-I.-ME/16 New National Excellence Program of the Ministry of Human Capacities.

REFERENCES

[1] Zs. Barkóczy and R. Ivelics (2008). Energetikai célú ültetvények. *Erdészeti Kisfüzetek*, Magán-erdőgazdálkodási Tájékoztató Iroda.

[2] Cs. Póliska (2012). Fás szárú energianövények szerepe kistelepülések hőenergia ellátásában. *Anyagmérnöki Tudományok*, Vol. 37, No. 1, pp. 331–342.

[3] B. Klasnja, S. Kopitovic and S. Orlovic (2002). Wood and bark of some poplar and willow clones as fuelwood. *Biomass and Bioenergy*, Vol. 23, pp. 427–432.

[4] W. A. Kenney, L. Sennerby-Forsse and E. Layton (1990). A Review of Biomass Quality Research Relevant to the Use of Poplar and Willow for Energy Conversion. *Biomass*, Vol. 21, pp. 163–180.

[5] M. J. Stolarski, S. Szczukowski, J. Tworkowski and A. Klasa (2013). Yield, energy parameters and chemical composition of short-rotation willow biomass. *Industrial Crops and Products*, Vol. 46, pp. 60–65.

[6] J. Hytonen and J. Nurmi (2015). Heating value and ash content of intensively managed stands. *Wood Research*, pp. 71–82.

[7] M. Krzyżaniak, M. J. Stolarski, S. Szczukowski and J. Tworkowski (2014). Thermophysical and chemical properties of biomass obtained from willow coppice cultivated in one- and three-year rotation cycles. Chair of Plant Breeding and Seed Production University of Warmia and Mazury in Olsztyn. *J. Elem*., pp. 161–175.

[8] Mrs. T. Szemmelveisz (2006). Fás- és lágyszárú biomasszák tüzelhetőségi feltételeinek vizsgálata. Ph.D Dissertation, University of Miskolc.

[9] E. S. Fabio, T. A. Volk, R. O. Miller and M. J. Serapiglia, A. R. Kemanian, F. Montes, Y. A. Kuzovkina, G. J. Kling, L. B. Smart (2017). Contributions of environment and genotype to variation in shrub willow biomass composition. *Industrial Crops & Products*, Vol. 108, pp. 149–161.

[10] M. Eisenbies, T Volk, and J. Posselius (2016). *Research Summary: Characteristics of Willow Biomass Chips Produced Using a Single-Pass Cut-and-Chip Harvester. Extension*. April 20. 2016. http://articles.extension.org/pages/71883/research-summary:-characteristics-of-willow-biomass-chips-produced-using-a-single-pass-cut-and-chip-

[11] H. Kovács (2013). *Nehézfémekkel szennyezett bányaterületről származó fás szárú biomassza égetéssel történő ártalmatlanítási feltételeinek vizsgálata*. Ph.D Dissertatin, University of Miskolc.

[12] *Szilárd energiahordozó fűtőértékének meghatározása*. Felkészülési tananyag a Tüzeléstan tantárgy 1. számú laboratóriumi gyakorlatához; Miskolci Egyetem, Műszaki Anyagtudományi Kar, Tüzeléstani és Hőenergia Intézeti Tanszék.

[13] K. Hernádi (2012). *Nanokompozitok.* Szegedi Egyetem, 2012.

[14] *Termoanalitikai módszerek (termoanalízis)*. https://www.muszeroldal.hu/measurenotes/termoanalizis.pdf

[15] L. Laczkó Wojnárovitsné, I. Hrapka and K. Fórizs (2014). Anyagvizsgálati lehetőségek a SZIKKTI Labor Kft.-ben. *Üvegipari Szakmai Konferencia*, Budapest. https://szte.org.hu/upload/Anyagvizsg%C3%A1lati%20lehet%C5%91s%C3%A9gek%20a%20SZIKKTI%20Labor%20Kft.%20-%20ben%20%5BKompatibilit%C3%A1si%20m%C3%B3d%5D.pdf

Materials Science and Engineering, Volume 43, No. 1 (2018) pp. 92–97.

APPLICATION OF DIISOCYANATE ADDITIVE IN RIGID PVC/WOOD FLOUR COMPOSITE

KRISZTINA ROMÁN[1]–TAMÁS J. SZABÓ[2] –KÁLMÁN MAROSSY [3]

In this paper, we are dealing with the preparation of various PVC/Wood flour/MDI composites. Using additional additives to further develop Wood/PVC (WPVC) composites. For the tests, high purity MDI (methylene diphenyl diisocyanate) was used. This additional agent was used in order to improve the adhesion between PVC and wood. The agent was used for surface treatment of the wood. The wood was treated with 1%, 2% and 5% by weight MDI. A number of tests were performed on the samples. From the measurement results, the modifying effects of the MDI can be observed. In some measurements, the properties of the samples change, but only slightly. The mixture containing of 5% by weight MDI, showed greatly decreased thermal stability, but the tensile properties have increased. Based on the results, some properties of the specimens can be improved by increasing the amount of MDI.

Keywords: PVC, composite, mechanical properties

INTRODUCTION

Products made from polyvinyl chloride (PVC) can be found in many areas in the world. Most of these, we can commonly find it in the industry area, where various products of PVC appear, such as drainage pipes, window/door profiles or floor covers [1]. Because of the growing demand for special applications the need for product with special properties [2]. In order to satisfy demand for improvements, it is necessary to improve present materials or products, in order to get new materials with better properties. The properties of PVC can be improved by mixing it with additives. PVC is a difficult to break down biologically material; therefore it is preferred to be combined with natural materials. By mixing the two materials, the product becomes more biodegradable and also more resistant mechanically.

Beside to the wood fiber/flour the wood and plastic composites may be also made of thermoplastic or thermoset polymers. Processing techniques for thermoplastics had been known since the early 1900s. The wood additives are dispersed in the plastic melt, and then the mixtures are processed. The application of this technology has been going on since the 1980s and has since expended [1]. The natural flour or fiber can work as a strengthening phase in the polymer matrix, where it gives some positive properties compared to the original PVC [3]. These advantages are the reduced price and excellent mechanical properties and fire safety properties compared to wooden materials. Thus, the other advantages of the wood-PVC combination are reduction of the flammability of the wood, and also reducing the amount of toxic materials compounds from the burning of PVC. Variety of processing methods can be used to produce this wood-reinforced polymer composites, such as injection

---

[1] Institute of Ceramics and Polymer Engineering, University of Miskolc
H-3515 Miskolc-Egyetemváros, Hungary
polkrisz@uni-miskolc.hu

[2] Institute of Ceramics and Polymer Engineering, University of Miskolc
H-3515 Miskolc-Egyetemváros, Hungary
polsztam@uni-miskolc.hu

[3] Institute of Ceramics and Polymer Engineering, University of Miskolc
H-3515 Miskolc-Egyetemváros, Hungary
polkal01@uni-miskolc.hu

molding, extrusion or pressure molding [4]. However, the disadvantages of the WPVC materials are the change in weather ability. The worst of all of them are: degradation due to the high temperature or moisture absorption, UV radiation [5]. So it is necessary to use different types of additives in the mixtures. These additives are stabilizers, antioxidants, biocides and other additives which increase the lifetime of the product [6]. The problem with the mixing of thermoplastics and natural additives is the weak adhesion between them, which is the results of a low chemical affinity between the cellulose and the "hydrophobic" plastic [7]. The only way to increase the adhesion if we are using coupling agents between the additive and the polymer. In reality, it is very difficult to find the ideal coupling agent, which achieves the necessary requirements. In case of this research, the isocyanates proved to be reliable. The possibility of forming primary bonds – such as covalent bond's between cellulose and isocyanate – and forming secondary bonds between the isocyanate and PVC is present. The mechanical properties are improved by the wood flour, because it reinforced the polymer matrix. Generally, the efficiency of the coupling agents also depends on the method of application, the method of surface treatment and the chemical structure [8].

In order to improve the material strength on the interface between the wood flour and PVC, we used additional additives in our research. In case of PVC, usually not necessary, but also was useful to use an extra agent to increase the connection. Therefore, the surface of natural filler was treated with MDI. We experimented with pure MDI, because it can be advantage of MDI that it can be chemically bonded to the free-OH groups of cellulose and lignin as well. The tension and mobility of MDI is very low, so is does not escape from the composites. Five types of measurements were carried out:

- Density
- Hardness test (Shore D)
- Tensile test (100 mm/min)
- Impact test (Charpy method)
- Thermal Stability test (Stabilimetr method)

1. MATERIALS

The base mixtures with the required additive were: suspension PVC powder (Ongrovil S-5258), Ca–Zn based stabilizer, paraffin based internal and glycerin ester type external lubricants, $CaCO_3$ filler, acryl based processing aids and beech wood flour. To create a triple system, pure methyl diphenyl diisocyanate was used. *Table 1* shows the additive's quantity in phr (per hundred resin).

Table 1

Formulations of the PVC/Wood/MDI composites

PVC	Stabilizers	Lubricants	Processig aids	Filler	Wood flour – MDI
100	2.4	2	7	10	20

1.1. Sample preparation

First and foremost, we were carrying out the surface treatment of the wood flour. The MDI was applied 1, 2 and 5% by weight to the wood's surface for better miscibility and adhesion with the PVC. The mixtures were hot mill rolled at 170 °C for until fully homogeneous and were pressed to two different thicknesses at 175 °C. For the 4 mm thickness sheets, 5 minute at 20 bar and 5 minute at 300 bar pressures were used. While, for the 1 mm thickness specimens, 2.5 minute at 20 bar and 2.5 minute at 300 bar pressures were used. From the prepared sheets, standard sized specimens were stamped using a pneumatic punching equipment.

2. MEASUREMENT METHODS

2.1. Density and hardness tests

Based on principle of Archimedes, the density values were determined by water immersion measurement with a Mettler-Toledo digital analytical scale.

The hardness tests were carried out using a Zwick/Roell Ho.43150 type digital Shore D testing equipment. The Shore D test tools are usually used to measure harder plastics and elastomers, so it is well suitable for measuring the PVC composite samples. The tests were carried out according to ISO 868. On each specimens of four mm thickness 20 parallel measurements were made to determine the mean values and standard deviation.

2.2. Tensile and impact tests

The tensile tests were carried out using an INSTRON 5566 universal material tester according to ASTM D638-10 standard. During the tests, the stress-elongation behavior of the samples can be determined. The tests were carried out at room temperature (23 ± 1), 50% humidity and with a cross-head speed of 100 mm/min.

Impact resistance of the materials can be determined by the impact tests. The impact tests were carried out according to the Charpy method (EN ISO 179) using a CEAST 6545 instrumented pendulum equipment. The tests were done with a 2J hammer.

2.3. Thermal stability tests

The thermal stability can be determined using a Stabilometer. The device is used to examine the heat stability of PVC, PVC copolymers, blends and films, as function of time. The test can be used to determine the time, at which pre-determined color changes occur within the materials at 190 °C. The tests were carried out on a Stabilimetr WC45 measuring equipment. The material thickness was 0.4 mm.

3. RESULTS

3.1. Density and hardness tests

During the tests, the density values of various composites can be determined. The composites of MDI may have a more compact structure, which could mean that the MDI is connected both to the wood and the PVC better.

Table 2

Result of density tests of the PVC/Wood and PVC/Wood/MDI composites

Sample	**Density (g/cm^3)**
PVC/Wood	1.38 ± 0.001
PVC/Wood/MDI (1%)	1.43 ± 0.005
PVC/Wood/MDI (2%)	1.43 ± 0,001
PVC/Wood/MDI (5%)	1.42 ± 0.003

However, the results show differences between the treated and untreated samples, but only slight differences treated samples. The amount of applied MDI does only affect the density slightly.

Table 3

Results of the hardness and deviation values of the specimens

Sample	**Shore D**
PVC/Wood	80.76 ± 0.35
PVC/Wood/MDI (1%)	80.13 ± 0.45
PVC/Wood/MDI (2%)	81.01 ± 0.36
PVC/Wood/MDI (5%)	81.19 ± 0.79

The results of the hardness tests show no significant differences. In case of MDI composite the MDI did not cause material softening. If we are taking notice of the deviation values they are very close to each other.

3.2. Tensile and impact tests

The modifying effect of MDI is visible in *Table 4.* In case of 5% MDI mixtures, significant increases in the strength values were observed. *Figure 1* shows the elongation-stress curves, where it can be seen that the deformations were almost the same, the tensile strength increased by adding increased amounts of additive. For all blends, the tensile test shows significant improvement in mechanical properties.

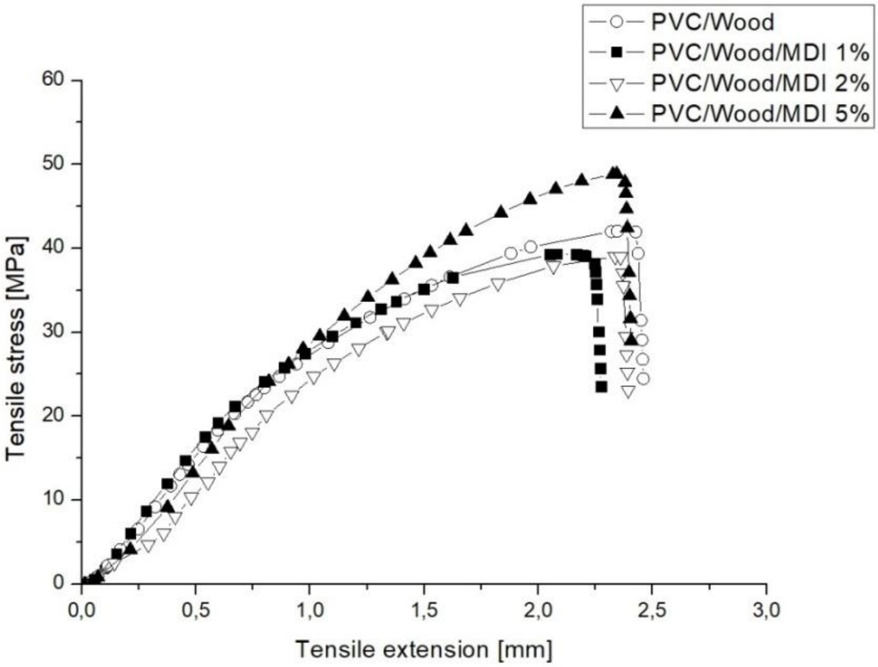

Figure 1

Stress-strain curves of PVC/Wood and PVC/Wood/MDI composites

Table 4

Result of the tensile tests at room temperature

Sample	Tensile strength (MPa)
PVC/Wood	42.05 ± 0.97
PVC/Wood/MDI (1%)	39.33 ± 0.59
PVC/Wood/MDI (2%)	39.01 ± 0.92
PVC/Wood/MDI (5%)	50.54 ± 1.02

In the impact strengths considering the deviation values only slight changes were observed. Accordingly, MDI seems to have no significant effect on the impact strength.

Table 5

Results of Charpy – impact tests

Sample	Impact strength (kJ/m^2)
PVC/Wood	2.50 ± 0.03
PVC/Wood/MDI (1%)	2.32 ± 0.27
PVC/Wood/MDI (2%)	2.44 ± 0.05
PVC/Wood/MDI (5%)	2.35 ± 0.07

3.3. Thermal stability tests

During the thermal stability tests, the samples were inserted into the measuring equipments at 190 °C. During the evaluation the sample's time scale was compared to each other. The thermal stability values were that time, when predetermined color changes occurred to the samples. The times are expressed in minutes.

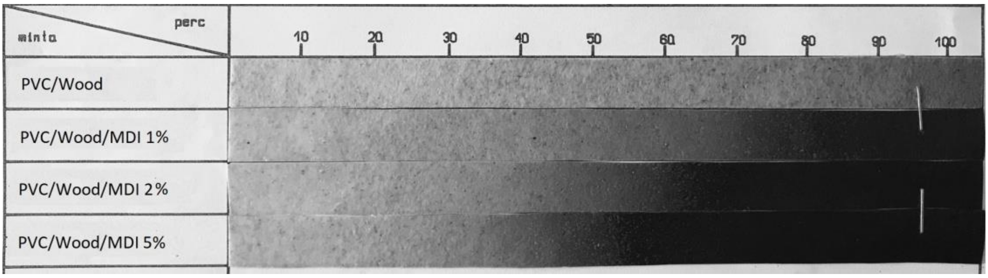

Figure 2

Result of PVC/Wood and PVC/Wood/MDI thermal stability tests

Figure 2 shows that the thermal stability of the 1% MDI composites (70 minutes) composite was becoming worse with increasing MDI content. Larger sensitivity was measured at 5% composites (35 minutes). Thus, increasing the MDI content the heat resistance of the material is reduced. This was probably caused by the reactive amide content of the urethane bond formed between the cellulose/lignin and the isocyanate which can promote the scission of the HCl, decreasing the thermal stability of PVC.

SUMMARY

In this research, four different composites were prepared and tested. Numbers of tests were carried out on the specimens to determine the properties of the developed new material structures. Based on the results of density tests, those composites which contained MDI were more compact that the other. Further tests would be needed to understand the result of the impact tests. From the results, an apparent decrease in strength is observed, probable caused by the MDI, because the MDI works as a hard segment in these composites, making them more rigid/brittle. The results of the 5% by weight MDI containing mixture provided excellent tensile strength. We will also investigate this further. Probably, due to the strong interaction between the polymer matrix and the organic filler, large parts of the load were taken over by the fibrous filler (wood flour). From the thermal stability tests, significant deterioration was observed. If we increased the dose of MDI then the thermal resistance of the composite deteriorated. This was expected, because the nitrogen content of the compounds generally has a negative effect on the PVC is thermal stability. In a continuation of the research means and methods will be sought after and tested to mitigate the MDI's detrimental effect on thermal stability without compromising the improved tensile behavior but hopefully improve on the impact resistance.

ACKNOWLEDGMENT

This research was supported by the European Union ant the Hungarian State, co-financed by the European Regional Development Fund in the framework of the GINOP – 2.3.4.-15-2016-00004 project, aimed to promote the cooperation between the higher education and the industry.

REFERENCES

[1] H. Jiang and D. P. Kamdem (2004). Development of poly(vinyl chloride)/wood composites. A literature review. *Journal of Vinyl and Additive Technology*, Vol. 10, No. 2, pp. 59–69.

[2] G. Akovali (2012). *Plastic materials: Polyvinyl chloride (PVC)*. Woodhead Publishing Limited.

[3] F. Mengeloglu and L. M. Matuana (2003). Mechanical properties of extrusion-foamed rigid PVC/wood-flour composites. *Journal of Vinyl and Additive Technology,* Vol. 9, No. 1, pp. 26–31.

[4] P. Kaushik and K. K. Jin (1989). Recent Advances in the Processing of Wood-Plastic Composites. *Journal of Chemical Information and Modeling,* Vol. 53, p. 160.

[5] A. Kositchaiyong, V. Rosarpitak, H. Hamada, and N. Sombatsompop (2014). Anti-fungal performance and mechanical-morphological properties of PVC and wood/PVC composites under UV-weathering aging and soil-burial exposure. *International Biodeterioration and Biodegradation*, Vol. 91, pp. 128–137.

[6] J. M. Pilarski and L. M. Matuana (2006). Durability of wood flour-plastic composites exposed to accelerated freeze-thaw cycling. II. High density polyethylene matrix. *Journal of Applied Polymer Science*, Vol. 100, No. 1, pp. 35–39.

[7] N. Petchwattana and S. Covavisaruch (2013). Effects of Rice Hull Particle Size and Content on the Mechanical Properties and Visual Appearance of Wood Plastic Composites Prepared from Poly(vinyl chloride). *Journal of Bionic Engineering,* Vol. 10, No. 1, pp. 110–117.

[8] B. V. Kokta, D. Maldas, C. Daneault, and P. Beland (1990). Composites of polyvinyl chloride-wood fibers. i. effect of isocyanate as a bonding agent. *Polymer-Plastics Technology and Engineering*, Vol. 29, No. 1–2, pp. 87–118.

Materials Science and Engineering, Volume 43, No. 1 (2018) pp. 98–107.

INFLUENCE OF CHAIN EXTENDER ON SOFT AND HARD SEGMENT OF POLYURETHANE ELASTOMERS

PATCHARAPON SOMDEE[1]–TÍMEA LASSÚ-KUKNYÓ–
CSABA KÓNYA–KÁLMÁN MAROSSY[2]

The goal of this study is investigation of the effect of chain extender content consisting of flexible polyurethane elastomers at 7 phr and rigid polyurethane elastomers at 34 phr on mechanical, thermal and structural properties of polyurethane elastomers (PUR). Firstly, polypropylene glycol (PPG) was solution mixed with chain extender, amine catalyst, air release additive and moisture scavenger. After that, the mixture was shear mixed with diphenylmethane-4,4'-diisocyanate (MDI). In this study, the chain extender is monoethylene glycol (EG). Mechanical properties of polyurethane elastomers were tested by Shore A/D hardness and tensile test. Thermal properties and structure were investigated by differential scanning calorimetry (DSC) and thermally stimulated discharge (TSD) method. Density was also measured in the study. Results show Shore A and D hardness increase with increasing EG content from 7 to 34 phr. Tensile strength increases when EG content is increased while elongation at break decreases at EG content of 34 phr. Density of PUR slightly increases when EG content is increased. For structure characterization, DSC thermogram clearly observed a relaxation temperature of soft segment at EG content of 7 phr. Furthermore, TSD technique was used to investigate chain relaxation of PUR as well. Results show the same soft segment glass transition temperatures for both EG content 7 and 34 phr. However, the glass transition temperature of soft segment measured by DSC is lower than that shown by the TSD technique.

Keywords: polyurethane elastomers, chain extender content, soft and hard segments

INTRODUCTION

Chain extenders play an important role in the molecular structure of polyurethane elastomers. Polyurethane elastomers without a chain extender formed by directly reacting diisocyanate and polyol generally have very poor physical properties and often do not exhibit microphase separation. Polyurethane elastomers are formed typically by three chemical constituents reacting together such as a diisocyanate, a long chain diol and a small molecule chain extender diol or a diamine.

The hard segments are built from alternating diisocyanate and chain extender sequences while the soft segments originate from the polyol [1]. The alternating of hard segment and soft segment is shown in *Figure 1*.

---

[1] Institute of Ceramics and Polymer Engineering, University of Miskolc
H-3515 Miskolc-Egyetemváros, Hungary
somdee_patch@hotmail.com

[2] Institute of Ceramics and Polymer Engineering, University of Miskolc
H-3515 Miskolc-Egyetemváros, Hungary
polkal01@uni-miskolc.hu

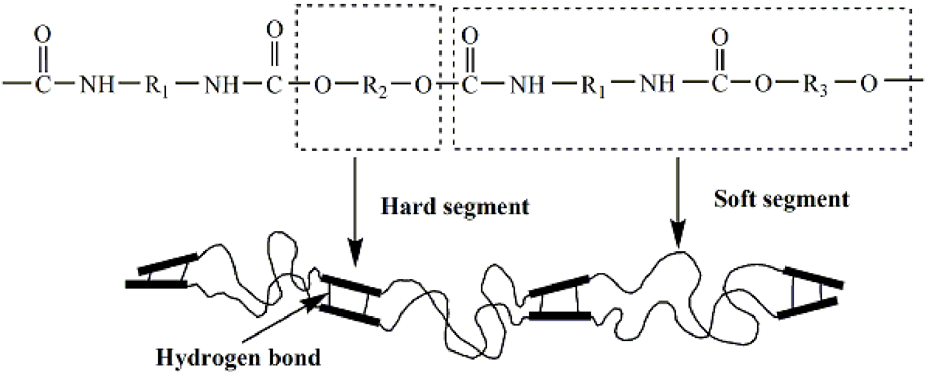

Figure 1
PUR alternating hard segment (HS) and soft segment (SS) structure

Chain extender may increase the hard segment length to allow hard segment segregation which results in good mechanical properties such as an increase in modulus and an increase in the hard segment glass transition temperature of polyurethane [1]. Chain extender can be categorized into two classes, aromatic diols or diamines and the corresponding aliphatic diols or diamines. In general, polyurethane elastomers (PUR) chains extended with an aliphatic diol produce a softer material than do their aromatic chain extended counterparts. Also, diamine chain extenders are much more reactive than diol chain extenders and give properties superior to those of similar polymers prepared with the equivalent diol chain extenders. This is due to the HS (urea linkage) which has a higher density of hydrogen bonding, which results in a higher glass transition temperature and higher thermal stability. However, polyurethane urea made from diamine chain extenders tend to be less soluble in common solvents and therefore they are more difficult to process. Moreover, another factor is electron delocalization, i.e. the aromatic chain extenders have less reactivity than aliphatic chain extenders, which can be favorable in reactions. Examples of diol chain extenders include ethylene glycol, 1,6-hexanediol (HG), 1,4-butanediol (BDO, BD or BG), diethylene glycol (DEG), diacetylene diols such as 2,4-hexadiyne-1,6-diol or 5,7-dodecadiyne-1,12-diol and some aromatic diols, triazine diols or 4,4’-(ethane-1,2-diyl) bis (benzene thiohexanol) [1]. In the case of ethylene glycol or 1,2-ethanediol glycol, it is produced from ethylene by the intermediate ethylene oxide. Ethylene oxide reacts with water to produce ethylene glycol.

Modifying the ratio between the polyol and chain extender, and polyurethane elastomers may result in a change from a hard to a rubbery elastomer. The effect of chain extender on tensile properties of polyurethane microcellular elastomers used in reaction injection moulding (RIM) technology and multivariable linear regression analysis was studied by Korodi et al. [2]. It was found that the molded density has the greatest influence on the tensile strength, so the tensile strength is increased by the ethylene glycol and rigid polyol content. All the chain extenders studied had a negative influence on the elongation at break. Barikani and Barmar [3] studied about effective structure parameters of thermoplastic polyurethane elastomers. The role of the hard segment chemical construction in physical and mechanical properties of the elastomers studied by changing the chain extenders. Dynamic mechanical analysis studies for polyester and polyether elastomers show that an elastomer with larger chain extender has a larger hard segment and better phase separation. By increasing the phase separation, good physical and mechanical properties were identified.

The effect of the ratio between the hard and soft segment content was investigated by Prisacariu and Scortanu [4]. Moreover, the effect of varying the odd-even number of CH_2 groups in regard to the chain extender was examined. The best mechanical behavior as elastomers was revealed for polyurethane with CH_2 even numbers on the chain extender when the different parts of the PUs macromolecular chains can adopt extended linear forms. Two series of polyurethane elastomers were synthesized to investigate the effect of incorporation of various new chain extenders on the mechanical and thermal properties of polyurethane elastomers. The 2,5-dimethyl-3 hexine-2,5-diol-based polyurethane displayed a relatively low glass transition temperature of –57 °C, tensile strength of 11 to 14 MPa and elongation at break of 600 to 700% [4]. Several works have studied the effect of chain extender with different methods to improve the properties of polyurethane such as the effect of the polyol and chain extender ratio or the hard and soft segment ratio. Some new work synthesized a new polyurethane based polyurethane ureas with different chain extender type and investigated their properties [5]. The effect of different types of chain extenders and their dosage on the degree of phase separation between hard and soft segments in polyurethane prepolymers was investigated [6].

From previous study, some papers focus on a small difference in chain extender content on properties of polyurethane elastomers. Therefore, the effect of a large difference in the chain extender content was investigated for wide range of polyurethane elastomer applications with a very soft polymer and a hard polymer in this study. Chain extender content of PUR was varied at 7 or 34 phr. Shore A and D hardness, tensile strength and elongation at break were measured and evaluated. Furthermore, thermal properties and structure of PUR were characterized by DSC and TSD techniques. The density of PUR with different EG content was measured.

1. MATERIALS AND METHODS

1.1. Materials

Monoethylene glycol is used as chain extender. The EG content was either 7 or 34 phr. Diphenylmethane-4,4’-diisocyanate was used for isocyanate. ONGRONAT XP 1147 is an acidified MDI blend. An average molecular weight is 266 g/mol and its equivalent weight is 127.33 g/mol. ALCUPOL D4011 is used for polyol blend. It is reactive polypropylene glycol (PPG-4000) with ethylene oxide. Its molecular weight is 4,000 g/mol. Jeffcat TD33 is used for catalyst, it is 33.3 wt.% solution of triethylene diamine in dipropylene glycol. The air release additive trade name is BYK A500. The trade name of the moisture scavenger is Finmasorb430. All ingredients of mixture A are listed in *Table 1*.

1.2. Methods

PPG polyol or soft segment, chain extender, catalyst, air release additive and moisture scavenger were prepared in mixture A. Mixture A was solution mixed with weight fraction shown in *Table 1*. All ingredients were homogenized for 10 to 15 min at 35% of a shear mixing machine that has 6,000 rpm capacity. After that, mixture A was shear mixed for 8 to 12 sec at 1,000 rpm with MDI by shear mixing machine. Then, it was poured into a warm mold of 70 °C and left for 30 min in order to prepare polyurethane elastomer samples. The cured sample sheets were stored at least four days at room temperature before testing. Mechanical properties were tested such as Shore A hardness for soft material and Shore D for hard material following ISO 868. Tensile properties were measured according to ISO 527 1A. Structure of polyurethane elastomers was characterized by DSC technique performed on METTER TOLEDO model DSC823e with heating rate of 10 °C/min from –100 to 250 °C. Thermally stimulated discharge technique was used to examine the glass transition of polyurethane elastomers. PUR sheet of 1 mm thickness was cut by die cutting of 26 mm diameter and thin gold electrode deposited by sputter coater. Polarizing field was 500 V/mm and temperature in the range of –120 to 10°C. Heating and cooling rates were 5 °C/min. Moreover, the density of polyurethane elastomers was measured by calculation of the difference in weight between dry and wet.

Table 1

Ingredients of mixture A

Description	**Trade Name**	**Weight (phr[*])**
Polypropylene glycol copolymer (PPG)	ALCUPOL D4011	100
Monoethylene glycol	EG	7 or 34
Amine catalyst	Jeffcat TD33	0.3
Air release additive	BYKA500	0.3
Moisture scavenger	Finmasorb 430	10

[*] phr is parts per hundred resin

2. RESULTS AND DISCUSSIONS

The chain extender content of 7 and 34 phr were used to prepare the experimental PUR that consist of flexible and other one for rigid PUR, respectively. Mechanical properties such as Shore A hardness, Shore D and tensile properties of both flexible and rigid polyurethane elastomers were tested. The variation of Shore A and D hardness values with different EG content are shown in *Figure 2*. Both Shore A and D hardness increase with increasing EG content from 7 to 34 phr. Shore A hardness increases from 55.2 to 96.3 while Shore D hardness increases from 13.6 to 58.8. Both Shore A and D hardness have higher effectiveness at 1.7 and 4.3 times, respectively, than when compared to EG content of 7 phr. This is due to increasing the hard segment content, which will also increase the hydrogen bonding index. If hydrogen bond is formed only within the hard segment, it may enhance crystallization and phase separation of the PUR structure [7].

The tensile strength of polyurethanes is dependent on the resistance of the cross-linking bonds being either covalent or hydrogen bonds in order to prevent the chains from slipping completely and the material yielding. The harder the material, the dense the cross-linking. When operating below the ultimate tensile strength, the harder materials retain their elastic properties and do not behave like a thermoset. Under long term tension, polyurethanes will suffer from creep (strain relaxation). Fully post cured polyurethanes will lose both tensile and modulus properties when heated in the short term to temperatures above ambient and below their breakdown points [8]. The tensile strength of PUR increases with changing EG content from 7 to 34 phr. Tensile strength increases from 4 to 24 N/mm^2 when EG content is increased to 34 phr. It was enhanced around 6 times when compared to EG content of 7 phr. On the other hand, elongation at break decreases with increasing EG content as shown in *Table 2*. Result shows elongation at break was decreased from 255 to 28% with increasing EG content of 34 phr.

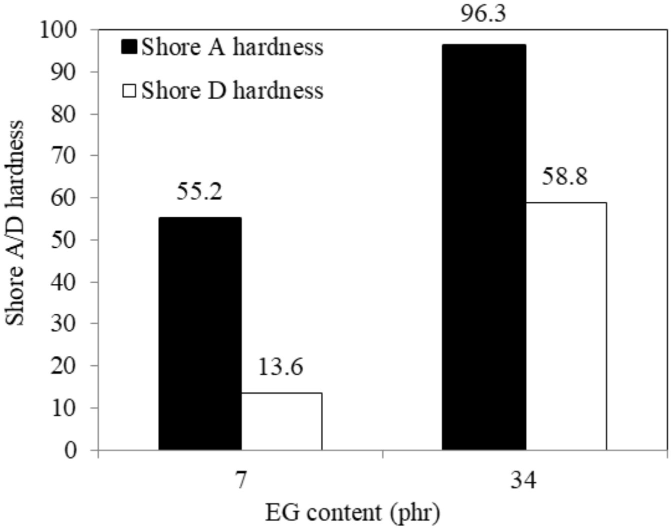

Figure 2
Shore A and D hardness of polyurethane elastomers with EG content of 7 and 34 phr

The influence of monoethylene glycol which is a chain extender in PUR leads to formation of phase separated hard segments and affects properties of PUR. Thus, the hard segment concentration leads to high phase separation and increasing tensile strength as well. This is in accordance with the widely accepted idea that the hard segment domains act as a reinforcing particle in the soft segment matrix. The effect of chain extender on the density of polyurethane elastomer is shown in *Table 2*. Results show the density increases when increasing the EG content.

Table 2
Tensile strength, elongation at break and density of polyurethane elastomers at EG content of 7 or 34 phr

EG content (phr)	Tensile strength (N/mm^2)	Elongation at break (%)	Density (g/cm^3)
7	4 ± 0.07	255 ± 9	1.084 ± 0.00
34	24 ± 0.40	28 ± 7	1.184 ± 0.01

DSC thermograms from the first heating scans of polyurethane elastomers at EG content of 7 and 34 are shown in *Figure 3*. In the case of flexible PUR at EG content of 7 phr, a small transition is clearly observed at around –62 °C that is the glass transition temperature of the soft segment in PUR. In contrast, the soft segment relaxation temperature at EG content of 34 phr was not clearly observed. This is due to the cross-linking of the hard segment obstructing the PPG polyol chain motion, so the transition temperature was not clearly exhibited when increasing EG content to 34 phr. The broader endotherms peak at EG content of 7 phr a small degree of ordering in hard segment domains. In the case of EG content 34 phr, the endotherms peak is narrower than of the soft PUR, which may be due to it being highly hard segment cross-linked compared to EG content of 7 phr EG content. However, hard segment glass transition temperature could not be observed in either flexible or rigid PUR. This is probably due to it having a low fraction of amorphous phase.

The thermally stimulated discharge technique can confirm the glass transition temperature results of PUR, as shown in *Figure 4*. The curves of both flexible and rigid polyurethane elastomer show the same glass transition temperature of the soft segment around –65 °C. Furthermore, the intensity peak of rigid PUR can be related to a small relaxation in the DSC thermogram, which is difficult to evaluate, as shown in *Figure 3(b)*. It can be indicated that this originates from the polyol and also can prove that the hard and soft segments in polyurethane elastomer are an incompatible mixture.

Figure 5 shows the first derivative of flexible polyurethane elastomers at EG content of 7 phr. The primary curve is the derivative with respect to temperature of the original DSC curve and is generally computed electronically. The first derivative curve of a glass transition gives a peak which area is proportional to the value of ΔC_p. Peak temperature of the first derivative can be used as a measure of change in glass transition temperature. The first derivative curve exhibited the lowest peak at –72 °C. This can indicate that the glass transition temperature of the soft segment is around –72 °C. A small peak that drops to base line on the first derivative exhibited crystallization temperature before relaxation of the soft segment in polyurethane elastomer.

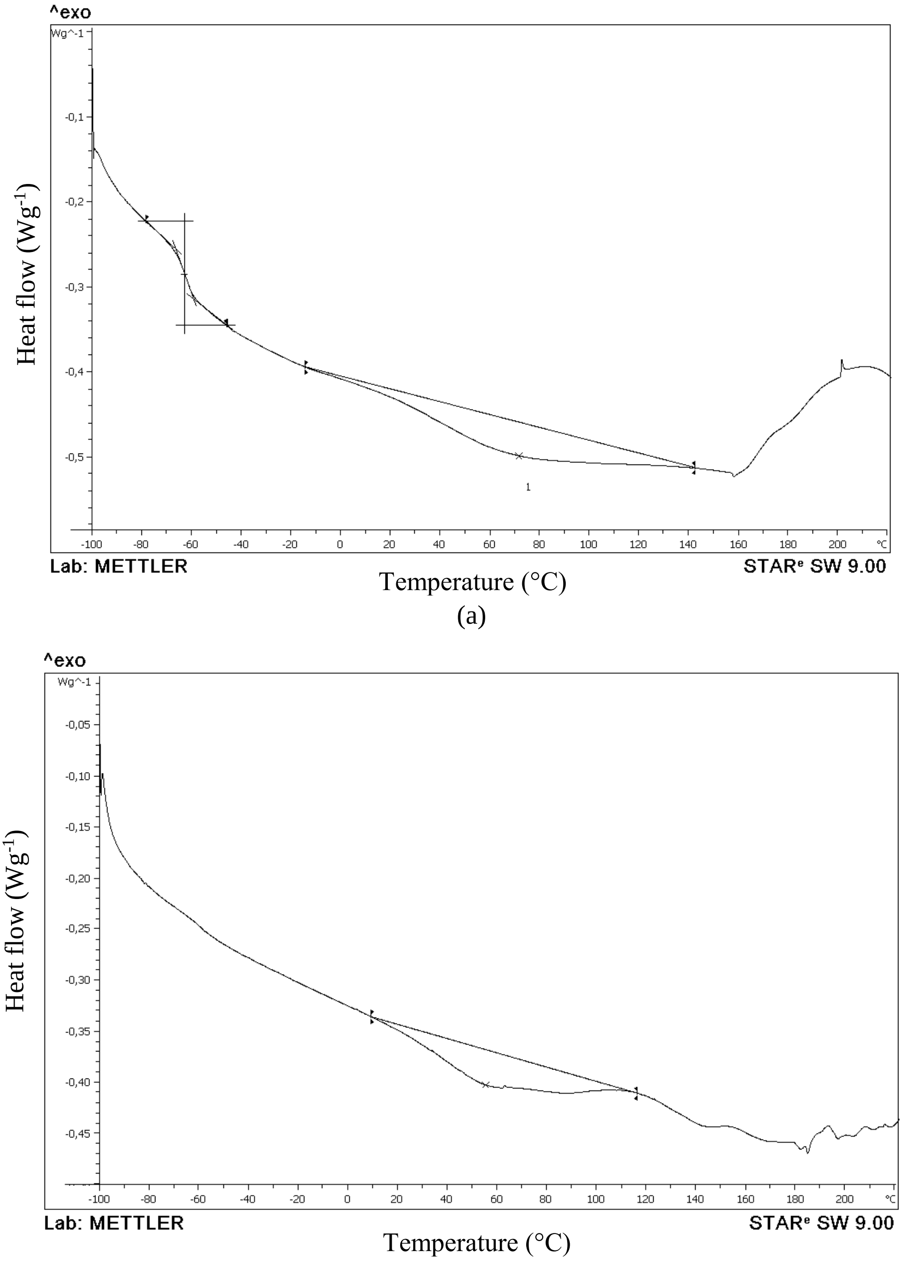

(a)

(b)

Figure 3

DSC thermograms of polyurethane elastomers at EG content of 7 (a) and 34 (b) phr

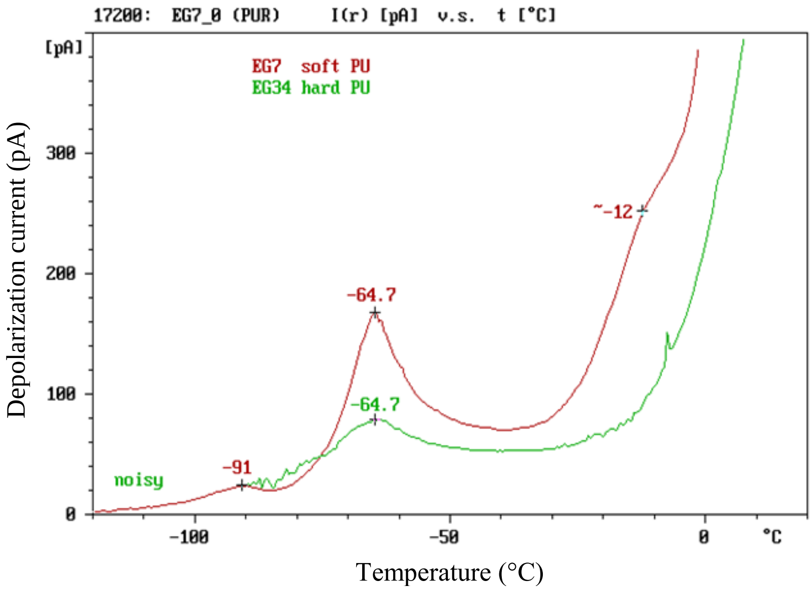

Figure 4

TSD thermograms of polyurethane elastomers at EG content of 7 and 34 phr

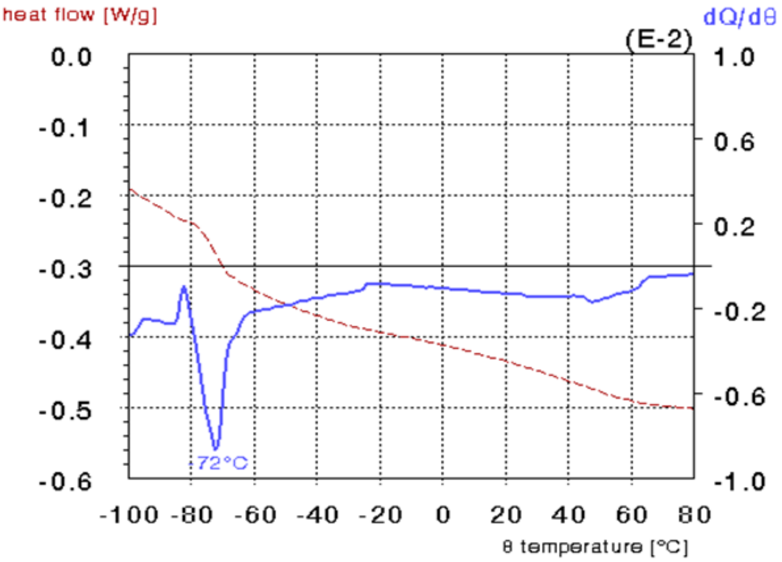

Figure 5

DSC curve of polyurethane elastomer at EG content of 7 phr (dashed line) and it's first derivative (solid line)

CONCLUSIONS

Flexible and rigid polyurethane elastomers matrix were produced with varying chain extender content of 7 and 34 phr. In case of mechanical properties, Shore A and D hardness increased when EG content was increased from 7 to 34 phr. It can be enhanced 1.7 and 4.3 times, respectively, when compared to the EG content of 7 phr. In the same way, tensile strength increases around 6 times, from 4 and 24 N/mm^2, showing that the higher EG content of the chain extender has significantly affected the mechanical properties. These results indicate that higher chain extender content reacts more strongly with the MDI part and can become a longer hard segment in PUR structure. Moreover, the mechanical property results are also related to increasing of density of PUR. Flexible polyurethane elastomers became rigid polyurethanes when chain extender content was increased up to 34 phr. Therefore, elongation at break decreased from 255 to 28%. In the case of thermal and structural properties, the glass transition temperature of soft segment in PUR was observed by DSC and TSD techniques to be –62 °C and –65 °C, respectively. It was difficult to observe transition temperatures from the DSC thermogram at EG content of 34 phr. This might be due to the higher EG content affecting polyol chain motion in the PUR structure. Glass transition temperature measured by the DSC method had higher values than when measured by TSD, which may have been caused by different evaluation algorithms. However, the glass transition temperature of the hard segment can be proved by the TSD method.

ACKNOWLEDGMENTS

This research was supported by the European Union and Hungarian State, co-financed by the European Regional Development Fund in the framework of the GINOP-2.3.4-15-2016-00004 project, aimed to promote the cooperation between the higher education and the industry. The research was also supported by the Institute of Ceramics and Polymer Engineering, University of Miskolc and BorsodChem Zrt. Company.

REFERENCES

[1] C. Prisacariu (2011). *Polyurethane Elastomers: From Morphology to Mechanical Aspects.* Springer Wien–NewYork.

[2] T. Korodi, N. Marcu and AI. Tirnaveanu (1984). Polyurethane microcellular elastomers: 2. Effect of chain extender on the mechanical properties. *Polymer,* Vol. 25, pp. 1211–1213, Aug. 1984.

[3] M. Barikani and M. Barmar (1996). Thermoplastic polyurethane elastomers: Synthesis, and study of effective structural Parameters. *Iranian Polymer Journal,* Vol. 5, No. 4, pp. 231–235, Oct 1996.

[4] C. Prisacariu and E. Scortanu (2011). Influence of the type of chain extender and urethane group content on the mechanical properties of polyurethane elastomers with flexible hard segments. *High Performance Polymers,* pp. 308–313, May 2011.

[5] A. E. Kalajahi, M. Rezaei, F. Abbasi and G. M. M. Sadeghi (2017). The effect of chain extender type on the physical, mechanical and shape memory properties of poly (ε-caprolactone)-based polyurethane-ureas. *Polymer-Plastics Technology and Engineering,* Vol. 56, No. 18, pp. 1977–1985, Apr 2017.

[6] C. Tan, T. Tirri and C-E. Wilen (2017). Investigation on the influence of chain extenders on the performance of one-component moisture-curable polyurethane adhesives. *Polymers*, Vol. 9, 184, pp. 1–19, May 2017.

[7] M. M. Zamzam (2005). A study on thermal degradation resistance of thermoplastic polyurethane coatings. Master dissertation, Dept. of Chem., United Arab Emirates University.

[8] I. R. Clemitson (2008). *Castable Polyurethane Elastomers*. CRC Press Taylor & Francis Group.

Materials Science and Engineering, Volume 43, No. 1 (2018) pp.108–116.

MODEL AIDED BIOFUEL DESIGN: A CASE STUDY OF $C_6H_{12}O$

YILEI XUE[1, 2, 3]–ZSÓFIA BORBÁLA RÓZSA[2, 4]–ANDREA GULJAS[2, 3]–
BÉLA FISER[2, 4, 5]–ANITA RÁGYANSZKI[2, 3, 4]–JOHN JUSTINE VILLAR[2, 6]–
BÉLA VISKOLCZ[2, 4]–IMRE G. CSIZMADIA[2, 3]–MILÁN SZŐRI[2, 4]

The aim of this project is to find the most promising $C_6H_{12}O$ molecular entities for use as a biofuel. To design such structures in a heuristic manner, gas-phase thermodynamic properties of all singlet $C_6H_{12}O$ isomers (211 species) were calculated using G3MP2B3 *ab initio* composite method. For each isomer, the G3MP2B3 standard enthalpy of formation ($\Delta_{f,298.15K}H^{\circ}_{calc}$), higher heating value (HHV), as well as relative molar Gibbs free energy (ΔG), standard molar entropy *(S)* was computed, and it was found that the computed $\Delta_{f,298.15K}H^{\circ}_{calc}$ reproduced the corresponding literature values – available only in case of 11 species – by average absolute deviation of 3.3 kJ/mol, so it can be assumed that this uncertainty can be used for the recommended $\Delta_{f,298.15K}H^{\circ}$ values for the remaining molecular entities as well. These $C_6H_{12}O$ isomers were structurally categorized into 13 subgroups according to their backbone features and functional groups. Amongst these structures, ethers have the highest HHV from which 3-ethyl tetrahydrofuran (38.3 MJ/kg) is a potential biofuel component however production from lignocellulose biomass is not yet reported and its other fuel properties has to be waited for characterization. When LD_{50} values were available, health risks of these compounds were also analyzed.

Keywords: ab initio, thermodynamic properties, thermodynamic map

INTRODUCTION

An ideal biofuel is environmentally friendly, easily storable, renewable, sustainable, and a widely available chemical compound with high energy density, which can be generated from inexpensive and abundant sources. It is even better if the fuel is an important intermediate for chemical industry at the same time, making the compound multifunctional. The first-generation (1G) of biofuels are made from food crops and are currently the major sources of biofuels despite their low energy density and conflict with food supply [1]. Second-generation (2G) biofuels overcame the latter issue since these are produced from sustainable feedstock such as cellulose, but their production requires several physical and chemical processes [1]. However, using algae as an energy source can keep the third-generation (3G) biofuel production relatively simple [2]. Further improvement – the fourth-generation (4G) technology – is a combination of genomically synthesized microbes (synthetized to efficiently produce fuels) and genetically

---

[1] Department of Physical and Environmental Sciences, University of Toronto Scarborough, Canada

[2] Institute of Chemistry, University of Miskolc, Miskolc, Hungary
e-mail: milan.szori@uni-miskolc.hu

[3] Department of Chemistry, University of Toronto, Canada

[4] Higher Education Industry Cooperation Centre, University of Miskolc, Miskolc, Hungary

[5] Ferenc Rákóczi II. Transcarpathian Hungarian Institute, Beregszász, Transcarpathia, Ukraine

[6] Scientific Computing Laboratory, Department of Computer Science, University of the Philippines Diliman, Philippines

optimized feedstocks (designed to capture large amounts of carbon). This may render 4G biofuels a carbon neutral source of fuel [3]. An optimum molecule for such biofuel can be difficult to select even with retrosynthetic approach, although some empirical rules are already available. For instance, it is known that increasing hydrogen content leads to lower carbon dioxide footprint and higher oxygen content decreases smoke emission [4], although it also leads to smaller carbon and hydrogen content which in turn lowers the heating value [5]. For example, one of the $C_6H_{12}O$ isomers, 2,5-dimethyltetrahydrofuran (2,5-DMTHF), is already recommended as a biofuel component [6]. It has a relatively high energy density (LHV = 35.2 MJ/kg and HHV = 37.8 MJ/kg), low volatility (T_b = 101.5 °C), low viscosity (0.8 mm^2/s), and it is immiscible with water [7]. Furthermore, it can be manufactured by a one-step transformation of biomass-derived carbohydrates and raw lignocellulose with reasonable yields at mild conditions in water [8]. Therefore, a chemical formula, like $C_6H_{12}O$, with high degree of saturation and moderate oxygen content is promising, but 2,5-DMTHF is probably not the optimum structure amongst $C_6H_{12}O$ isomers. Other oxygenated hydrocarbons including alcohol, methyl ester and cyclic ethers can also be generated from cellulosic feedstocks [4].

In this research, an effort has been made to find better candidates described by the same chemical formula as 2,5-DMTHF, using data collection and *ab initio* prediction of thermodynamic properties for all $C_6H_{12}O$ isomers.

COMPUTATIONAL METHODS

The enumeration of organic molecules corresponding to a given stoichiometry can be deduced to graph theory, if nuclei and chemical bonds are considered as the nodes and the edges of a graph [9]. A certain number of atoms with a limited amount of different valences define the number of constitutional isomers. In this work, all possible stochiometric isomers of $C_6H_{12}O$ were generated, allowing hydrogen, carbon and oxygen to form 1, 4 and 2 chemical bonds, respectively. This low dimensional representation is extended into three dimensions by means of the atom-type-specific geometric parameter set obtained from the simplified MM2 force field [10]. By using this procedure, a number of 211 three dimensional molecular configurations were generated by Molgen 5.0 [11]. These structures served as initial structures in the search for local minima on the multidimensional potential energy surface for the species.

All quantum chemical calculations in this work were carried out using G3MP2B3 composite methods [12] as implemented in Gaussian 09 program package [13]. As part of this method, B3LYP/6-31G(d) level of theory was used for geometry optimizations and vibrational frequency calculations. The maximum optimization step size was limited to 0.01 Bohr or radians and the number of optimization steps were restricted to 300, while harmonic wavenumbers were scaled by factor of 0.96 for calculating thermodynamic properties such as standard enthalpy of formation [$\Delta_{f,298.15K}H°_{calc}(g)$], relative standard molar Gibbs free energy ($\Delta_rG°$) and standard molar entropy ($S°$). Only structures with no imaginary harmonic frequencies were further analyzed (otherwise the structure would have been re-optimized until it became a real minimum). To obtain more accurate standard enthalpy of formation [$\Delta_{f,298.15K}H°(g)$] and relative Gibbs free energy ($\Delta_rG°$) at P = 1 atm and T = 298.15 K, further single point calculations were carried out using QCISD(T)/6-31G(d) including MP2/6-31G(d) and MP2/GTMP2 levels of theories according to the G3MP2B3 protocol. Standard enthalpy of formation, $\Delta_{f,298.15K}H°(g)$, was obtained using the atomization scheme. When available, calculated $\Delta_{f,298.15K}H°(g)$ values were compared with literature ones ($\Delta_{f,298.15K}H°_{lit}(g)$). Literature data was mostly collected from Ruscic's active thermochemistry tables [14] and Burcat's thermochemistry database [15].

Finally, the higher heating value (HHV, also known as gross calorific value or gross energy) of each species was calculated either in MJ/kg or GJ/m^3 (when mass density was available in the literature). HHV is defined as the amount of heat released once the 1 mol species burned to CO_2 and H_2O and the gas phase products returned to a reference temperature (298.15 K). When the lower heating value (LHV, also known as net calorific value) is determined, gas-phase standard enthalpy of formation $\Delta_{f,298.15K}H°[H_2O(g)]$ is replaced by liquid-phase standard enthalpy of formation $\Delta_{f,298.15K}H°[H_2O(l)]$.

RESULTS AND DISCUSSION

1.1. Validation of the standard enthalpy of formation computed using G3MP2B3 composite method

To the best of our knowledge, only 11 $C_6H_{12}O$ isomers has previously published standard enthalpy of formation values from the existing 211 isomers. Available data was compared with the computed G3MP2B3 results and absolute deviation (AD) is presenteid in *Table 1.*

Table 1

G3MP2B3 calculated [$\Delta_{f,298.15K}H°_{calc}(g)$] and literature values [$\Delta_{f,298.15K}H°_{lit}(g)$] of standard enthalpy of formation for the $C_6H_{12}O$ isomers. Absolute deviation (AD) of the G3MP2B3 results from the literature are also presented

Species	$\Delta_{f,298.15K}H°_{calc}(g)$ (kJ/mol)	$\Delta_{f,298.15K}H°_{lit}(g)$ (kJ/mol)	Ref.	AD (kJ/mol)
Cyclohexanol	–261.0	–293.1	[15]	32.1
Oxepane	–220.5	–224.5	[15]	4.0
2,5-DMTHF	–262.1	–262.4	[15]	0.3
Hexan-2-one	–275.6	–279.80 ± 1.1	[14]	4.2
3-Hexanone	–273.0	–278.25 ± 0.89	[14]	5.25
3,3-Dimethyl-2-butanone	–290.7	–290.67 ± 0.88	[14]	0.03
4-Methyl-2-pentanone	–286.0	–291.2 ± 1.4	[16]	5.2
3-Methyl-2-pentanone	–279.5	–284.1 ± 1.3	[16]	4.6
2-Methyl-3-pentanone	–283.1	–286.1 ± 0.9	[17]	3.0
1-(Vinyloxy) butane	–173.0	–179.2 ± 1.2	[18]	6.2
1-Methylcyclopentan-1-ol	–283.6	–284.3 ± 1.4	[19]	0.7

Literature values for cyclohexanol, oxepane, and 2,5-DMTHF were obtained from Burcat's Thermodynamic Table [15], which were calculated using G3B3 composite method (G3B3 is technically quite similar to G3MP2B3). While the absolute deviations in the case of oxepane and 2,5-DMTHF are within the uncertainty of these methods (approx. 8 kJ/mol according to [12]), the values for cyclohexanol deviated significantly. A possible reason for this deviation can be that different cyclohexanol conformers were used for our calculations and the literature data. The remaining eight literature values are from calorimetric measurements: rotating bomb calorimetry method was used for 1-(vinyloxy) butane, and static bomb calorimetry method was used for the rest seven isomers. The maximum deviation between the computed and measured results is 6.2 kJ/mol. For the case of 1-(vinyloxy) butane the standard enthalpy of formation for 3,3-dimethyl-2-butanone shows almost a perfect match (absolute deviation is 0.03 kJ/mol). For these $C_6H_{12}O$ isomers, the computed enthalpies of formation reproduced the corresponding literature values by an average absolute deviation of 3.3 kJ/mol.

1.2. Analysis of the relationship between structure and thermodynamic properties

Backbones and functional groups of the obtained molecules had been investigated to understand the role of structural features defining the maximum reversible work that may be performed by the $C_6H_{12}O$ isomers at standard isothermal-isobaric condition (ΔG). According to backbone structure, $C_6H_{12}O$ isomers were divided into two main groups: an acyclic (indicated by unfilled symbols in *Figure 1*) and a cyclic group (indicated by filled symbols in *Figure 1*).

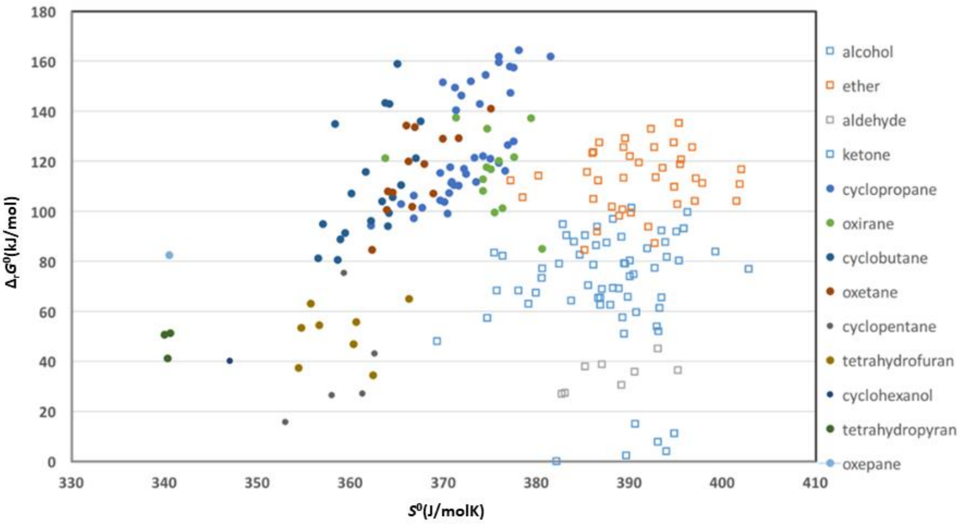

Figure 1

Thermodynamic map of the $C_6H_{12}O$ isomers based on their relative molar Gibbs free energy ($\Delta_r G$) and standard molar entropy (S)

The two groups were further classified: acyclic isomers were classified by their functional groups into four families: alcohols, ethers, aldehydes, and ketones; cyclic isomers into: cyclopropane, oxirane, cyclobutane, oxetane, cyclopentane, tetrahydrofuran, tetrahydropyran family, and cyclohexanol and oxepane as separate groups. Their relative molar Gibbs free energy ($\Delta_r G°$) and entropy contents ($S°$) can be mapped out as shown in *Figure 1*. *Figure 1* shows that acyclic structures have a higher entropy content than cyclic structures. Five- and six-membered ring structures such as oxepane and tetrahydrofurans have an extremely low entropy content compared to other $C_6H_{12}O$ isomers. The higher the relative Gibbs free energy and molar entropy, the smaller the ring size. It is also interesting to note that the Gibbs free energy content of the alkyl ethers is comparable to the molecules having strong ring-strain such as cyclopropanes, oxiranes, and oxetane. The Gibbs free energy content of the ketones is somewhat lower than ethers, while that of aldehydes is about the average of the ketones.

1.3. Higher heating values (HHV) as a function of the molecular structure motif

Similar to the case of the molar Gibbs free energy content, the cyclopropane family has the highest HHV value with a range between 38.7 MJ/kg and 39.4 MJ/kg as seen in *Figure 2*. Again, oxirane, oxetane, and acyclic ether families are the second highest subgroups of the average HHV with 38.9 MJ/kg (significantly above that of 2,5-DMTHF). From each molecular family, an isomer with the highest HHV was selected as representative and listed in the *Table 2*.

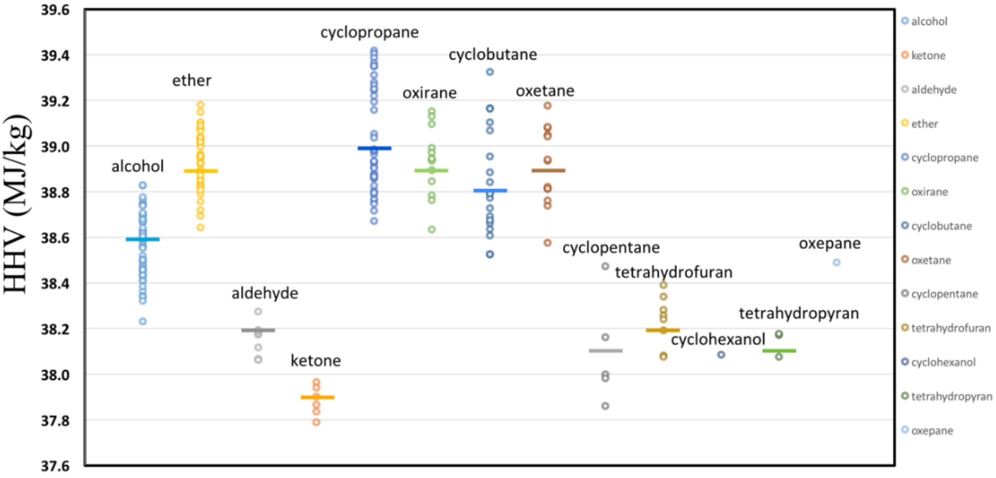

Figure 2

Calculated HHV values grouped by molecule families of the $C_6H_{12}O$ isomers

Table 2

$C_6H_{12}O$ isomers with highest HHV values from the 13 molecular families (classified by functional group). HHV are obtained from G3MP2B3 standard enthalpy of formation. Density (ρ), melting (T_m), boiling (T_b), flash point (T_{flash}), and median lethal dose, LD_{50} were collected from Ref. 19 and 20. The abbreviation n.a. stands for 'not available'

Family	**Species**	**ρ**	**HHV**	**T_m**	**T_b**	**T_{flash}**	**LD_{50}**
		g/cm^3	**MJ/kg (GJ/m^3)**	**°C**			**mg/kg**
Alcohol	5-hexen-1-ol	0.850	38.8 (33.0)	<–20	128	24.0	n.a.
Ether	5-methoxypent-1-ene	0.792	39.2 (31.0)	–112	89.9	6.90	n.a.
Aldehyde	n-hexanal	0.814	38.3 (31.2)	–49.0	131	32	4,890
Ketone	hexan-3-one	0.822	38.0 (31.2)	–55.2	121	35.0	2,901
Cyclopropane	2-methoxyethyl cyclopropane	0.910	39.4 (35.9)	–70.2	113	21.9	n.a.
Oxirane	2-butyloxirane	n.a.	39.2	–72	117.1 ± 8.0	21.8 ± 21.9	n.a.
Cyclobutane	(methoxymethyl)cyclo-butane	n.a.	39.3	–80	97	n.a.	n.a.
Oxetane	3-propyloxetane	n.a.	39.2	–75	117.1 ± 8.0	21.8 ± 21.9	n.a.
Cyclopentane	cyclopentyl methyl ether (CPME)	0.863	38.5 (33.2)	–63.3	110	16.8	200
Tetrahydrofuran	3-ethyl tetrahydrofuran (3-ETHF)	0.890	38.4 (34.2)	–63.8	113	14.8	n.a.
Cyclohexanol	cyclohexanol	0.948	38.1 (36.1)	23.0	161	62.6	1,400
Tetrahydropyran	3-methyltetrahydro-2H-pyran	n.a.	38.2	–82.3	110	79.8 ± 15.9	n.a.
Oxepane	oxepane	0.871	38.5 (33.5)	–44.6	119	21.9	n.a.

The highest HHV belongs to 2-methoxyethyl cyclopropane with a value of 39.4 MJ/kg, which is relatively close to that of the fossil-based diesel (44.8 MJ/kg). Usually the energy density of a biofuel is significantly lower than the fossil counterparts (see HHV = 22.7 MJ/kg for ethanol). The situation is even better if one compares the higher heating values per unit volume for 2-methoxyethyl cyclopropane (35.9 GJ/m^3) and diesel (39 GJ/m^3). Although the HHV of cyclohexanol in MJ/kg is not outstanding (38.1 MJ/kg) amongst the $C_6H_{12}O$ isomers, its HHV in GJ/m^3 is one of the highest in this study, since it is solid in ambient conditions. Kumar et al. [20] investigated cyclohexanol as a fuel additive and found that it increases ignition delay and heat release rates during the premixed combustion phase of diesel engine. From an emissions standpoint, the increasing cyclohexanol content reduces smoke opacity (up to 32.3%) but increases NO_x significantly. It should also be mentioned that its toxicity is moderate as indicated by median lethal dose in *Table 2* [LD_{50}(cyclohexanol) = 1400 mg/kg oral for rats]. Therefore, it can be a potential liquid fuel additive. The 3-ethyl tetrahydrofuran (3-ETHF) is the next largest HHV (38.4 MJ/kg and 34.2 GJ/m^3), however it is just slightly denser in energy than 2-ethyl tetrahydrofuran (2-ETHF, 38.3 MJ/kg). 2-ETHF can be prepared from lignocellulose sources in a two-step pathway *via* the reduction of 2-acetylfuran where the yield of the first and second step are 99% and maximum 80%, respectively [23], while such an established synthetic route is not yet reported for 3-ETHF. There is also no reported health risk of 3-ETHF yet. Beside toxicity, several other properties must also be considered, for instance, the melting point (T_m) and boiling point (T_b) are essential to ensure the fuels can be stored safety in liquid phase: $T_m < -20$ °C, 60 °C $< T_b <$ 120 °C for spark-ignition (SI) engine and 60 °C $< T_b <$ 250 °C for compression-ignition (CI) engine [7].

For the species shown in *Table 2*, T_m seems to not be a serious constrain. However, for 5-hexen-1-ol, n-hexanal, hexan-3-one, and cyclohexanol, the boiling point is reached over the limit of 120 °C used for SI engine. Moreover, flash point (T_{flash}) is also crucial to the fuel storage [24] and to avoid unwanted fuel ignition, the flash point must be between 52 °C and 96 °C for CI engine, while a low T_{flash} is desired for SI engine (and high autoignition temperature). Species in *Table 2* are out of the range for the T_{flash} of the CI engine, except cyclohexanol and 3-methyltetrahydro-2H-pyran, therefore their potential use is limited to SI engines. Based on their LD_{50} value these species are moderately toxic.

CONCLUSION

In this work, we intended to design a better $C_6H_{12}O$ biofuel component than 2,5-DMTHF. To achieve this, G3MP2B3 standard enthalpy of formation ($\Delta_{f,298.15K}H°_{calc}$), HHV, relative Gibbs free energy and entropy values were computed for all the possible $C_6H_{12}O$ isomers. The computed G3MP2B3 enthalpies of formation reproduced the available literature values within an average absolute deviation of 3.3 kJ/mol demonstrating the reliability of G3MP2B3 methodology. Amongst $C_6H_{12}O$ structures, ethers have the highest HHV values from which 3-ethyl tetrahydrofuran (3-ETHF) can be a promising structure for a biofuel component for an SI engine, and it can be produced from lignocellulose biomass. Cyclohexanol was found to be a potential biofuel additive as it has high energy density. Health risks of these molecules were also analyzed, and they were found to be moderately toxic.

ACKNOWLEDGEMENT

We acknowledge KIFÜ for awarding us access to resource based in Hungary at Szeged. Authors also thanked Máté Labádi and Dávid Vincze for the administration of the Herkules computing cluster at University of Miskolc also used in this work. This research was supported by the European Union and the Hungarian State, co-financed by the European Regional Development Fund in the framework of the GINOP-2.3.4-15-2016-00004 project, aimed to promote the cooperation between the higher education and the industry. Milán Szőri is grateful for the financial support by the János Bolyai Research Scholarship of the Hungarian Academy of Sciences (BO/00113/15/7), and the New National Excellence Program of the Ministry of Human Capacities (ÚNKP-17-4-III-ME/26).

REFERENCES

[1] A. Mohr, and S. Raman (2013). Lessons from first generation biofuels and implications for the sustainability appraisal of second generation biofuels. *Energy Policy*, Vol. 63, pp. 114–122.

[2] Y. Chisti (2007). Biodiesel from microalgae. *Biotechnology Advances*, Vol. 25, pp. 294–306.

[3] E-M. Aro (2016). From first generation biofuels to advanced solar biofuels. *Ambio*, Vol. 45 (Suppl. 1) pp. S24–S31.

[4] L. S. Tran, B. Sirjean, P. A. Glaude, R. Fournet, and F. Battin-Leclerc (2012). Progress in detailed kinetic modeling of the combustion of oxygenated components of biofuels. *Energy*, Vol. 43, pp. 4–18.

[5] Y. Demirel (2012). Energy: Production, Conversion, Storage, Conservation, and Coupling. *Green Energy and Technology*, Vol. 69, Springer.

[6] J. M. Simmie (2012). Kinetics and Thermochemistry of 2,5-Dimethyltetrahydrofuran and Related Oxolanes: Next Next-Generation Biofuels. *J. Phys. Chem. A.*, Vol. 116, pp. 4528−4538.

[7] M. Dahmen, and W. Marquardt (2016). Model-Based Design of Tailor-Made Biofuels. *Energy Fuels*, Vol. 30, pp. 1109–1134.

[8] W. Yang, A. and Sen (2010). One-step catalytic transformation of carbohydrates and cellulosic biomass to 2,5-dimethyltetrahydrofuran for liquid fuels. *ChemSusChem*, Vol. 3, pp. 597–603.

[9] M. Szőri, B. Jójárt, R. Izsák, K. Szőri, I. G. Csizmadia, and B. Viskolcz (2011). Chemical evolution of biomolecule building blocks. Can thermodynamics explain the accumulation of glycine in the prebiotic ocean? *Phys. Chem. Chem. Phys.*, Vol. 13, pp. 7449–7458.

[10] N. L. Allinger (1977). MM2. A hydrocarbon force field utilizing V1 and V2 torsional terms. *J. Am. Chem. Soc.*, Vol. 99, pp. 8127–8134.

[11] C. Benecke, T. Gruner, A. Kerber, R. Laue, and T. Wieland (1997). MOLecular structure GENeration with MOLGEN, new features and future developments. *Fresenius J. Anal. Chem.*, Vol. 359, pp. 23–32.

[12] A. G. Baboul, L. A. Curtiss, P. C. Redfern, and K. Raghavachari (1999). Gaussian-3 theory using density functional geometries and zero-point energies. *J. Chem. Phys.*, Vol. 110, pp. 7650–7657.

[13] *Gaussian 09, Revision A.02*. M. J. Frisch, G. W. Trucks, H. B. Schlegel, G. E. Scuseria, M. A. Robb, J. R. Cheeseman, G. Scalmani, V. Barone, G. A. Petersson, H. Nakatsuji, X. Li, M. Caricato, A. Marenich, J. Bloino, B. G. Janesko, R. Gomperts, B. Mennucci, H. P. Hratchian, J. V. Ortiz, A. F. Izmaylov, J. L. Sonnenberg, D. Williams-Young, F. Ding, F. Lipparini, F. Egidi, J. Goings, B. Peng, A. Petrone, T. Henderson, D. Ranasinghe, V. G. Zakrzewski, J. Gao, N. Rega, G. Zheng, W. Liang, M. Hada, M. Ehara, K. Toyota, R. Fukuda, J. Hasegawa, M. Ishida, T. Nakajima, Y. Honda, O. Kitao, H. Nakai, T. Vreven, K. Throssell, J. A. Montgomery, Jr., J. E. Peralta, F. Ogliaro, M. Bearpark, J. J. Heyd, E. Brothers, K. N. Kudin, V. N. Staroverov, T. Keith, R. Kobayashi, J. Normand, K. Raghavachari, A. Rendell, J. C. Burant, S. S. Iyengar, J. Tomasi, M. Cossi, J. M. Millam, M. Klene, C. Adamo, R. Cammi, J. W. Ochterski, R. L. Martin, K. Morokuma, O. Farkas, J. B. Foresman, and D. J. Fox, Gaussian, Inc., Wallingford CT, 2016.

[14] S. J. Klippenstein, L. B. Harding, and B. Ruscic (2017). Ab initio Computations and Active Thermochemical Tables Hand in Hand: Heats of Formation of Core Combustion Species. *J. Phys. Chem. A.*, Vol. 121, pp. 6580–6602.

[15] E. Goos, A. Burcat, and B. Ruscic (2005). Extended Third Millennium Ideal Gas and Condensed Phase Thermochemical Database for Combustion with Updates from Active Thermochemical Tables, Update of Third Millennium Ideal Gas and Condensed Phase Thermochemical Database for Combustion with Updates from Active Thermochemical Tables.

[16] J.-E. Dubois, and H. Herzog (1972). Heats of formation of aliphatic ketones: Structure correlation based on environment treatment. *J. Chem. Soc. Chem. Commun.*, Vol. 0, pp. 932–933.

[17] P. Seller (1970). Enthalpies of formation of some aliphatic branched ketones. *J. Chem. Thermodyn.*, 1970, 2, 211–219.

[18] W. V. Steele, R. D. Chirico, S. E. Knipmeyer, A. Nguyen, and N. K. Smith (1996). Thermodynamic properties and ideal-gas enthalpies of formation for butyl vinyl ether, 1,2-dimethoxyethane, methyl glycolate, bicyclo[2.2.1]hept-2-ene, 5-vinylbicyclo[2.2.1]hept-2-ene, trans-azobenzene, butyl acrylate, di-tert-butyl ether, and hexane-1,6-diol. *J. Chem. Eng. Data*, Vol. 41, pp. 1285–1302.

[19] A.V. Blokhin, G. J. Kabo, A. A. Kozyro, L. S. Ivashkevich, A. P. Krasulin, V. V. Diky, and Y. V. Maksimuk (1997). Thermodynamic properties of 1-methylcyclopentanol and 1-chloro-l-methylcyclopentane in the ideal gas state. *Thermochim. Acta*, Vol. 292, pp. 19–29.

[20] B. Rajesh Kumar, S. Saravanan, R. Niranjan, Kumar, B. Nishanth, D. Rana, and A. Nagendran (2016). Effect of lignin-derived cyclohexanol on combustion, performance and emissions of a direct-injection agricultural diesel engine under naturally aspirated and exhaust gas recirculation (EGR) modes. *Fuel*, Vol. 181, pp. 630–642.

[21] United States Environmental Protection Agency Chemistry Dashboard: https://comptox.epa.gov/dashboard/dsstoxdb/results?search=DTXSID2021604 (accessed May 2, 2018.)

[22] https://www.sigmaaldrich.com (accessed May 2, 2018.)

[23] W. Leitner, J. Klankermayer, S. Pischinger, H. Pitsch, and K. Kohse-Höinghaus (2017). Advanced Biofuels and Beyond: Chemistry Solutions for Propulsion and Production. *Angew. Chem. Int. Ed.*, Vol. 56, pp. 5412–5452.

[24] D. A. Saldana, L. Starck, P. Mougin, B. Rousseau, and B. Creton (2013). Prediction of Flash Points for Fuel Mixtures Using Machine Learning and a Novel Equation. *Energy Fuels*, Vol. 27, pp. 3811–3820.

Secreteriat of the Vice-Rector for Research and International Relations,
University of Miskolc,
Responsible for the Publication: Prof. Dr. Tamás Kékesi
Published by the Miskolc University Press under leadership of Attila Szendi
Responsible for duplication: Works manager: Erzsébet Pásztor
Number of copies printed: 200
Put the Press in 2018
Number of permission: TNRT–2018–398–ME